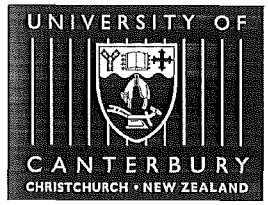

THE QUANTIFICATION OF AIRFLOWS GENERATED BY ROTATING ROLLERS IN WOOL CARDING MACHINES

by

Graeme Brendon Wood

UNIVERSITY OF CANTERBURY

Department of Mechanical Engineering

THE QUANTIFICATION OF AIRFLOWS GENERATED BY ROTATING ROLLERS IN WOOL CARDING MACHINES

A thesis submitted in fulfilment

of the requirements for the Degree

of

Master of Engineering

at

the University of Canterbury

by

Graeme Brendon Wood, B. Sc., B. E. (Hons)

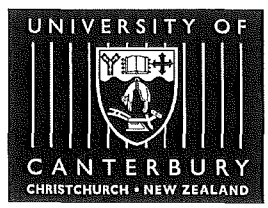

UNIVERSITY OF CANTERBURY

Department of Mechanical Engineering

Christchurch, New Zealand

March 2001

ABSTRACT

The properties of fibres make them easily manipulated by aerodynamic forces. The carding machine, used in cotton and wool processing, is an example of equipment that creates aerodynamic forces due to fast rotating cylinders with rough surfaces. These forces are generally seen as an undesirable side effect in fibre processing machinery, exacerbated with modern equipment using faster rotating components.

This work attempts to quantify these aerodynamic forces on carding machines used in the wool industry. A combination of boundary layer theory, experiments using hot wire anemometry and flow visualisation, and Computational Fluid Dynamics (CFD) software (Fluent) was used to build up an understanding of aerodynamics in the example of wool carding machines. The theoretical and experimental work progressed along the following topics to determine each effect on carding machine aerodynamics: rough surfaces, centrifugal forces, three-dimensional edge effects, and interactions between rotating cylinders. Examples from each section were modelled using CFD, which was found to accurately simulate theoretical and experimental results in most cases. It could also accurately predict the complex two-dimensional airflow patterns occurring in carding machines. The CFD simulations underestimated the degree of turbulence generated by interactions between rotating cylinders. Three-dimensional effects were overestimated, due in part to attempting to apply the results of an oversimplified model to a full-scale carding machine.

In undertaking this work, it was found the universal velocity distribution equations describing flow over flat plates (for both smooth and rough surfaces) could also be used for flow induced by rotating cylinders by compensating for curvature effects.

ACKNOWLEDGEMENTS

I would like to personally thank:

- Tony Bowen, who supervised this project and provided guidance on fluid mechanics issues.
- Ian Huntsman, whose knowledge of and guidance on CFD modelling was invaluable.
- Graeme Harris, who provided technical support and encouragement throughout this work. Special mention is made of the restrained demeanour he showed each of the innumerable times I presented him bust probes to fix.

Thanks are also due to the following organisations:

- The Foundation of Science, Research and Technology who funded this work via a PGSF grant to the Wool Research Organisation of New Zealand (WRONZ).
- WRONZ, for providing equipment and allowing me to take paid study leave in the earlier stages of my work.
- ADM Group Ltd, for allowing me to take paid study leave in the latter stages of my work.
- The various departments within Mechanical Engineering including workshop, computing and audio-visual for their contributions towards this work.

TABLE OF CONTENTS

1 INTRODUCTION

1.1 Aerodynamics and fibre processing

Aerodynamics plays an important role in fibre processing. Fibres have low mass, high surface area to volume ratio and high length to diameter ratio. Thus air streams can easily move individual fibres and masses of fibres. Intense air streams can move fibres attached to surfaces if the frictional forces binding them to the surface can be overcome by aerodynamic forces.

There are two aspects of aerodynamics in fibre processing, as a side effect or as an integral part of the fibre processing operation. The air currents generated by the rotating rough surfaces on the carding machine are not an integral part of the carding operation. However these currents have the potential to alter the desired fibre movement through the carding machine and cause quality problems not only with fibre migration across the roller, but also fibre removal from the carding machine. Modern carding machines tend to have higher roller surface speeds to increase production, but undesirable aerodynamic effects are exacerbated with higher roller speeds, and highly turbulent air currents may ultimately limit what speeds rollers can operate at.

Aerodynamics can also be used integrally in a fibre processing operation. Examples include pneumatic conveying of fibres and contaminant removal. Contaminants associated with fibres are often heavier than fibres and have much lower surface to volume ratios. Thus the contaminants have more inertia and are less sensitive to air currents than fibres. These differing properties have been utilised to enhance the separation of fibres from contaminants on cotton carding machines.

Although aerodynamics has many uses in the textile industry, its role in fibre processing is poorly understood. This is partly due to practical applications in fibre processing equipment being too complex to apply aerodynamic theories in the past. This has in turn stymied the invention of new processes utilising aerodynamics.

1.2 Brief introduction to wool carding process

The carding process involves the use of rotating cylinders covered with spikes to manipulate fibres. All wool and cotton is put through this carding process. In the case of wool, the wool is first washed and dried to remove as much contaminants (such as woolgrease and dirt) as possible. The wool fibres are then carded before either:

- being straightened (gilling) and combed to remove short fibres, then spun into yarn for apparel (fine wools)
- being directly spun into yarn for carpets (coarse wools)

Carding machines serve several functions. By passing fibres between the moving surfaces of the carding machine the fibres are disentangled, partially aligned, mixed and cleaned of contaminants.

Figure 1.1 illustrates a simplified carding machine. In the carding process, the wool is fed to the lickerin roller which grabs parts of tufts and transfers them via a transfer roller onto the main roller (swift roller). Once on the swift, the tufts are further separated by the worker rollers, which each collect typically 50% of all fibres passing underneath them. They then return the fibres to the swift via the stripper rollers. There are up to four pairs of worker and stripper rollers around the swift roller. The doffer roller collects a fraction of fibres moving along with the swift, and these fibres are removed from the doffer by an oscillating comb in the form of a web of partially aligned fibres. The remaining fraction of fibres not collected by the doffer will stay on the swift until collected by another worker roller, and so on.

The fancy roller moves faster than the swift and has long pins. It helps to flick out the fibres from between the teeth of the swift so the fibre can easily be gripped by the doffer.

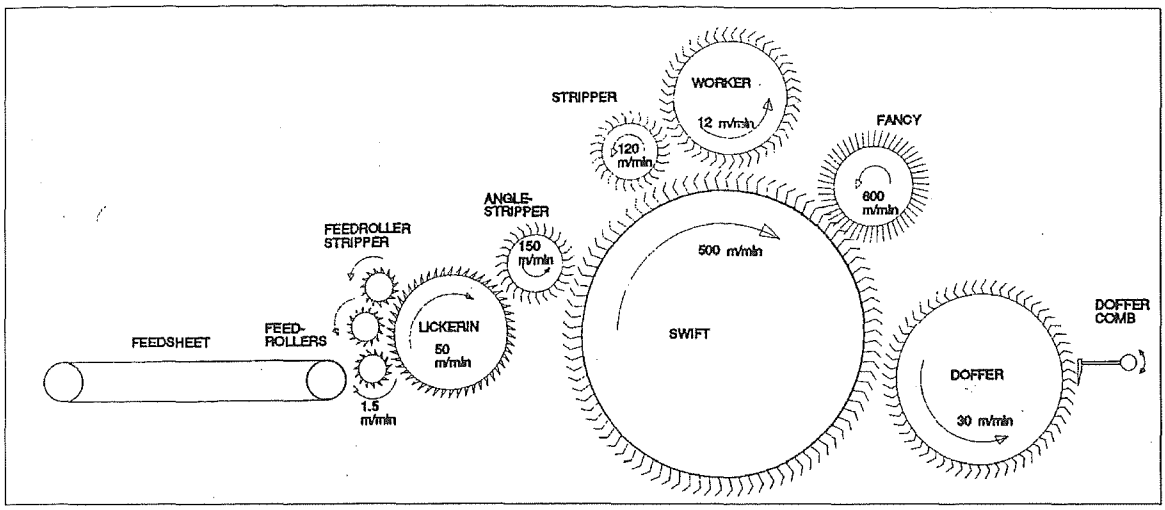

Figure 1.1. Simplified wool carding machine (WRONZ, 1994).

The carding actions falls into three categories:

- Point to point, a fraction of fibres being retained by both surfaces (worker/swift, doffer/swift)
- Point to back, all fibres removed from one surface to another (worker/stripper, stripper/swift)
- Back to back, fibres raised from one surface by another (fancy/swift)

These actions are illustrated in Figure 1.2.

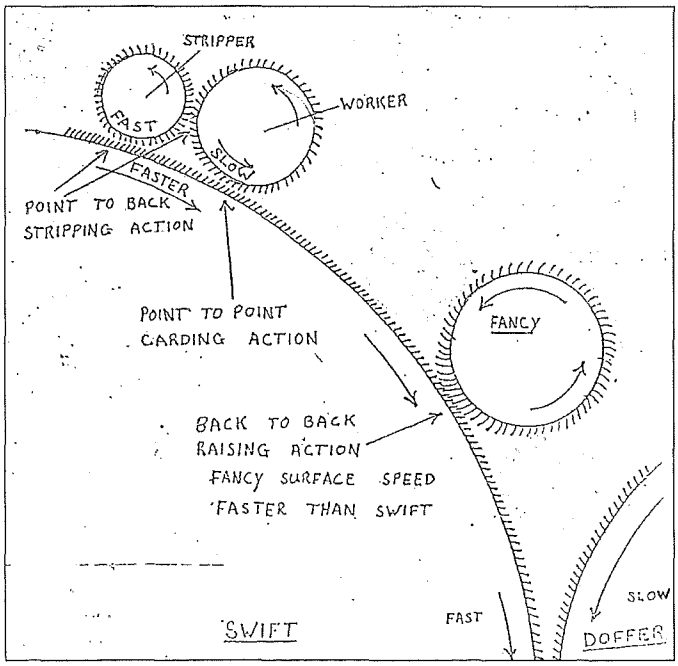

Figure 1.2. Various carding actions (WRONZ, 1997).

The clothing on card rollers falls into two categories, metallic (sawtooth) wire and fillet wire. Metallic wire resembles a fine saw blade, while fillet wire consists of staples inserted into a flexible foundation (Figure 1.3). Metallic wires are more commonly found in the feed end of the card (feed rollers, lickerin roller), while the fillet wire is used in the swift section of the carding machine.

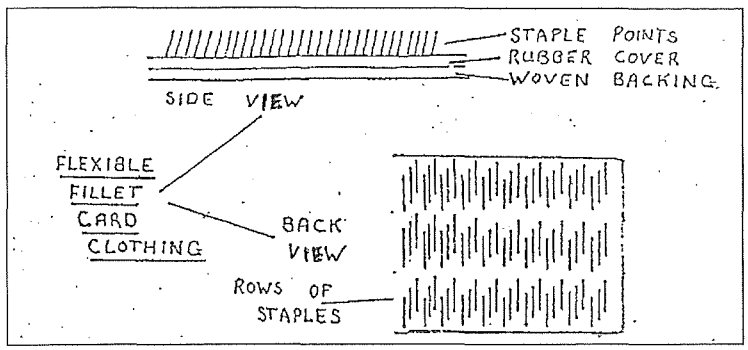

Figure 1.3. Fillet wire (WRONZ, 1997).

1.3 Project objective and schedule

The overall project objective was to quantify airflow characteristics generated within wool carding machines, using the underlying theory on how fluid flow is induced by the wire-clad rotating rollers. This objective was divided into sub-objectives that defined the project schedule.

1. Literature review

Review the literature, including theoretical, experimental and modelling/CFD work, on the following topics:

- Any previous work investigating the generation of aerodynamics on carding machines
- The effect of aerodynamics on fibre processing, including using aerodynamics to improve aspects of fibre processing
- The effect of 'rough' surfaces and individual roughness element geometries on fluid flow
- Fluid flow generated by rotating cylinders, including concentric rotating cylinders

2. Airflow behaviour over rough flat carding surfaces

Determine Fluent's approximation of flow over a rough flat surface. Conduct experiments in a wind tunnel on flat plates of fillet carding wire, using hot wire anemometry. Compare results to Fluent's predictions and open literature.

3. Airflow behaviour around a single rotating cylinder

Expand Fluent's predictions to airflow over a rotating cylinder of varying surface roughness and speed. Conduct experiments on a specially designed test rig to determine airflows around rotating cylinders clad with carding wires. Compare results to Fluent's predictions. Include 3D CFD simulation and flow visualisation.

4. Airflow behaviour around a pair of rotating cylinders

Conduct CFD, flow visualisation and hot wire anemometry tests on the airflow generated by a pair of rollers of varying roughness and speeds. Compare the results of each method and with potential flow theory.

5. Airflow behaviour around 2D carding machine components

Using the data gained from earlier work, further expand Fluent's approximation of airflow to various carding machine components. Compare with literature, observations of airflow around carding machines and trends noticed from individual rollers and roller pairs.

2 LITERATURE REVIEW

2.1 Introduction

As mentioned in the primary objective, this work is to quantify airflow characteristics generated within wool carding machines. The theory behind how the aerodynamics have been generated must be researched thoroughly in the open literature. The rotating roller (or cylinder) is what is generating the flow, but the airflow it generates is in turn affected by the roughness of its surface and the interaction of it with other rollers and stationary surfaces. As such, the literature review was split into two broad areas of interest, the generation and use of aerodynamics in fibre processing machinery and the underlying theory behind it. Then underlying theory was further divided into separate sections as outlined in Section 1.3.

2.2 Fibre processing operations involving aerodynamics

2.2.1 Carding processes and simulations

It has been known since at least 1881 (Bramwell) that high cylinder speeds (the fancy roller) can cause undesirable air currents that remove fibres from the carding machine and cause high fibre losses. The action of the fancy, which has a faster surface speed than the swift, is to manipulate the fibre web so it sits as far raised from the carding wire as possible and is more easily picked up by the doffer. This reduction of the fibre-wire binding force, combined with the high surface speeds means an increased likelihood of fibre losses. Shields, covers and baffle rollers have since been used to minimise the influence of the fancy and the swift rollers in generating air currents. However these devices did not completely remove the influence of air currents on fibre web quality. In assessing the variability of slubbings from across the card, WIRA (1948) stated that the 'light side threads' problem takes precedence over all other aspects of slubbing variation, and deduced that air currents were to blame.

The work by WIRA (1948) was the first attempt to quantify airflow profiles around a carding machine. It investigated air currents around the fancy roller region since the greatest air movement around a carding machine occured in this area. The direction of air currents in this area was determined using a smoke generator, while a vane anemometer was used to

gauge the magnitude of the currents. WIRA mentioned that obtaining information on speeds in this area was difficult due to the turbulent nature of the currents and eddies.

The general direction of air currents are shown in Figure 2.1. One side of the carding machine was fitted with a side shield on the belt drive side to minimise the influence of the fast moving belts. Outward currents are shown by dots and inward currents by circles. The general air movement was towards the fancy roller and over the worker roller. However there was a strong current out from the carding machine where an air dam is formed between the swift and doffer. Other comments were that there was a distinct tendency for material to be thrown out above the fancy near the ends of the last worker, and that any fly falling between the doffer and swift rollers tended to move towards the centre of the carding machine.

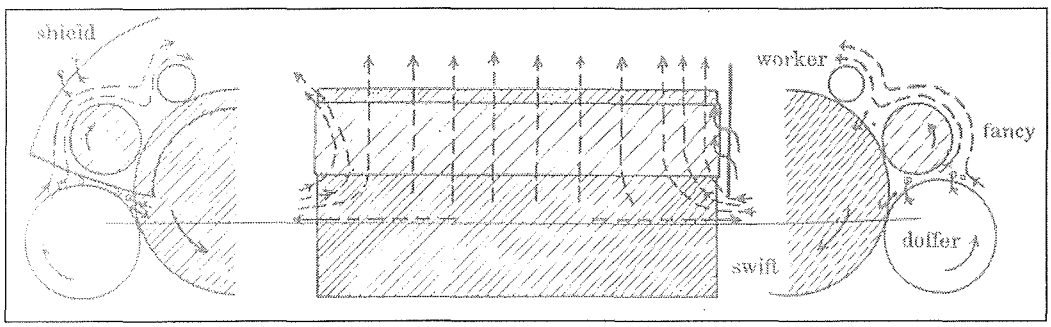

Figure 2.1. Air currents round the doffer, fancy and swift (WIRA, 1948).

Various experiments were conducted by WIRA (1948) on the effects of various parameters on the 'light sides'. The influence of moving belts had a significant effect in moving fibres from the sides of the carding machine. Installing side shields reduced, but did not eliminate fibre migration. Increased feed rate caused greatly enhanced fibre migration towards the centre of the rollers. This indicated that the carding wire was less able to grip all the fibres and the top layers were more susceptible to migration. Baffle rollers around the fancy did not significantly affect fibre migration.

The later version of the WIRA carding book (1969) contradicted its own earlier research on air currents in carding machines and considered it an insignificant problem after installing all the appropriate covers. It also comments on the role of fancys in blowing fibres away from the carding machine which, like Hewitt (1971) commented on the role of covers to minimise waste, as well as recommending top and bottom fly stripper rollers which are

positioned in the gaps between the fancy and swift. The position of the rollers seems to have a significant impact on reducing air currents because WIRA (1948) found baffle rollers mounted by the fancy but not by the swift of little use in minimising air currents.

Perhaps the most startling comment by WIRA (1969) on the influence of airflow (or lack of it) was that air currents played no significant part in fibre transfer. This statement was based on the results of high speed ciné photography which suggested that the air around the swift is relatively undisturbed to within less than a millimetre of the swift surface. No mention of whether fibre was present was given, nor were there photos, parameters or references given to support the comment. Another comment was that from the experience of designers of high production cotton carding machines, airflow only has a significant role in the carding action at surface speeds in excess of about 15 m/s, about twice that of a typical swift on a woollen card.

The work of Martindale (1945) was one of the first thorough investigations on the behaviour of wool on a card. It included what changes in speeds of the rollers relative to each other has on the carding effect. It was one of the first papers to rigorously define the role of workers in the carding process, and not only defines its role as an opener, but a mixer as well. It defines a worker 'collecting power', the fraction of wool transferred to the worker from the swift. It was stated qualitatively that an increase in the collecting power improves the carding process, and that it could be increased by increasing the worker speeds or narrowing the setting between the swift and the worker. Improved mixing can be achieved by running the workers at slightly different speeds to improve mixing. Many papers on carding give this paper as a reference.

Elliott (1986) predicted changes in efficiency due to process changes such as production rate and roller speeds on a model of the woollen carding process. The carding power is used to determine the degree of fibre mixing on the card. Increases in carding power were found to improve vegetable matter (VM) removal while lowering the incidence of neps (small masses of highly entangled fibres). Carding power could be increased by increasing the doffer-swift speed ratio, increasing the distance of the doffer from the swift, or altering the doffer and swift wire teeth angles. However the production rate (kg/h/mm card width) had a greater effect on VM removal and nep production than the carding power (although carding power is implicitly a function of production rate), with a denser mat increasing the number

of neps formed and VM present per unit weight of carded wool. The reduction in VM removal is likely to be the filtering effect of the denser web preventing contaminants to be removed from the wool.

As previously mentioned, changing aerodynamic responses in the carding process not only affects the evenness of the fibre web (WIRA, 1948, 1969), but also fibre losses (Bramwell, 1881). Elliott (1986) found that card losses increased as a function of swift speed, with higher airflows tending to throw unbound fibres further from the roller and increasing their likelihood of not being re-entrained with the fibre web. There was an optimum production rate and swift loading that minimised fibre losses. It is envisaged that at low loads, the only significant binding force that kept fibres on the card surface was fibre-wire binding forces, since low loading meant low fibre-fibre interaction. This was less sufficient to stop fibres being flung into the air stream and being blown away from the mat. Conversely, a high load prevents some fibres on the top layer of the web to adhere to the carding wire, therefore the only binding force for these fibres is the inter-fibre type, increasing the chance of fibre losses. Not surprisingly, the presence of covers was to significantly reduce card waste, due to re-entrainment of removed fibres back onto the web.

Elliott (1986) stated that from simulated carding tests, swift loading on an industrial carding machine was generally too low and that carding performance could be improved by lowering the doffer speed, without increasing production rate or swift speed. This improved carding power, therefore lowering nep count and improving VM removal, while lowering fibre losses due to the higher swift loading.

Ghosh (1968) looked into the effect of carding parameters on cotton fibre hook formation in the carding operation. The doffer and swift speeds were found to have an effect; increasing their speeds with constant production rate decreased the rate of hook formation and 'yarn imperfections', defined using the Uster Imperfection Tester which counts thin and thick places as well as neps. This is in contrast to carding machines for wool where increasing the swift/doffer ratio generally improves yarn production (Elliott, 1986; Martindale, 1945) and reduces nep content by increasing the carding power. No mention was given to carding waste, a problem with high swift speeds.

More recently, flow visualisation experiments have been conducted to closely investigate the trajectories of fibres caught in the induced draught from rotating cylinders. Most of the carding simulation and flow visualisation papers have been conducted on cotton carding machines, but the aerodynamic principles are similar for carding wool. Lauber (1995) published work describing fibre flow on cards. The non-contact flow visualisation technique of Laser-Doppler-Anemometry was used to track individual cotton fibres on a card. It mentions the qualitative effects of aerodynamics on fibre parallelism and that its effects are greatest underneath the fibre-transfer point between the swift and the doffer rollers. Air tended to be 'sucked up' towards the nip. This would have the consequence of fibres tending to move with the airflow while heavier material such as dirt would fall out of the air stream.

2.2.2 Aerodynamics and vegetable matter removal

Whereas air currents are generally seen as a nuisance in woollen cards, it has been implicit in more beneficial effects for cotton carding. Cotton carding machines differ in design to woollen cards in that they need to remove a greater amount of particulate material. Thus their taker-in zone (feed end) is more complex than for a woollen card. Klein (1986) discusses the use of mote knives that tend to scrape particulates from the fibre. The mote knife diverts the air currents away from the taker-in roller. Any particulate matter which is not bound to the fibres tend to be scraped or flung off by the mote knife with the air stream, while the fibres pass between the mote knife and attached to the roller.

The cotton blowroom also employs devices using aerodynamics to clean fibres (Klein, 1986). Aerodynamic forces are implicitly involved in the cleaning of fibres in rotating openers. Grids, in the form of triangular section bars, can be adjusted to allow varying amounts of waste between them. However since modern cotton processing operations produce a lot of dust which is carried along with the fibres, the waste collecting chamber has no influence on the operation, air recirculation from the chamber is minimal and fibre loss is increased. Previously the air currents that passed through the grid were used to good effect. The air, along with fibres would be actively recycled back through the grid, while heavier particles would fall out of the air stream.

The only device primarily using aerodynamics as a cleaning operation is the Platt Saco Lowell Air Stream Cleaner (Figure 2.2) (Klein, 1985). The opened fibre is blown along by an air stream into a rapidly converging duct before undergoing a sharp diversion (E). Fibres follow the air stream's change of direction but heavier particulates fly through a slot into a waste collection chamber (C). Like the older style openers, this cleaner does not work well on dust and fine particulates.

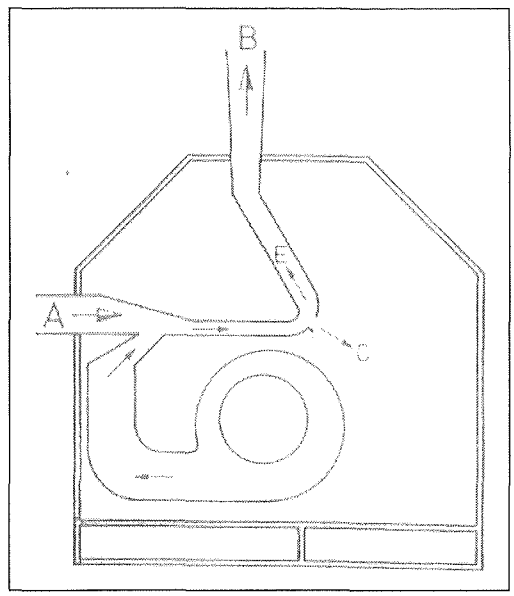

Figure 2.2. Air Stream Cleaner.

Klein (1985) details dust removal operations which involves either blowing or sucking the fibre to release the dust. Suction of dust requires use of a fibre retaining device such as a perforated plate. The Rieter dust extractor (Figure 2.3) (Klein, 1985) forms part of a pneumatic conveying system. A fan draws air from the conveying duct using a perforated converging pipe inside the duct. The converging duct imparts force on the fibres, while the fibres are 'washed' using the extra suction provided by the fan.

Dust can also be blown from the fibres. The carding process tends to generate air currents that move away from the rollers, carrying fly and dust with them. Although such means of dust removal from the fibres can be exploited, it is not generally used nowadays since maintaining a dust-free environment is considered much more important. Any dust that is blown off the fibres would then have to be removed by suction somewhere else in the process.

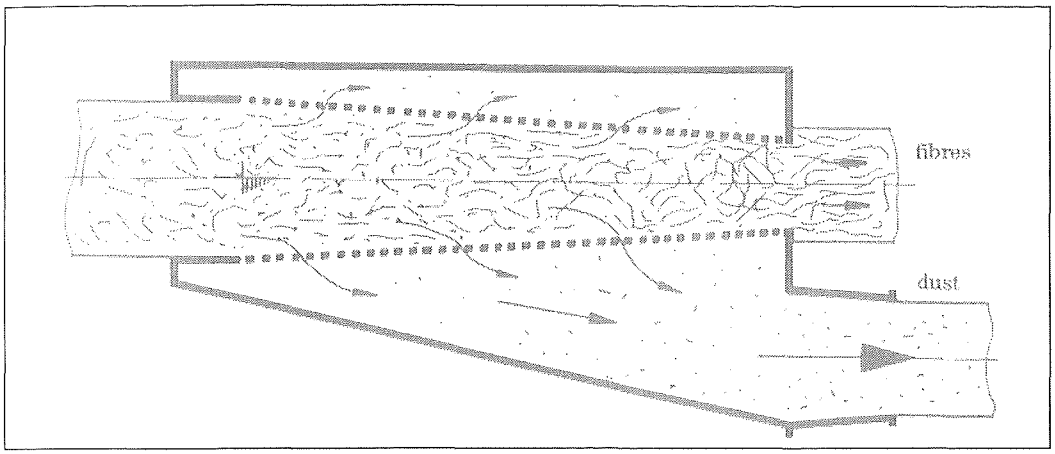

Figure 2.3. Rieter dust extractor.

2.2.3 CFD in fibre processing machinery

Open literature on this subject is very limited. Fluid flows in some finishing equipment have been investigated, but nothing specifically related to carding machines. Kong (1996) used CFD to predict airflow through a fibre transfer duct of a rotor spinning machine. The paper commented that the consequences of fluid recirculation in the duct was the increased likelihood of fibre buckling leading to deteriorated yarn quality and that future design of ducts should minimise recirculation. The work reinforces the work of Lawrence (1986) in recommending transfer ducts with a lower cross-sectional area. However, several simplifying assumptions were made including that the roller surface was smooth, no heat was transferred from the roller into the air stream, and the presence of fibres was not modelled. Farber (1996) comments on some areas in the textile finishing machinery area where CFD has been used such as an open-width washer. The paper concluded that CFD will be suitable to evaluate finishing machinery, but currently cannot be routinely used.

2.3 Fluid flow over flat rough surfaces

2.3.1 Boundary layer theory

Many papers and textbooks in fluid mechanics present the velocity profile near a wall converted to a 'dimensionless' form. For laminar flow near a wall, the shear stress can be expressed as:

$$\tau = \mu \frac{du}{dz} \tag{2.1}$$

where τ = shear stress, N/m^2

μ = molecular viscosity, Ns/m^2

u = velocity, m/s

z = distance from surface, m

Defining a 'friction' velocity which is a measure of the intensity of turbulent eddying:

$$u_* = \sqrt{\frac{\tau}{\rho}} = \sqrt{\overline{u'v'}} \tag{2.2}$$

where u', v' = instantaneous velocities - time-averaged velocities in the x and y directions respectively, m/s

Integrating Equation 2.1 yields the relationship

$$\frac{u}{u_*} = \frac{zu_*\rho}{\mu} \text{ or } u^+ = z^+ \tag{2.3a, b}$$

and noting that the shear stress is constant in the laminar region right to the wall,

$$\tau = \tau_w \tag{2.4}$$

Equation 2.3a is valid within the laminar sublayer, i.e. a dimensionless velocity (u^+) is expressed as a function of 'dimensionless' distance (z^+) away from the wall.

Prandtl (in Schlichting, 1979) describes a turbulent 'universal velocity' profile based on a mixing length theory. The mixing length (l) is assumed to be proportional to the distance away from the wall, i.e. $l = \kappa z$. With the turbulent shear stress (τ_t) being described in similar form to the laminar shear stress,

$$\tau_t = \varepsilon \frac{du}{dz} \tag{2.5}$$

where ε = eddy viscosity = $\rho l^2 \frac{du}{dz}$ (2.6)

It follows that

$$\tau_t = \kappa^2 z^2 \left(\frac{du}{dz}\right)^2 \tag{2.7}$$

Prandtl than made the assumption that the turbulent shear stress remains constant from the wall to well into the turbulent boundary layer, i.e.

$$\frac{du}{dz} = \frac{u_*}{\kappa z} \tag{2.8}$$

With the constant of integration corresponding to the condition that $u = 0$ at a certain distance z_0 away from the wall, and using a dimensional argument that z_0 is proportional to the ratio ν/u_*, one obtains

$$u^+ = \frac{1}{\kappa} \ln z^+ + A, \tag{2.9}$$

where κ = Von Karman's constant, approximately 0.4.

$A \approx 5.0 - 5.5$

There was good agreement to experimental data for values of $z^+ \geq 70$. Note that the velocity distribution in both the laminar and turbulent boundary layer can be described in terms of dimensionless velocity and length.

These same results can be obtained by using a more general method based on dimensional analysis first presented by Millikin (1939). This method relies on fewer assumptions and is not based on a mixing length theory.

2.3.2 Concepts of 'sand' and 'aerodynamic' roughness heights

The universal velocity profile can also be used to describe flow over rough surfaces. There is a shift in u^+ to compensate for the decreased velocity close to a rough surface, i.e.

$$u^+ + \left(\frac{1}{\kappa} \ln z_0^+ + B \right) = \frac{1}{\kappa} \ln z^+ + A \tag{2.10}$$

where B = constant

The roughness term can be determined either by using a 'sand roughness' height (k_s) or an aerodynamic roughness height (z_0), i.e.

$$z_0{}^+ = \frac{k_s u_* \rho}{\mu} \quad \text{or} \quad z_0{}^+ = \frac{z_0 u_* \rho}{\mu} \tag{2.11a,b}$$

The sand roughness height was originally used by Nikuradse (in Schlichting, 1979) and its use has since become commonplace. Nikuradse found three regimes of roughness, hydraulically smooth, transition, and completely rough. The laminar sub-layer depth was also given as approximately $u_*\rho/\mu$. So the three roughness regimes could be defined as the extent the roughness elements protruded out of the laminar sub-layer. For example, if the roughness elements are extremely small or if the flow is purely laminar ($z_0{}^+ < 5$), the elements are wholly contained in the laminar sub-layer and resistance is solely due to this layer. In the case of turbulent flow or large roughness elements ($z_0{}^+ > 70$), all protrusions

extend outside the laminar sub-layer and resistance is mainly due to the drag caused by them. Surfaces with sufficiently large roughness elements ($z_0^+ > 70$) have been termed 'fully rough'. For fully rough surfaces. Nikuradse found that B = -3.0, and Equation 2.10 reduces to

$$u^+ = \frac{1}{\kappa} \ln \frac{z}{k_s} + 8.5 \qquad (2.12)$$

The aerodynamic roughness height (z_0) is commonly used in wind engineering textbooks. It is easier to derive from experimental results since it can be obtained directly from a plot of u vs. ln z over any surface by extrapolating the line to ln z = 0. If it is used in place of the sand roughness height, A=B by definition and Equation 2.10 reduces to its more common form

$$u^+ = \frac{1}{\kappa} \ln \frac{z}{z_0} \qquad (2.13)$$

The aerodynamic roughness height is related to the physical roughness height using Equation 2.14:

$$z_0 = ke^{\kappa(B-5.5)} \qquad (2.14)$$

where k = height of roughness element, m

Using a value of 0.40 for the von Karman constant, and a 'sand roughness' surface, where $k = k_s$, and B = -3.0, then $k_s \approx 30\ z_0$ if the element density is not dense enough to cause the airflow to skim over the elements. The aerodynamic roughness height approach has been used in the experimental work and converted to a sand roughness height when appropriate.

2.3.3 Influence of roughness element geometry on fluid flow

2.3.3.1 Expansions of Equations 2.12 and 2.13

The problem with Nikuradse's approach is that it assumes all rough surfaces encountered can be expressed as a simple function of k_s. In reality, many rough surfaces cannot be expressed trivially as a function of k_s, and are a function of parameters such as element sparseness (λ) and shape. This element sparseness factor was defined as the ratio of the specific floor surface per roughness element to roughness element frontal surface area. Anomalies were found when trying to scale up Nikuradse's 'sand roughness' concept to flow over non-spherical roughness elements, for low roughness element density, or over terrein. Paeshke (in Schlichting, 1979) determined that for wind movements over vegetation,

$$k_s = 4k \qquad (2.15)$$

Lettau (1969) found that the aerodynamic roughness height (z_0) related not only to element height, but also to element sparseness. Nikuradse's roughness height was replaced with the term

$$z_0 = 0.5\, k\lambda \tag{2.16}$$

which agreed normally within the ±25% range but was found to be inaccurate at low λ (<10) since skimming over the roughness elements was found to occur.

O'Laughlin (1969) investigated turbulent flow through an array of obstacles as well as over it and found that the log-law term was only able to describe flow to within a height of two roughness elements from the ground. Below this 'wake layer', the velocity profile was flatter than the log-law prediction. This could be interpreted as the start of the transition to the laminar sub-layer approaching the tops of the roughness elements.

Mulhearn (1977) also used the log-law equation to describe flow over a rough surface, but included a 'skimming' displacement term (d) to be subtracted from z and found better agreement to experimental data, i.e.

$$u^+ = \frac{1}{\kappa} \ln \frac{z-d}{z_0} \tag{2.17}$$

Mulhearn kept Von Karman's term κ constant at 0.41 and varied d to get the best fit. In reality both, z_0 and d can 'displace' the roughness boundary layer. Different researchers have investigated varying κ and z_0 while omitting d, while others kept κ constant and varied z_0 and d to get the best fit. A recent publication, Dyrbye (1997) also uses d, which seems to be of more practical use over forest canopies where the whole profile is displaced from the ground to the tree tops. Jackson (1977) gives a good treatise in the virtues of varying either κ and z_0 or z_0 and d. The paper states that many authors assume that d=0 since varying all three variables does not give accuracy, especially for d, although making d=0 increases the scatter for z_0.

2.3.3.2 Expansion of *B* in Equation 2.10.

Several researchers expanded the term B in Equation 2.10 to account for roughness geometries. Dvorak (1969) expanded the law of the wall and calculated B as a function of element sparseness.

$$u^+ = \frac{1}{\kappa} \ln \frac{z}{k_s} + 5.5 - B\,, \tag{2.18}$$

where $B = 17.35(1.625 \log \lambda_d - 1), \quad 1 \le \lambda_d \le 4.68$ (2.19)

$B = -5.95(1.103 \log \lambda_d - 1), \quad \lambda_d > 4.68$ (2.20)

$\lambda_d = s/t,$

s = spacing between elements parallel to flow, m

t = horizontal length of roughness element parallel to flow, m

There exists a discontinuity for B at $\lambda_d = 4.68$, and values lower than this induce less drag. This is because of the skimming effect that occurs with increasing element density. Simpson (1973) was able to apply these equations to a more generalised term for element sparseness. With shape factors similar to that for sand, B was calculated to be close to –3.0, and Equation 2.18 became identical to the standard law of the wall equation for rough surfaces. For values of B other than –3.0, the sand roughness height is related to the projected height using Equation 2.21,

$$k_s = ke^{\kappa(3.0+B)} \tag{2.21}$$

For experimental work, it is best to modify Dvorak's equation to incorporate z_0, which is a function of k and B. Substituting Equation 2.14 into Equation 2.13,

$$u^+ = \frac{1}{\kappa} \ln \frac{e^{\kappa(5.5-B)} z}{k} \tag{2.22}$$

The formulae from other researchers can all be converted into this form. The only variable term is B, which in turn is a function of the 'element sparseness', the definition of which varies amongst the researchers.

Wooding (1972) gave a comprehensive review of work done to date on determining flow and drag generated by roughness elements, including extensive work by Marshall (1971) on flow over cylinders. The paper took previous data and fitted them to the log-law equation, but took into account the effects of λ as well as a shape factor (height/thickness). So Wooding took into account the fact that although k and λ have an effect on the flow profile, an increasing horizontal element would have a calming effect on eddy formation. For example, a flat square plate projected upwards would have a greater drag than a cube, although they would have the same height and area ratio.

The equations used in Wooding's work were converted to a function of B:

$$B = \log \frac{3.7}{\lambda \psi_1^{0.4}}, \qquad \lambda \leq 0.1 \qquad (2.23)$$

where ψ_1 = streamwise aspect ratio = (k/t)

Dirling (in Grabow, 1975) expanded the roughness density concept for non-uniform surfaces and introduced a 'bluntness parameter' (β) into the element sparseness term:

$$B = 13.28(1.639 \log \Lambda_d - 1), \qquad \Lambda_d \leq 4.93 \qquad (2.24)$$

$$B = -9.34(1.171 \log \Lambda_d - 1), \qquad \Lambda_d > 4.93 \qquad (2.25)$$

where $\Lambda_d = \frac{\sqrt{A_f}}{k} \beta^{\frac{4}{3}}$, (2.26)

β = bluntness parameter ($=A_s/A_p$)

A_s = windward surface area of roughness, m^2

A_p = projected area of roughness in flow direction, m^2

Sigal (1990) combines data from Schlichting, Dvorak and other researchers to yield the best fit equations for B:

$$B = 17.35(1.634 \log \Lambda_d - 1), \qquad \Lambda_s \leq 4.89 \qquad (2.27)$$

$$B = 2.2, \qquad 4.89 < \Lambda_s < 13.25 \qquad (2.28)$$

$$B = -9.55(0.686 \log \Lambda_d - 1), \qquad 13.25 \leq \Lambda_s \leq 100 \qquad (2.29)$$

where $\Lambda_s = \lambda \beta^{1.6}$ (2.30)

Waigh (1998) relates k_s to B using the following equation:

$$k_s = k e^{\kappa(4.0+B)} \qquad (2.31)$$

i.e. for 'sand roughness' surfaces, B = -4.0 and correlates data to best fit lines using shape and bluntness factors:

$$\frac{U}{u*} = \frac{1}{\kappa} \ln \frac{e^{\kappa(5.0-B)} z}{k}, \qquad (2.32)$$

$$B = 10.56 \log (\lambda \psi_2^{0.87} \beta^{0.44}) - 7.59, \qquad \Lambda_w < 6 \qquad (2.33)$$

$$B = -5.75 \log (\lambda \psi_2^{0.55} \beta^{1.38}) + 5.78, \qquad \Lambda_w > 6 \qquad (2.34)$$

where $\Lambda_w = \lambda \psi_1 = \frac{np}{st}$ (2.35)

ψ_2 = spanwise aspect ratio (= k/p)

p = horizontal length of roughness elements normal to flow, m

n = spacing between elements normal to flow, m

It was noted by Waigh that parameters such as cell aspect ratio (ratio of distance between elements parallel and perpendicular to flow) was not seen to significantly alter velocity profiles.

2.4 Flow induced by rotating cylinders

2.4.1 Analytical solution

Taylor (1923) was one of the first researchers to look at velocity profiles between concentric rotating cylinders. Taylor observed that at Reynolds numbers below a certain value, the velocity profile between the cylinders could be evaluated analytically using the Navier-Stokes equation describing angular momentum in polar co-ordinates. The relationship takes the form

$$u = Ar + \frac{B}{r},\ A = \omega_i \frac{\left(1 - \frac{\omega_o r_o^2}{\omega_i r_i^2}\right)}{\left(1 - \frac{r_o^2}{r_i^2}\right)},\ B = r_i^2 \omega_i \frac{\left(1 - \frac{\omega_o}{\omega_i}\right)}{\left(1 - \frac{r_o^2}{r_i^2}\right)} \qquad (2.36\text{ a, b, c})$$

where A, B = constants

r = distance from origin, m

ω = angular velocity, rad/s

i.e. the sum of solid body rotation and a 'potential' vortex. For very small clearances between the inner and outer cylinders, where curvature effects are negligible, the profile could be approximated as being linear, and is analogous to Couette flow between flat plates. For very large clearances, i.e. the outer cylinder radius approaches infinity, the flow becomes that of a potential vortex, where the angular momentum is constant at any distance away from the cylinder (Ur = constant). This solution can also be derived from potential flow theory. Milne-Thomson (1968) gives the solution for non-slip flow induced by a rotating cylinder as

$$u = \frac{a}{r} U_w \qquad (2.37)$$

where a = radius of cylinder, m

Taylor noticed that as the speed of the inner cylinder was increased above a critical Reynolds number of around 120, here defined as:

$$\mathrm{Re} = (r_o - r_i)\frac{u\rho}{\mu} \qquad (2.38)$$

the flow not only became turbulent, but was unstable to axisymmetric differences and leads to the development of toroidal eddies encircling the inner cylinder. The tangential velocity profile became S-shaped, and was dependent on Reynolds number.

Schlichting (1979) describes flow induced by a rotating disc, which can also be thought of as an infinitely thin cylinder. The layer near the rotating disc is carried by it through friction and thrown outwards due to centrifugal forces. This loss of fluid is replenished by fluid which flows in an axial direction towards the disc (the axes of the cylinder) (Figure 2.4).

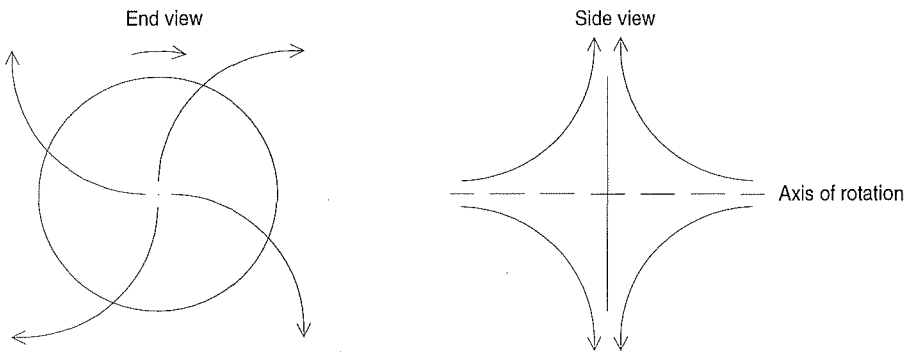

Figure 2.4. Induced flow past a rotating disc.

Kirchoff (1985) describes the fluid flow patterns generated around two rotating vortices of equal magnitude using potential flow theory. Potential flow theory states that there is conservation of mass and momentum in fluid flow. Assumptions made include that the fluid has zero viscosity, thus neglecting near-wall viscous effects. The difference between flows around cylinders and vortices is that vortex flow is around a point of origin and can deform around that point. Figures 2.5 to 2.8 show the general patterns for velocity contours and stream functions around co-rotating and counter-rotating vortices of equal magnitude. The stream function (ψ) lines represent the direction of fluid flow around the vortices. They were calculated from the following equations:

Co-rotating: $$\psi = \frac{1}{2}\log r_1 r_2 \qquad (2.39)$$

Counter-rotating: $$\psi = \frac{1}{2}\log \frac{r_1}{r_2} \qquad (2.40)$$

where $r_1 = x^2 + (y - a)^2$

$r_2 = x^2 + (y + a)^2$

$2a$ = distance between vortices, m

The velocity contour (isotach) equations given in Kirchoff involve complex numbers. However, the velocity components can be calculated from the partial derivatives of the stream function, i.e.

$$u = -\frac{\partial \psi}{\partial y}, \qquad v = \frac{\partial \psi}{\partial x} \tag{2.41a,b}$$

where u = velocity component in x-direction, m/s

v = velocity component in y-direction, m/s

q = velocity magnitude = $\sqrt{u^2 + v^2}$, m/s

Using Equations 2.41a and b, the velocity contours were solved numerically using a spreadsheet, with the graphical output shown on Figures 2.5 to 2.8.

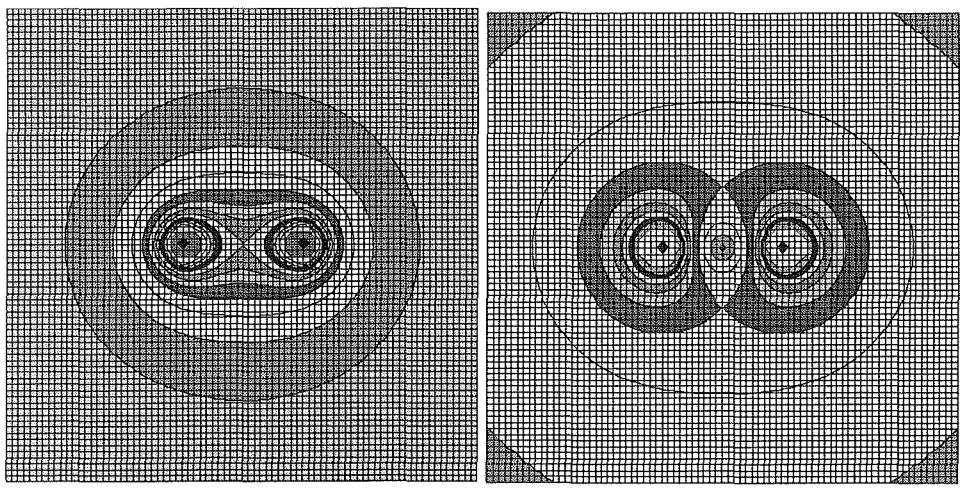

Figures 2.5 and 2.6. Velocity contours for counter-rotating and co-rotating vortices respectively.

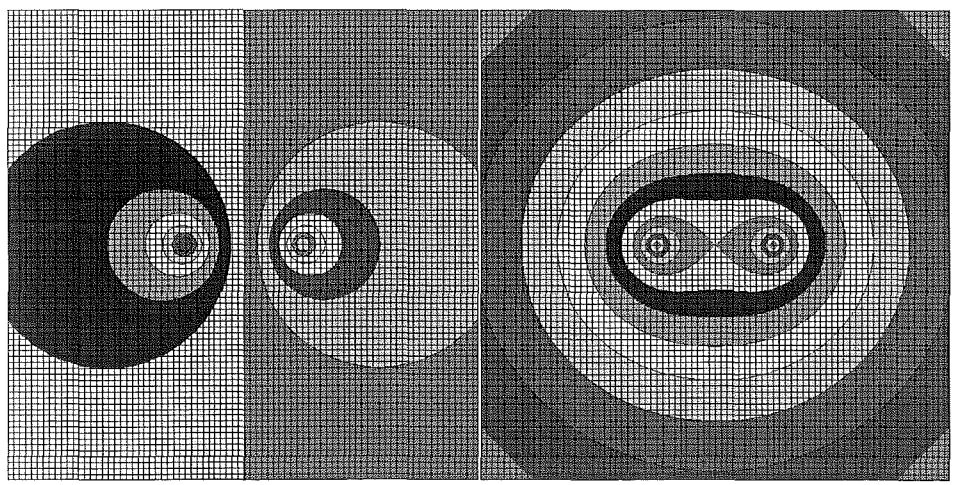

Figures 2.7 and 2.8. Stream function contours for counter-rotating and co-rotating vortices respectively.

Note that the stream function pattern for the co-rotating vortices is the same as the velocity contour pattern for the counter-rotating vortices.

2.4.2 Semi-empirical methods

The work by Theodorsen and Regier (1945) was the one of the first to investigate the fluid dynamic processes for a rotating cylinder in isolation, measuring torque and deriving an iterative equation to calculate friction coefficients:

$$\sqrt{\frac{2}{C_f}} = \frac{1}{\kappa}\ln\left(\mathrm{Re}\sqrt{\frac{C_f}{2}}\right) - 1.2\,,\ \mathrm{Re} = \frac{aU_w\rho}{\mu},\quad C_f = \frac{\tau_w}{\frac{1}{2}\rho U_w^2} \qquad (2.42a, b, c)$$

where C_f = friction coefficient, dimensionless

Dorfmann (1963) was one of the first researchers to derive velocity profiles for turbulent flow between concentric rotating cylinders. One underlying assumption were that the turbulent shear stress was related to a turbulent or 'eddy' viscosity (ε). The other was to consider the shear stresses acting on each cylinder. If the moments of the forces of action and reaction are equal, the shear force moment is conserved between the cylinders, i.e.

$$\frac{d}{dr}\left(r^2\tau\right) = 0\,,\ r^2\tau = a^2\tau_w \qquad (2.43a, b)$$

Equation 2.43b was also assumed to be applicable for a cylinder rotating in infinite space. The final assumption was that the mixing length was still proportionally related to the distance from the wall.

The assumptions were accurate very close to the inner rotating cylinder. However curvature effects on the streamline flow were not taken into account, i.e. the mixing length was not linearly related to the distance from the rotating surface away from the laminar sublayer. Bradshaw (1969) deduced that the effects of roller curvature on the apparent mixing length are appreciable when the shear layer thickness is greater than 1/300 of the radius of curvature.

Kasagi and Hirata (1975) looked specifically at experimental velocity profiles around rotating cylinders and were one of the first researchers to try and fit velocity profiles to the universal velocity form. Velocity profiles were similar to flat-plate theory close to the moving wall ($z^+ > 5$), where viscous effects dominate and curvature effects were negligible,

but deviated from flat-plate theory for turbulent flow. Kasagi used an algebraic eddy viscosity model to fit the experimental velocity profiles but it only fitted within the laminar region.

Smith and Townsend (1982) studied turbulent flow between concentric rotating cylinders (outer to inner radius ratio of 1.5) in more detail. Although much of their research was devoted to investigating the 3D flow profiles of turbulent Taylor vortices, their work on streamline velocity showed that, within the values of z^+ investigated (< 60), the approximation of flat-plate theory for rotating flows was adequate.

2.4.3 Inclusion of curvature effects

Furuya et al (1978) was one of the first researchers make an attempt to compensate for cylinder curvature effects. Combining the laminar and turbulent shear stress components in cylindrical coordinates, and assuming constant shear force moment away from the wall, one obtains:

$$\tau = \mu r \frac{\partial \omega}{\partial r} - \rho \overline{u'w'} = \frac{a^2}{r^2} \rho u_*^2 \tag{2.44}$$

Using the following terms:

$$\frac{\partial r}{\partial z^+} = \frac{\nu r^3}{u_* a^3}, \quad \omega_* = \frac{u_*}{a}, \omega^+ = \frac{\omega}{\omega_*} \tag{2.45a, b, c}$$

$$z^+ = \frac{a u_* \rho}{\mu} \frac{\left(r^2 - a^2\right)}{2r^2} \text{ (integrating Equation 2.45a)} \tag{2.46}$$

One obtains

$$\frac{\partial \omega^+}{\partial z^+} - \frac{r^2 \overline{u'w'}}{a^2 u_*^2} = 1 \tag{2.47}$$

Noting that Reynolds stresses disappear approaching the wall ($w' \rightarrow 0$), we have the simple term

$$\frac{\partial \omega^+}{\partial z^+} = 1 \tag{2.48}$$

Integrating, $\omega^+ = z^+ + C$ (2.49)

Satisfying the boundary conditions ($\omega = \omega_0$ at $z^+ = 0$), and converting into terms of u, the final solution reads:

$$\frac{U_w - \frac{a}{r}u}{u_*} = \frac{au_*\rho}{\mu}\frac{\left(r^2 - a^2\right)}{2r^2} \tag{2.50}$$

where $U_w - \frac{a}{r}u$ = angular velocity defect, m/s

Note that Equation 2.50 is only valid for laminar flow due to the absence of the turbulent Reynolds stresses. The terms r-a (= z), and a/r are very small and the equation can be approximated to laminar flow over a flat plate. Also note the use of an angular velocity defect to compensate for rotational effects. The velocity term for rotating cylinders has usually been defined as a straight velocity defect (U_w - u).

Furuya (1978) then uses a dimensional analysis technique first presented by Millikin (1939) to show that the z^+ term obtained for the laminar regime is also valid for turbulent regime, i.e.

$$\frac{U - \frac{a}{r}u}{u_*} = \frac{1}{\kappa}\ln\left(\frac{au_*\rho}{\mu}\frac{\left(r^2 - a^2\right)}{2r^2}\right) + A \tag{2.51}$$

The same conclusion could be reached using the same assumptions in Prandtl's mixing length theory (Equations 2.8, 2.9).

Nakamura et al (1983) was able to fit the log-law in the turbulent region with experimental data, but found that the constant terms (κ; A) needed different values to best fit the data (0.55, 9.8), with κ being obtained from a thin cylinder rotating in an axial uniform stream (Furuya, 1978). Nakamura's paper was one of the first to review the friction coefficient (C_f) data available in literature and found some wide discrepancies. One reason was whether the data was obtained from a rotating cylinder in an infinite fluid or from between concentric cylinders; the inner wall shear stress becomes larger with a decreasing gap between the cylinders. The distance between the cylinder and a physical boundary (other than an outer cylinder) such as a wall or a floor could also be a contributing factor. Since boundary layers are reported by Williamson (1987) to be very large, up to 30 times the cylinder radius, such boundaries could have an effect.

Nakamura was able to compare the two experimental methods available to obtain u_*. The conventional method is obtaining Reynolds stresses $\overline{u'w'}$ (=τ/ρ) with an X-wire hotwire

anemometer, using Equation 2.2 and assuming that $r^2\tau = const = a^2\tau_w$. Nakamura also obtained u_* from plotting the velocity defect vs. distance from the wall in the laminar regime using Equations 2.2 and 2.3. Nakamura obtained close comparison between both methods. Nakamura also tested the validity of the constant shear force moment assumption and found good agreement, although at distances of z more than $0.6a$ away from the wall, $r^2\tau/a^2\tau_w$ fell below unity. One reason for this could be due to the absence of the outer cylinder required to make Equation 2.43b valid at any distance from the rotating inner cylinder.

Another possible reason for differences is the roughness characteristics of the cylinder material. Nakamura used cylinders made of aluminium alloy and claimed they were smooth. Other papers failed to even mention the cylinder material. It is known that most surfaces, although they may appear smooth, exhibit roughness characteristics, as apparent on a Moody diagram. Refer to Massey (1989) for an example.

The most recent paper found on rotating cylinders in a quiescent fluid was that by Dierich et al (1998), who uses an analytical eddy viscosity model to model the velocity profile. The resulting equation is complicated and only applicable to $z/a = 0.5$. Although the experimental data was comprehensive, there was no mention made about the cylinder material, and the friction coefficients are generally higher than that of Nakamura. However the velocity data as plotted in the universal law form did show the characteristic dependence on Reynolds number, and the shear force moment was relatively constant up to $z/a = 0.5$.

2.4.4 Numerical methods

Numerical methods have been used in the past few years to fit experimental velocity profiles. Williamson (1987) used numerical methods based on mixing length to obtain friction coefficients and velocity profiles and obtained a good fit to Theodorsen's friction coefficients, but the predicted velocity profile was less accurate outside of the laminar sublayer. Andersson (1992) used a low Reynolds number second moment transport model to predict velocity profiles but found deviations, suspected to be due to an overpredicted turbulent shear stress. Andersson also compared the different methods to obtain friction velocity (namely, from friction coefficient, Reynolds stresses, and from velocity gradient) and found large discrepancies, particularly between the experimentally obtained Reynolds

stresses and velocity gradients. The Reynolds stress method was probably more accurate, particularly since all the measurements were made close to the wall ($z > 0.1a$) and $r^2\tau$ was reasonably constant. Also, the velocity data as plotted by Andersson did not fall neatly on a straight line.

Wild (1996) looked at previous work on fluid flow induced by rotating cylinders. The review concentrated on flow patterns emerging when one cylinder rotated concentrically inside another stationary cylinder. Applications of this system include heat transfer between the rotor and stator in motors, and flow patterns between the rotor and wall in centrifuges. Within the laminar regime, the flow pattern changes from Couette flow to Taylor vortex flow beyond a critical Reynolds number. The flow is characterised by the formation of an array of toroidal vortices, the characteristics of which depend on geometric and fluid properties, as well as start-up acceleration. The vortex structure remains as the flow becomes fully turbulent.

Wild used CFD (Fluent) to determine streamline patterns for the turbulent flow between a rotating cylinder and a fixed enclosure as applied to a centrifugal desalinator. The results showed that the log-law profile could adequately predict the velocity data for an infinitely long cylinder. However the log-law profile slightly underestimated the velocity changes very close to the rotor and enclosure. This discrepancy is in line with the inaccuracy of the log-law term very close to a surface. The maximum radial velocities occurring as a result of the Taylor vortices were about one seventh that of the average tangential velocity in the annulus.

2.5 Conclusions

2.5.1 Fibre processing operations involving aerodynamics

On carding machines, fast moving cylinders are known to cause high air currents and undesirable side effects, including fibre migration and losses. This is particularly true for the fancy roller, which not only rotates faster than any other roller, but also has the roughest surface. Covers, shields and similar devices are now used in an attempt to minimise air currents but with varying success. The cotton industry uses air currents generated by moving surfaces for more beneficial effects. Some vegetable matter removal processes in use aerodynamics implicitly in cotton carding machines or explicitly in some cleaning

equipment. Although fibre processing operations have been modelled, the use of CFD has been very limited, the main applications being modelling air movements in cotton rotor spinning machines.

2.5.2 Fluid flow over flat rough surfaces

The Influence of roughened surfaces on fluid flow can be approximated by modifying the universal velocity law for smooth surfaces with a roughness term, based on an equivalent roughness height. Both sand roughness height (k_s) and aerodynamic roughness height (z_0) are commonly used and are directly related to each other ($k_s \approx 30z_0$). However the roughness heights themselves are a function of roughness element geometries. There are many correlations that exist but their validity and accuracy vary widely. A general trend between the correlations is that two formulae are required since there exists a certain element density parameter value that induces the maximum drag on fluid flow. As the elements are spaced more sparsely, the drag reduces. The same is true if the density is increased over this value since a skimming effect occurs and the drag correspondingly reduces.

The aerodynamic roughness height concept is derived from the ease of finding its value by plotting a simple semi-log plot of fluid velocity as a function of distance from the surface.

2.5.3 Flow induced by rotating cylinders

There have been attempts to determine velocity profiles around rotating cylinders by several researchers. In laminar flow, an analytical solution has been found, but there were only semi-empirical or numerical solutions if the flow becomes turbulent, the bases of which have often found to have been flawed.

There is no known work in the public domain on quantifying velocity profiles around systems of rotating cylinders. The closest approximation for two rotating cylinders was a pair of potential flow vortices in co-rotating and counter-rotating motion. Of the semi-empirical approaches, work that modified the universal velocity profile for curvature effects found the most favour, and the equation used by Furuya can be easily used in experimental work.

3 AIRFLOW BEHAVIOUR OVER FLAT ROUGH SURFACES

3.1 Introduction

The work done in this section has been done for several reasons, although it may not be of direct relevance to work on rotating surfaces. The simplicity of the velocity profiles generated along the fixed rough surface will allow accurate comparisons between experimental results, formulae obtained from literature and Fluent's computational estimates. There has been much work done in this area, whereas no rigorous research has been published on rotating cylinders with rough surfaces. Any problems in input/output errors in Fluent can be more easily picked up at an early stage without the complications of a moving surface. Finally, the hot wire anemometers used to measure air speed can be positioned closer to the tips of the carding wire 'teeth' on a fixed surface than a fast rotating surface. This would enable more accurate velocity profiles to be obtained very close to the wire tips.

3.2 Experimental method

3.2.1 Equipment

This work was conducted in the atmospheric boundary layer wind tunnel situated in the Industrial Aerodynamics Laboratory of the University of Canterbury Mechanical Engineering Department (Figure 3.1). The height and width of the tunnel in the testing zone was 1.22 metres square, and the length of the working section was 10 metres. The carding wire strips (typically about 40 mm wide) were cut and laid flat over a section of particle board measuring 2.44 x 1.22 m and glued into place, then reinforced by either nails or staples at the edges, being careful not to damage the wires. As much hand-tension was put on the wires as possible to minimise the bowing of the wire strips along the centre. The position of the board was close to the honeycomb immediately downwind of the air filter to minimise wind tunnel turbulence intensity effects. The wind tunnel turbulence intensity was about 0.4%.

Figure 3.1. Boundary layer wind tunnel.

Air velocity measurements were taken with a Thermo Systems Inc. (TSI) linearised anemometer using DISA 55P14 hot wire probes. Velocities were obtained from recorded voltages using a TSI calibrator which provided a uniform jet of air to the probe and induced a pressure drop measured by a Betz manometer in mm H_2O. The velocity was obtained from the pressure drop using the following correlation:

$$v = 7.5034\sqrt{\frac{H(273+T)}{1.0185P}} \tag{3.1}$$

where H = pressure drop, mm H_2O

P = air pressure, mbar

T = air temperature, °C

A calibration curve could then be generated from the velocity versus voltage data using a polynomial best-fit equation. This calibration was checked each day a set of runs was to be conducted.

The probe could be positioned to an accuracy of 0.1 mm using a computer controlled traverser that had full 3D movement in cartesian coordinates. The accuracy of the probe height from the tips of the wires could be verified throughout a run using a telescope mounted outside of the wind tunnel.

Once the probe was calibrated and its coordinates confirmed, the fans could be started. The fans are contra-rotating Woods 48 J 1/2 aerofoil S-type variable pitch axial flow fans each powered by 25 kW motors. The wind speed could be adjusted by varying the blade angle from a pneumatic controller, and measured from the manometer using Equation 3.1. The free stream velocity was set at about 12 m/s unless stated otherwise.

Instantaneous velocity readings from the hot wire probe were taken at 2.5×10^{-3} second intervals for five seconds, giving a total of 2 000 readings in each set.

The position of the probe would only change in vertical distance from the wires in a typical run. Some 15 – 18 sets of readings would be taken in a vertical traverse of the probe. The closest reading would be 1 – 2 mm from the tops of the wires and extend to beyond the boundary layer (300 mm). Most readings were taken within 60 mm of the wires.

3.2.2 Properties of carding wires

Important parameters from the carding wires wire used in experimental work are detailed in Tables 3.1a and 3.1b. The carding wires were provided by Wool Research Organisation of New Zealand (WRONZ) and are shown in Figure 3.2 to 3.4. Note that since fancy wires are only laid on carding machines to lie downwind, only downwind experiments were recorded for fancy wires. Experiments were done for swift wires facing in both directions. There was also a trial over a particle board surface to serve as a comparison against the carding wire surfaces. The particle board surface was absent for the swift wire boundary layer development experiments but was present for all other experiments.

Values of B using the various researchers equations were then calculated from these parameters (Table 3.2) and an estimate of z_0 produced (Table 3.3). These values would then be compared to experimental results to determine which equation is the most accurate.

Table 3.1a Carding wire properties.

Wire type	Alternative notation	Comments	Wire length (mm)	Projected wire height (mm)
Swift #1			3.5	3
Swift #2			3.8	3.3

Fancy #1	New, dense wire		20.5	18
Fancy #2	New, loose wire		20	17.5
Fancy #3	Old, dense wire	Some wires dirty	17.5	15.5
Fancy #4	Old, loose wire	Many wires bent	23.5	20.5

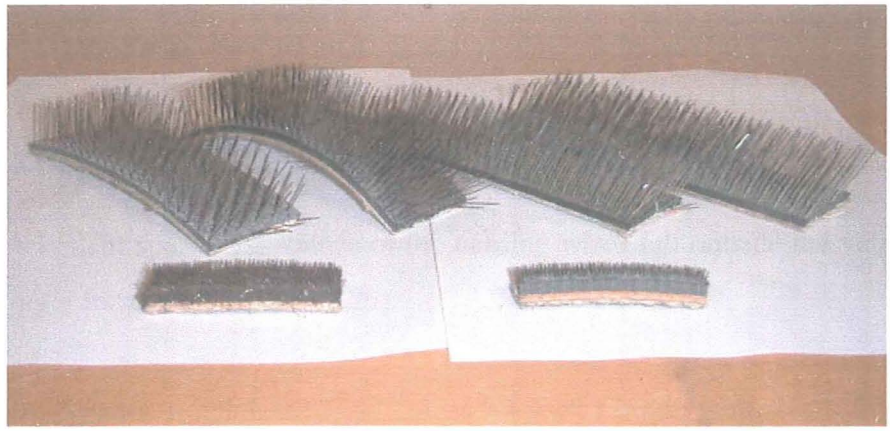

Figure 3.2. Carding wires used in flat surface experimental work. From left: fancy #1, swift #1, fancy #2, fancy #3, swift #2, fancy #4.

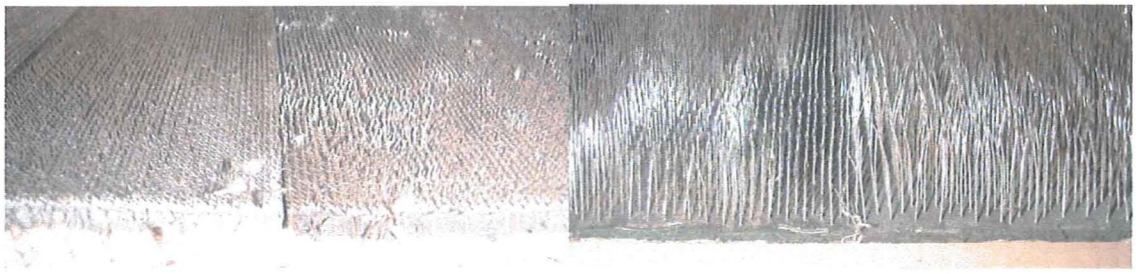

Figures 3.3 and 3.4. Example of working surface for swift and fancy wires respectively. Figure 3.3 shows swift #1 wire on the left, swift #2 wire on the right. Figure 3.4 shows fancy #3 wire on the left, fancy #4 wire on the right.

Table 3.1b.

Wire type	Thickness parallel to flow (mm)	Thickness normal to flow (mm)	Spacing parallel to flow (mm)	Spacing normal to flow (mm)
Swift #1	0.46	0.35	1.75	1.44
Swift #2	0.39	0.30	1.50	1.28
Fancy #1	0.58	0.38	4.90	2.17
Fancy #2	0.61	0.52	6.40	3.25
Fancy #3	0.51	0.31	5.20	2.38
Fancy #4	0.85	0.51	6.40	3.30

Table 3.2. B values for each carding wire.

Wire type	Wooding (λ)	Dvorak	Simpson	Dirling	Sigal	Waigh
Swift #1	2.4	-3.4	-6.6	-17.4	-3.5	0.1
Swift #2	1.9	-2.8	-9.2	-19.7	-6.4	0.3
Fancy #1	1.6	-1.2	-11.9	-27.8	-9.4	-1.1
Fancy #2	2.3	1.2	-7.2	-24.3	-4.5	-1.6
Fancy #3	2.6	1.5	-5.8	-25.8	-3.3	-2.4
Fancy #4	2.0	-0.7	-8.7	-25.7	-6.0	-1.5

Note that the element sparseness values of the carding wires fall outside the valid range for use in Wooding's formula (Equation 2.23).

Table 3.3. Aerodynamic roughness height values for each carding wire.

z_0 values (mm)						
Wire type	Wooding	Dvorak	Simpson	Dirling	Sigal	Waigh
Swift #1	5.4	0.09	0.023	3.2×10^{-4}	0.08	0.42
Swift #2	8.2	0.12	0.009	1.4×10^{-4}	0.03	0.51
Fancy #1	93.8	1.24	0.017	3.0×10^{-5}	0.05	1.59
Fancy #2	60.1	3.11	0.108	1.2×10^{-4}	0.32	1.26
Fancy #3	48.3	3.14	0.171	5.7×10^{-5}	0.46	0.81
Fancy #4	74.2	1.68	0.069	7.8×10^{-5}	0.21	1.51

3.2.3 Determination of velocity profiles and roughness parameters

The characteristic method to graph velocity profiles was to plot velocity on the x-axis and distance from the surface on the y-axis. Using this format, the usual form of the log-law equation (Equation 2.13) was transformed to

$$z = z_0 e^{\frac{\kappa}{u^*}U} \tag{3.2}$$

Rearranging,

$$\ln z = \ln z_0 + \frac{\kappa}{u^*}U \tag{3.3}$$

the y-intercept was $\ln z_0$ and the slope was κ/u^*. Thus the parameters of aerodynamic roughness height and friction velocity can be obtained from the plotted data.

Once friction velocities were obtained, the dimensionless velocities, u^+ (Equation 3.4a) and distances, z^+ (Equation 3.4b) could be calculated and plotted to yield a universal velocity plot for the carding wires.

$$u^+ = \frac{U}{u_*}, \qquad z^+ = \frac{z u_* \rho}{\mu} \tag{3.4 a,b}$$

As mentioned in Section 2.3.2 the sand roughness height, a required input into Fluent, is related to the aerodynamic roughness height, $k_s \approx 30.0\, z_0$.

3.2.4 Determination of boundary layer properties

A set of runs was conducted on the swift wires to determine the boundary layer development along the surface parallel to the airflow. The boundary layer development does not directly affect the effect of the roughness elements (and therefore the aerodynamic roughness height). However, there was only enough carding wire to clad a 2.44 m length of the tunnel and it was feared the boundary layer could be too small to obtain meaningful data in the log-law region.

Once it was determined the boundary layer was thick enough to obtain sufficient velocity measurements in the log-law region, all subsequent measurements were taken near the end of the carding wire surface (2.1 – 2.4 m along the surface).

Boundary layer parameters were derived from the graphs using a curve fitting program. Firstly, the distance from the wire surface (minus the displacement depth) was found where the velocity was 99% of the maximum velocity (u_{99}) ; this is usually defined as the extent of the boundary layer (Schlichting, 1979). The boundary layer thickness (defined as the distance by which the external field of flow is displaced outwards as a consequence of the decrease in velocity in the boundary layer, δ^*) was then calculated using the equation:

$$\delta^* = \int_{z=d}^{(z-d)_{u99}} \left(1 - \frac{U}{u_{\max}}\right) dx \tag{3.5}$$

The boundary layer thicknesses obtained along the flat surface multiplied by the area upon which it acts on yields the volumetric flow of air that the rough surface has dragged.

The momentum thickness (θ) is similar to the boundary layer thickness but quantifies the loss in momentum due to the boundary layer:

$$\theta = \int_{z=d}^{(z-d)_{99}} \frac{U}{u_{\max}}\left(1-\frac{U}{u_{\max}}\right)dx \qquad (3.6)$$

3.3 Features of CFD relevant to this work

Before detailing the method and results of using CFD to model airflows over flat rough surfaces, it is pertinent to mention in more detail some of the features of CFD that will be used repeatedly through out this work. The simulation work presented here used Fluent, a commercially available CFD software package. Fluent models fluid flows by solving the conservation equations for mass and momentum using a finite element difference method. The wide range of physical models and solver methodologies allows Fluent and its associated grid meshing software (Gambit) to accurately simulate many applications in fluid flow.

3.3.1 Approximation of rough surfaces

Fluent (Version 5) contains one model that accounts explicitly for wall roughness. It also includes a porous media model that implicitly accounts for roughness.

The explicit wall roughness model is based on Nikuradse's equation for equivalent sand roughness in pipes. The model uses the terms:

$$\phi = \frac{1}{\kappa}\ln(\varepsilon' z^+), \qquad \varepsilon' = \frac{9.8}{1+C_{\mathrm{Re}} z_0^+}, \qquad z_0^+ > 90 \qquad (3.7a, b)$$

Only C_{Re} and the sand roughness height (k_s) are input values. Note that the roughness constant term is not the standard notation found in the open literature. However if the default value for C_{Re} of 0.33 is used, and noting that for $z_0^+ > 90$,

$$1 + 0.33\, z_0^+ \approx 0.33\, z_0^+ \qquad (3.8)$$

then the equation can be converted to Equation 2.12.

Implicit roughness could be introduced using the porous media model. Porous media can be modelled using a variation of the Ergun equation (Ergun, 1952) which is composed of two

parts, a viscous term which dominates when the flow is laminar, and an inertial term which dominates when the flow is turbulent.

$$\frac{\Delta P}{L} = \frac{1}{\alpha}\mu v_i + C_2 \frac{1}{2}\rho |v_i| v_i \qquad (3.9)$$

where α = permeability, m^2

C_2 = inertial resistance factor ($\approx$ inverse permeability), 1/m

This momentum sink contributes to the pressure gradient in the porous cell, creating a pressure drop that is proportional to the fluid velocity (or velocity squared) in the cell.

Porous media are modelled as live cells and are set on the grid before calculations take place. Therefore another input is the amount of cells to be labelled as porous, which requires knowledge of the porous media height. This was initially set as the roughness element height.

Note that there are two unknowns, the permeability and the inertial resistance factor. If the flow regime is predominantly either laminar or turbulent, then one of the terms can be dropped.

3.3.2 Near-wall treatments

There are two classes of treatments for near-wall flow, the wall function approach and the two-layer zonal model. The wall function approach 'bridges' the solution variables at the near-wall cells and the corresponding quantities on the wall. The two-layer zonal model resolves the solution variables all the way down to the wall, attempting to resolve the viscosity-affected near-wall region all the way to the viscous sublayer. The whole domain is subdivided into a viscosity-affected region and the fully-turbulent region.

It was important that there were accurate predictions of velocity close to the surface, particularly for rotating surfaces where the sublayer may be fractions of a millimetre thick. Thus the near-wall grid was constructed to immerse at least one line of cells within the laminar sublayer. Therefore if the wall function treatments do not provide an accurate answer, the two-layer zonal model could be used. Each section describes which treatment was used.

Although the two-layer zonal model may be more accurate, it does not quantify wall roughness as an explicit value (in terms of sand roughness height) that can be used in Fluent. Roughness characteristics need to be evaluated from graphing the airflow profile (refer to Section 3.1.3 for details).

3.3.3 Turbulence models

Fluent incorporates the Reynolds stresses to mean flow qualities by three versions of turbulence models that are applicable to this work, the κ-ε model, the Renormalisation Group (RNG) κ-ε model, and the Reynolds Stress Model (RSM). More details are given in Chapter 19.3 of the Fluent 4 Users Guide (1996).

The κ-ε model is a semi-empirical model that uses the Boussinesq hypothesis that the Reynolds Stresses are proportional to the mean velocity gradients, the constant of proportionality being the turbulent viscosity μ_t. Despite the simplicity of the model, it has proven to be robust and most papers referring to the use of CFD to model processes used the κ-ε model.

The RNG κ-ε model is based on the κ-ε model but uses a theoretical rather than a semi-empirical basis and yields improved predictions of near-wall flows, separated flows and flows with high streamline curvature. However it contains no special treatment for rotating reference frames.

The assumption in the κ-ε models that μ_t is isotropic may not hold in highly swirling flows. The RSM calculates the individual Reynolds Stresses provides a better alternative, but comes at a cost of iterating speed.

All three models were used in this work to varying degrees of success. The CFD application sections detail what model was used and what happened.

3.4 Setting up the CFD model

The wind tunnel was modelled in Fluent as a two-dimensional surface with a uniform inlet velocity of 11.4 m/s. This inlet velocity was chosen since the boundary layer displacement effects pushed the free stream velocity to 12 m/s, the same as for the experimental work. As

for the experimental work, there was a 700 mm particle board surface positioned immediately downwind of the tunnel entrance, followed by the 2.4 m carding wire surface. The input value of the particle board sand roughness height was determined by experiment and assumed to be constant. Using the default value of C_{Re} from the Fluent equation, the input value of k_s in Fluent is the same as k_s from experimental data. The sand roughness height or porous height of the wire surface was a variable term.

The closest grid point was 1 mm away from the wire surface and the distance between each point was increased by a factor of about 3% moving away from the surface (Figure 3.5). This was done to increase the accuracy of the simulation within the boundary layer while minimising points within the bulk flow. The grid point profile was also expanded away from the tunnel inlet for similar reasons. The total grid comprised of 122 nodes along the tunnel by 152 nodes traversing the tunnel height, a total of approximately 18 000 internal nodes.

Underrelaxation factors were set at 0.5 for the velocity terms, 0.7 for pressure and 0.9 for the turbulence parameters. It was important to let the solution converge to a low normalised velocity residual (about 3×10^{-6} for each velocity term) otherwise significant errors in the boundary layer profile resulted. The solutions took between 500 – 1 000 iterations and lasted approximately 0.5 – 1 hour on a Pentium II 400 MHz computer, depending on what initial conditions were used.

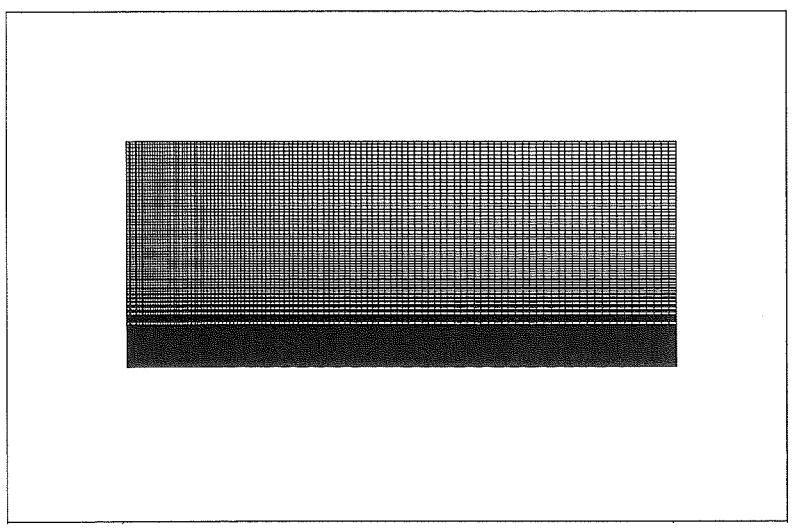

Figure 3.5. Typical grid structure for flat surface, flow from left to right.

3.5 Results and discussion

3.5.1 Swift wire experiments

3.5.1.1 Velocity profiles

Figures 3.6 and 3.7 show the velocity profile as a function of distance from the surface (direction normal to the airflow) and distance along the surface (direction parallel to airflow). The friction velocities generally decrease along the surface while the aerodynamic roughness height remains essentially constant.

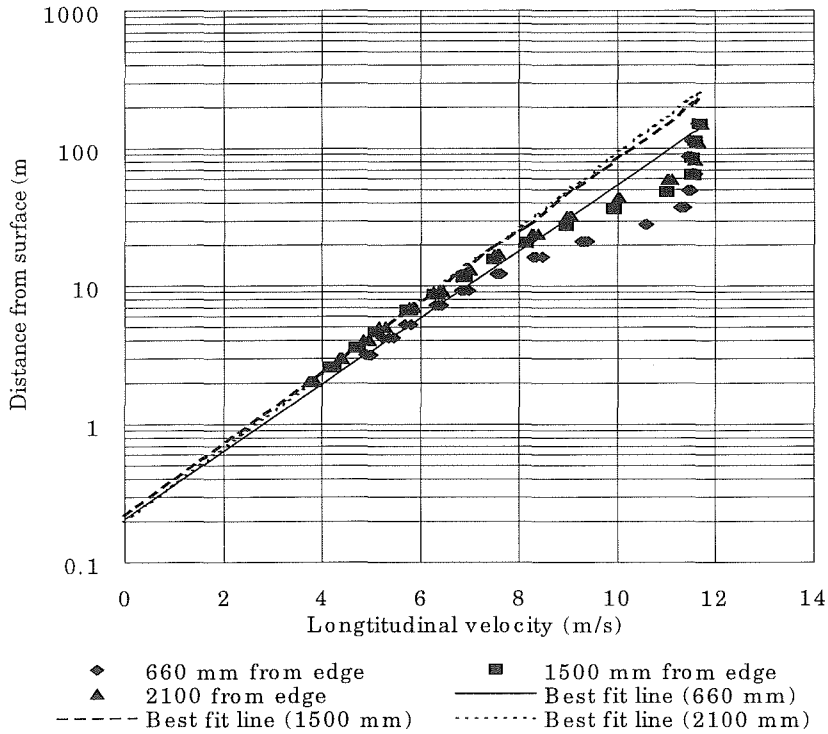

Figure 3.6. Velocity profiles over swift wire #1.

From reading the slope and intercept of the best fit lines and using Equation 3.3, aerodynamic parameters were derived for the carding wires and detailed in Tables 3.4 and 3.5.

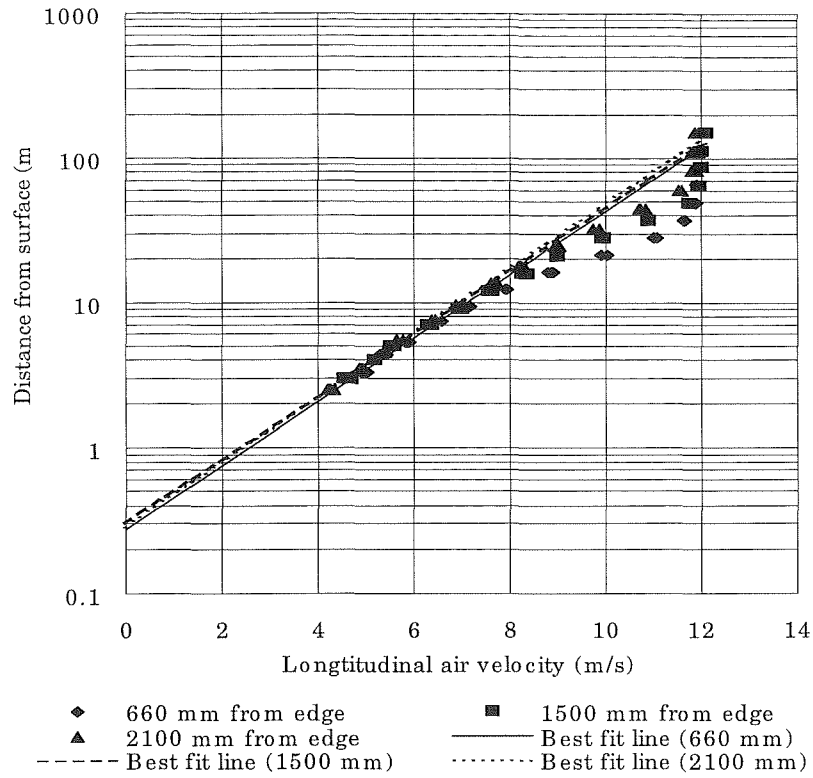

Figure 3.7. Velocity profiles over swift wire #2.

Table 3.4. Aerodynamic properties for swift wires.

Surface type.	Distance along surface (mm)	Direction of wires	z_0 (mm)	k_s (mm)	u^* (m/s)
Swift #1	660	upwind	0.21	6.3	0.72
Swift #1	1 500	upwind	0.21	6.3	0.67
Swift #1	2 100	upwind	0.20	6.0	0.65
Swift #1	2 400	upwind	0.22	6.6	0.74
Swift #1	2 400	downwind	0.22	6.6	0.77
Swift #2	660	upwind	0.27	8.1	0.79
Swift #2	1 500	upwind	0.30	9.0	0.80
Swift #2	2 100	upwind	0.28	8.4	0.78
Particle board	660	upwind	0.057	1.7	0.63

Table 3.5 gives averaged values of aerodynamic roughness height, B and sand roughness height for the swift wires. When compared to values derived from each of the log-law variations given in Section 2.3.3.2, Waigh's formulae give the closest fit. Furthermore, only

the aerodynamic roughness equations of Waigh and Dvorak come consistently to within an order of magnitude of the experimental results.

Table 3.5. Averaged roughness properties of swift wires.

	z_0 (mm)	k_s (mm)	B
Swift #1	0.21	6.3	-1.15
Swift #2	0.28	8.4	-0.67

Although Waigh's equations gave the best estimate, in all cases Λ was calculated to be over 6, therefore the equation describing flow in a sparsely spaced element region was used (Equation 2.34). This conflicts with the other methods that imply the carding wires are densely spaced.

With friction velocities evaluated, the data could be presented on a universal velocity plot. Figure 3.8 shows a comparison between swift wire #1 and the particle board surface.

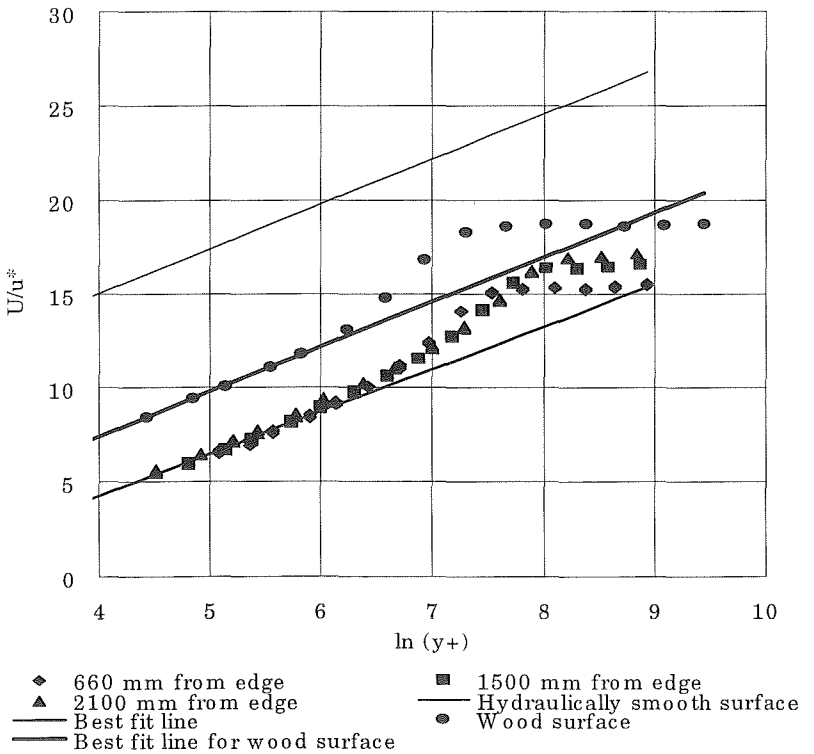

Figure 3.8. Universal velocity profile over swift wire #1 and particle board.

3.5.1.2 Boundary layer development

Table 3.6 shows the boundary layer properties for the swift wires in various positions along the surface and with the wires facing upwind/downwind. Since a displacement depth was not used for the swift wires, $d = 0$ in Equations 3.5 and 3.6 and a linear velocity profile was assumed between the position of velocity measurement closest to the surface and the surface itself (where $U = 0$). As expected, the boundary layer developed over the wires along the surface, but changed little after about 2 metres length along the tunnel. The boundary layer may have become fully developed at this stage.

The trend of decreasing friction velocity for increasing boundary layer depth held true for swift wire #1, but was less noticeable for swift wire #2.

Table 3.6. Boundary layer data for various surfaces.

Wire type	Distance along surface (mm)	Direction of wires	δ (mm)	δ^* (mm)	θ (mm)	δ/δ^*	δ/θ
Swift #1	660	Upwind	48.2	10.4	5.71	4.63	8.44
Swift #1	1 500	Upwind	61.2	14.7	8.57	4.16	7.14
Swift #1	2 100	Upwind	77.8	17.0	10.4	4.58	7.48
Swift #1	2 400	Upwind	79.2	15.9	9.96	4.98	7.95
Swift #1	2 400	Downwind	69.7	14.7	9.27	4.74	7.52
Swift #2	660	Upwind	43.9	10.3	5.43	4.26	8.08
Swift #2	1 500	Upwind	56.5	12.8	7.30	4.41	7.73
Swift #2	2 100	Upwind	72.9	15.0	8.95	4.86	8.14
P. Board	660	Upwind	43.6	8.74	5.21	4.99	8.37

3.5.1.3 Effect of wire inclination

There was a slightly enhanced skimming effect due to the angle of element inclination downwind rather than upwind, resulting in a lower boundary layer thickness and a lower amount of air being dragged. This could be due to the elements pushing air upwards causing a higher displacement depth and slightly reducing the form drag caused by the individual element. An analogous effect can be seen as wind crosses a wheat field; the form drag is reduced when the wheat stalks orientate themselves downwind. Conversely, elements

pointing upwind could cause air to be pulled lower through the elements, lowering the skimming effect and therefore the displacement depth, causing a greater form drag.

Regardless of the effect on friction velocity and boundary layer depth, the element inclination seemed to have no significant effect on the aerodynamic roughness height. For both experiments, z_0 was estimated to be 0.22 mm (Table 3.4).

3.5.1.4 CFD comparisons

When the average k_s values for swift wire #1 (6.3 mm) and swift wire #2 (8.5 mm) were used in Fluent, the calculated velocity profile was in good agreement with experimental data (Figure 3.9).

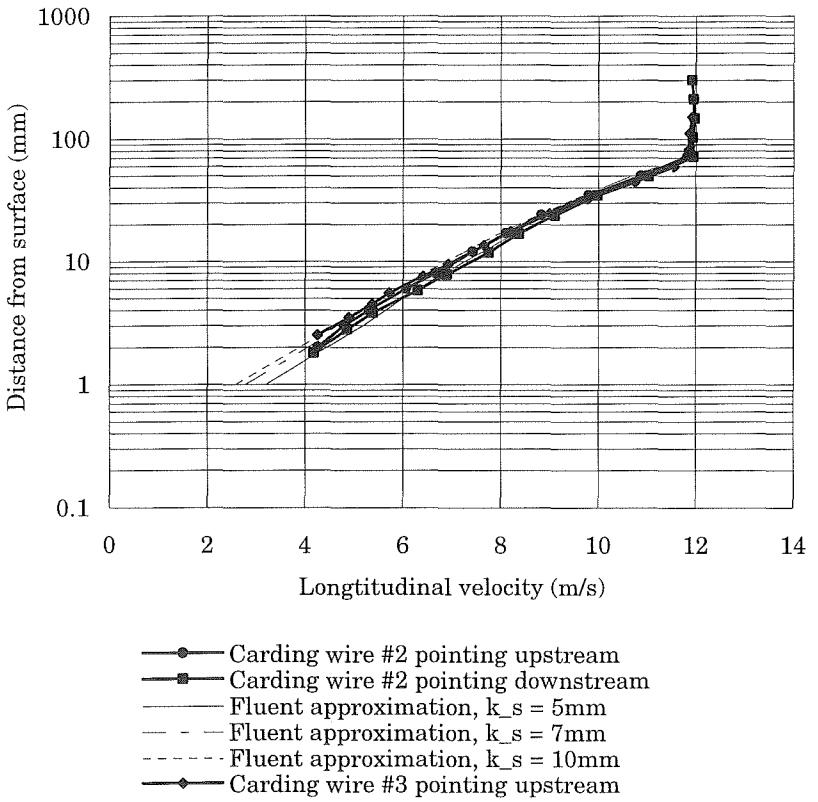

Figure 3.9. CFD comparison with experimental results for velocity profiles over swift wires.

3.5.2 Fancy wire experiments

3.5.2.1 Velocity profiles

Figure 3.10 shows the velocity profiles of the different fancy wires as a function of distance away from the surface. The log-law region of the boundary layer was readily apparent, although it did not possess the characteristic wake (the deviation from the log law close to the outer boundary layer). Despite the differences in characteristics between the fancy wires, the airflow profiles over them were remarkably similar. Table 3.7 details aerodynamic parameters using Equation 3.3 and the raw velocity information illustrated in Figure 3.10.

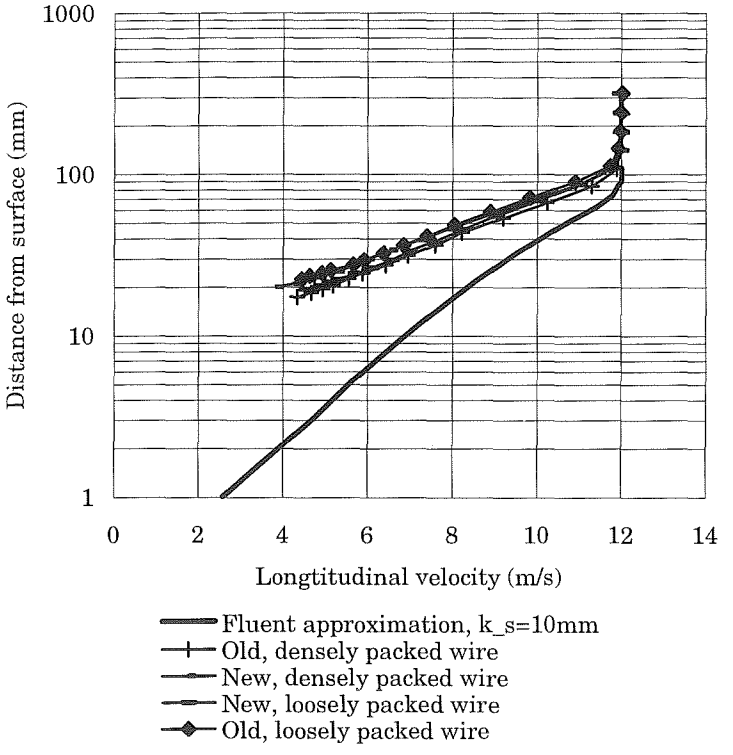

Figure 3.10. Velocity profiles over fancy wires.

Table 3.7. Raw aerodynamic profiles of fancy wires.

Surface type	Distance along surface (mm)	Direction of wires	z_0 (mm)	k_s (mm)	u^* (m/s)
Fancy #1	2 400	downwind	7.7	231	1.58
Fancy #2	2 400	downwind	5.1	153	1.39

Fancy #3	2 400	downwind	6.6	198	1.55
Fancy #4	2 400	downwind	6.4	192	1.55

3.5.2.2 CFD comparisons

Since the model was insensitive to sand roughness heights greater than 10 mm, it became quickly apparent that the Fluent's explicit rough wall approximation could not model the fancy wire velocity profile accurately. The comparison of k_s = 10 mm is shown on Figure 3.10. A fine grid was made very close (1 mm spacing) to the surface so an accurate velocity profile could be obtained for all simulations. Changing the grid size from 1.0 to 0.5 mm made little difference to the modelled profile.

To overcome the deficiencies of Fluent's sand roughness model, the porous media model was used to determine whether it would improve the accuracy of the CFD output. The porous height was initially set at the projected height of the wires, and trial and error was used to obtain a value for C_2 that made the prediction best fit the experimental data. Assuming completely turbulent flow through the wires, the viscous term of the Ergun Equation used in Fluent (Equation 3.9) was dropped and C_2 was the only term that could be varied. The assumption of fully turbulent flow is based on the experimental results of high turbulence intensities approaching the wires (over 30%) and the good agreement to the turbulent log-law term for the experimental data close to the wires. Laminar flow is only likely to be taking place less than 1 mm away from the surface, which is only a small fraction of typical wire heights. This being the case, the dominating flow regime will be turbulent, and only using the turbulent term in Equation 3.9 is a good approximation. The distance reference frame of the experimental data was shifted by the wire height (i.e z = 0 at the tips of the wires rather than the surface) to make valid comparisons.

Figure 3.11 gives an example of Fluent output using d = 18 mm and C_2 = 1/m. There is an improvement in predictions using the porous model but varying C_2 only tended to shift the velocity profile along the x – axis (velocity). As C_2 was increased, the porosity decreased and the profile shifted towards the origin. The converse was true as C_2 was decreased. Furthermore, the log-law region of the boundary layer which was readily apparent in Figure 3.10 was not followed when the reference point of origin was shifted to the tops of the

wires. There was no straight line to determine u_* and be able to extrapolate to ln z = 0 to obtain z_0.

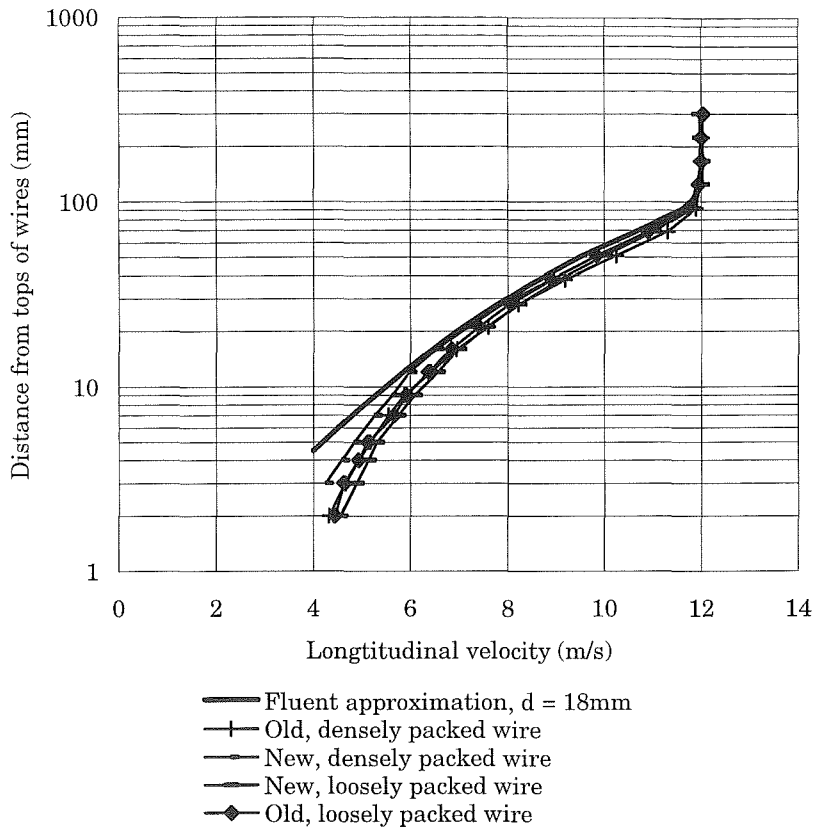

Figure 3.11. Velocity profiles with reference point shifted to tops of the wires.

Close agreement was finally reached when the porous height was set below the value of the roughness elements, i.e. a displacement depth (d) was used in the experimental data. It was incorporated into the data by altering the log-law equation (Equation 2.13) in the following way:

$$\frac{U}{u^*} = \frac{1}{\kappa} \ln \frac{z-d}{z_0} \tag{3.10}$$

This yielded the same equation as Mulhearn used to find a better agreement to experimental data. Equation 3.10 was rearranged to yield

$$\ln (z-d) = \ln z_0 + \frac{\kappa}{u^*} U \tag{3.11}$$

The best agreement was reached between using the following values for displacement depth, which then set the porous height ($k - d$) to be used in Fluent (Table 3.8). After trial and error, the appropriate C_2 values were found which gave the best fit to the experimental

data. Once the optimum displacement depths and C_2 values were found and used in Fluent, the corresponding output velocity profile were all virtually identical to each other and could all be approximated by one line (Figure 3.12).

Table 3.8. Optimal porous heights for fancy wires, with corresponding C_2 values.

Surface type	d (mm)	$k - d$ (mm)	C_2 (1/m)
		2.5	80
Fancy #1	15	3	50
Fancy #3	11.5	4	25
Fancy #4	16.5	4	25
Fancy #2	13	4.5	20
		5	15
		6	10
		8	5.7
		10	3.8

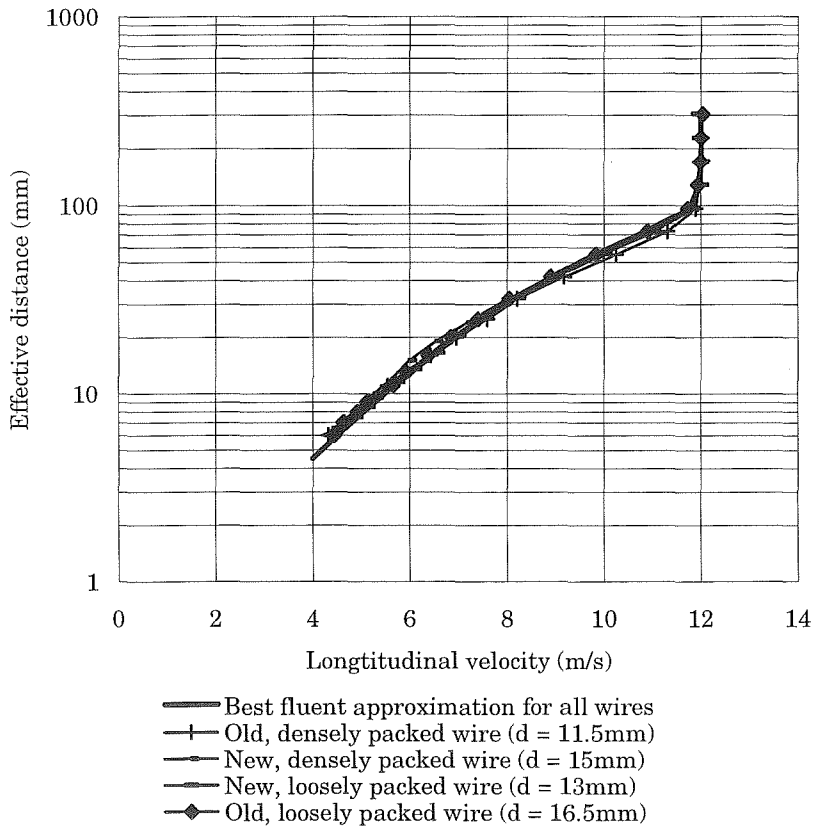

Figure 3.12. Corrected velocity profiles over fancy wires.

There was a trend noticed between increasing porous height and optimal C_2 values, a relationship that could be expressed as:

$$C_2 = 567(k-d)^{\frac{-20}{9}} \tag{3.12}$$

What was now required was a relationship to estimate displacement depth for any given roughness parameters. It is known that increasing element density causes a skimming effect and may be directly related to displacement depth. There are many definitions for element density used by various authors in their variants of Nikuradse's law. They are functions of several roughness parameters such as wire length, wire height and flat surface area per element and are given in Table 3.9.

The carding wire parameters given in Tables 3.1a and 3.1b were used in these equations. The accuracy of each equation was determined by calculating the spread of the constant coefficient obtained from the equation below:

$$d = \text{(constant coefficient)} \times \text{(element density)} \tag{3.13}$$

Table 3.9. Accuracy of each element density definition.

	Coefficients					
Wire type	Dvorak t/s	Simpson $1/\lambda$	Wooding $1/(\lambda\psi_1^{0.4})$	Dirling $1/(\frac{\sqrt{A_f}}{k}\beta^{\frac{4}{3}})$	Sigal $1/\lambda\beta^{1.6}$	Waigh $1/(\lambda\psi_2^{0.55}\beta^{1.38})$
Swift #1	9.4	7.2	15.2	1.95	9.21	29.0
Swift #2	10.8	6.4	15.0	1.67	8.02	29.1
Fancy #1	56.1	23.3	92.1	3.23	28.7	233
Fancy #2	69.2	29.7	113.8	4.05	36.8	247
Fancy #3	53.7	29.6	116.1	3.07	36.0	301
Fancy #4	64.1	33.3	119.1	4.44	41.5	307
Ave (fancy wires)	60.7	29.0	110.2	3.70	35.7	272
Ave % error (fancy wires)	9.7	9.8	8.3	14.8	9.8	11.7

There is a spread of values for the constant terms for all variations of element density for fancy wires with little to distinguish between the correlations. It may seem to be surprising that the simplest correlation used by Dvorak gives a better fit than Waigh's equation. It could be that the element density seems to be independent of the frontal area for the wires used. But the wire pattern is such that looking down the strips, there are discrete rows with sizeable gaps (up to 3 mm) between them. The air could be encountering less resistance through these gaps and streamlining through them. The airflow profile could be such that the velocity is lowest immediately upwind and downwind of the wires, creating a psuedo-roughness element similar to a long (or even corrugated) bar orientated streamwise. This would have the effect of minimising the effects of frontal area.

Since all of the wires tested were inclined around 30°, the bluntness parameter was constant for all the wires. Thus it is not yet known if a change in wire inclination changes the air drag, although it is known from the results presented in Section 3.4.1.3 that the wires orientated upstream drag more air than those downstream (despite the bluntness factor being the same).

It is noted that the old fancy wires which are either dirty or bent, should have different values of thickness and spanwise aspect ratio (a measure of the streamlining between the rows of wires) than those used, which assumes clean, straight wires. Only Waigh's equation takes both of these parameters into account. If the effective thickness of the old dense fancy wire was increased and the spanwise ratio decreased by the optimal amounts (16% and 23% respectively), the spread of coefficients falls to 3% and Waigh's formula becomes the most accurate. This assumes the dirt, which is primarily located near the bottom of the wires, still has an effect on air drag.

For a robust equation estimating element density, Waigh's equation is recommended for carding wire laid over a flat surface. Using the optimal coefficient from Waigh's equation yields the complete equation for displacement density as a function of element density,

$$d = 272(\lambda^{-1}\psi_2^{-0.55}\beta^{1.38}) \qquad (3.14)$$

Simultaneously solving the Fluent porous height equation and the element density equation gives:

$$k - d = k - 272(\lambda^{-1}\psi_2^{-0.55}\beta^{1.38}) \qquad , d \leq k$$

$$k - d = 0 \qquad , d \geq k$$

Both of these equations apply primarily for fancy wires. The second equation in each case is given since in the case of some swift wires, the calculated displacement depth is greater than the roughness height. This is in spite of the finding that setting $d = k$ gives satisfactory results for the swift wires studied.

With these correlations obtained, knowledge of the relevant roughness parameters for any carding wire can be directly used to calculate $k - d$ and C_2 for input into Fluent.

3.5.2.3 Boundary layer development

The boundary layer depths were calculated using the optimal displacement depths calculated in Section 3.4.2.2. The results are given in Table 3.10.

Table 3.10. Boundary layer data for fancy wires using optimal displacement depths.

Wire type	Distance along surface (mm)	Direction of wires	δ (mm)	δ^* (mm)	θ (mm)	δ/δ^*	δ/θ
Fancy #1	2 400	Downwind	112.7	26.0	14.3	4.33	7.88
Fancy #2	2 400	Downwind	109.2	25.7	14.3	4.25	7.64
Fancy #3	2 400	Downwind	94.7	24.1	13.1	3.93	7.23
Fancy #4	2 400	Downwind	117.6	26.4	14.8	4.45	7.95

Note that the relationship between porous height and boundary layer thickness is less apparent, and the boundary layer displacement is relatively constant for all types of fancy wires. The average displacement depth of the fancy wires was 26 mm. This compares to 15 mm for the swift wires using the same bulk air velocity. Thus the fancy wires drag some 73% more air than do the swift wires.

3.6 Conclusions

The experimental velocity profiles as a function of distance from the carding wire surface were consistent with the boundary layer theory over rough surfaces. There was a log-law region evident from which roughness parameters such as aerodynamic roughness height and friction velocity could be obtained. For swift wires, the closest approximation estimating aerodynamic roughness height in the literature was given by Waigh, and was a function of

element projected height and width, as well as spacing between elements. The inclination of the wires did not significantly affect the aerodynamic roughness height but affected the boundary layer depth. The velocity profiles for the short swift wires could also be accurately predicted using CFD simulations.

The longer fancy wires also showed the characteristic log-law velocity profile, and possessed a larger boundary layer. However CFD simulations could not accurately model the experimental results until a porous media was introduced to mimic the drag of the wires. This improved the comparison but a displacement depth was also required. By using the displacement depth, the depth of the porous media could be varied, and by using the combination of porosity and displacement depth as variables, the CFD simulation was able to match the experimental profiles. A formula was used to predict displacement depth and porosity as a function of the rough surface geometry for flat surfaces. Work detailed in Section 4 will confirm whether similar wires yield similar displacement depths and porosities for rotating surfaces.

4 TWO-DIMENSIONAL AIRFLOW BEHAVIOUR AROUND A SINGLE ROTATING CYLINDER

4.1 Introduction

The work in this section was a logical progression from the flat surface work on rough surfaces. It includes the effects of centrifugal forces on fluid flow and determines whether the experimental roughness parameters obtained from the flat surface work hold for rotating surfaces.

This section also includes the CFD modelling of a rotating cylinder and comparison of the results with open literature and experiment. It also determines whether the universal velocity profile found for boundary layer flow over flat surfaces holds for rotating surfaces if Furuya's corrections for curvature effects are used.

4.2 Setting up the CFD model

4.2.1 Defining the problem and grid set-up

For purposes of modelling the rotating cylinder in Fluent, the cylinder was differentiated into the solid, smooth roller and the carding wire clad around it. The carding wire was modelled as a moving porous medium with varying depth and permeability. An outer boundary was also a necessary input. The solid roller diameter was set at 107 mm radius, which is the radius of the control rollers to be used in subsequent experimental work.

The outer boundary interactions were minimised by extending the outer boundary. Although the outer boundary is ill defined in reality, Fluent requires a more definite description of the outer boundary, and it is influential in the fluid flow if it is placed near the inner cylinder. Recognising that the fluid flow is symmetric in the tangential direction, the outer boundary was defined as a cylinder in Fluent to further minimise boundary effects. Let the boundary layer depth be defined as the distance from the cylinder where the angular velocity is 1% of the rotating cylinder. Taylor's equations describing fluid flow between concentric rotating cylinders show that the boundary layer increases as the outer cylinder size is increased. For the case of our 107 mm radius roller, it was not until the outer cylinder was extended to at least 5 metres radius (about 50 times the inner cylinder) before the increase in boundary

layer became insignificant. Knowing this, an outer to inner cylinder radius ratio of about 100 was chosen for all simulations. The outer cylinder was treated as a stationary wall.

The two zonal wall model was used; this was the only near-wall treatment that attempted to predict the flow within the viscous sublayer although the grid points may be sparse or non-existent within the sublayer. Predictions were more accurate by ensuring at least one grid point was immersed within the sublayer. The closest interior grid point was calculated so that it corresponded to a z^+ value of around 10. This was about 0.2 mm for the case of the 107 mm roller rotating at 175 rad/s. The results from the RNG κ - ε turbulence model are used in the results; an attempt to use the RSM for the same problem resulted in diverging iterations.

Since the flow around the cylinder is symmetric in the tangential direction, not all the annular space between the two cylinders was required. Thus only one quarter of the annulus grid space was used, and periodic boundaries were set up 90° to each other (refer to Figure 4.1). The quarter roller grid sped up convergence fourfold, and when the roller speed was set slow enough (0.00175 rad/s corresponding to a Reynolds number of 1.3) that the flow was laminar throughout the annulus, the velocity profile was virtually identical to that predicted by Taylor (1923), giving us confidence in the CFD simulation results at this point. About 60 grid points were used on the quarter roller, and about 125 interior node contours were used, corresponding to approximately 7 500 nodes. By trial and error, underrelaxation factors were all set at 0.5, and normalised pressure and velocity residual tolerances set at 10^{-6} and 10^{-8} respectively. The second order discretisation scheme was used for all parameters, and the PISO algorithm was used for the pressure-velocity coupling. The solutions took between 5 000 – 15 000 iterations and lasted 2 – 6 hours on a Pentium II 400 MHz computer. A report summary for a smooth roller (107 mm radius) with no porosity is included in the Appendix.

4.2.2 Data input and analysis

4.2.2.1 Velocity profiles

The control used the 107 mm roller with no carding wire and a smooth surface, rotating at 175 rad/s. From this set-up, the effects of four variables were tested:

- Angular velocity, ω (5, 17.5, 50, 175, 500 rad/s)

- Roller radius, a (40, 107, 250, 625 mm)
- Porous media height, k - d (0, 2, 7, 20 mm)
- Porous media inertial resistance, c (2.5, 25, 2.5 × 10^{-6}/m)

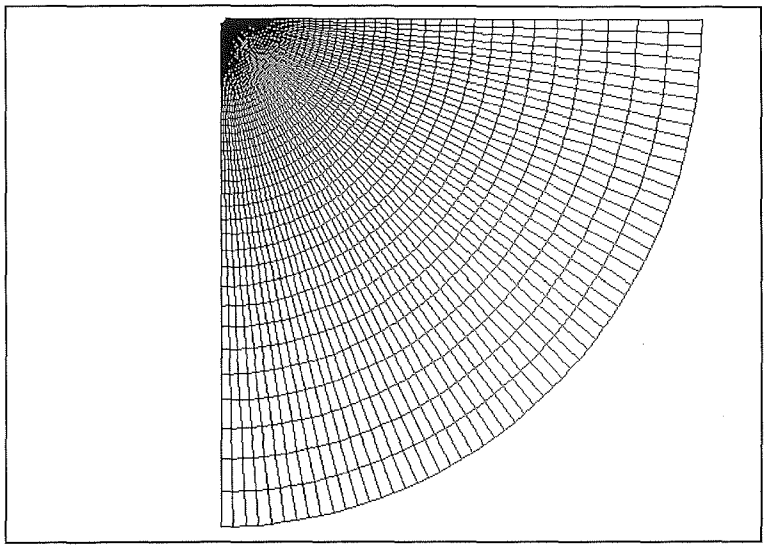

Figure 4.1. Typical grid structure.

The porous media terms were variables in Fluent's porous media model, explained in more detail in Section 3.2.1. It was quickly established that turbulent flow extends well into the roughness layer, noting that the roughness Reynolds number was over 90 in all but one case of the CFD simulations. The laminar term was therefore effectively dropped by making α excessively large.

The velocity profile results were initially plotted on linear plots of angular velocity defect versus distance. If there was a substantial linear relationship, i.e. if there were a few points embedded within the laminar sublayer, the frictional velocity was calculated from the slope by rearranging Equation 2.3a and using the angular velocity defect term:

$$z = \frac{\mu}{u_*^2 \rho}\left(U_w - \frac{a}{r}u\right) \tag{4.1}$$

This is called the implicit (laminar) method in Section 4.3.1. If a straight line could not be obtained, then a semi-log plot of angular velocity defect vs. distance was plotted, the slope and intercept determined and the frictional velocity obtained by rearranging Equation 2.13 and using the angular velocity defect term:

$$\ln z = \ln z_0 + \left(U_w - \frac{a}{r}u\right)\frac{\kappa}{u_*} \tag{4.2}$$

This is called the implicit (log-law) method in Section 4.3.1. The approach to finding the frictional velocity has the disadvantages of involving the Von Karman constant, which Nakamura (1986) found may not be constant for rotating cylinders. It also assumes curvature effects away from in the log-law turbulent region are negligible and do not affect the slope of the line.

Once friction velocities were obtained, u^+ vs. z^+ plots were generated. As expected from the literature, the fit within the laminar sublayer was good, up to about $z^+ \approx 5$, but became dependent on the cylinder Reynolds number in the turbulent regime. Furuya's equations were then used to generate u^+ vs. z^+ plots for the rollers. For smooth rollers,

$$\frac{U - \frac{a}{r}u}{u_*} \text{ was plotted against } \frac{au_*\rho}{\mu}\frac{\left(r^2 - a^2\right)}{2r^2}$$

While for 'rough' rollers,

$$\frac{U - \frac{a}{r}u}{u_*} + \left(\frac{1}{\kappa}\ln\frac{z_0 u_*\rho}{\mu} + 5.0\right) \text{ was plotted against } \frac{au_*\rho}{\mu}\frac{\left(r^2 - a^2\right)}{2r^2}$$

4.2.2.2 Friction coefficients

Friction coefficients can be determined from frictional velocities using Equations 2.2 and 2.42c. Several researchers have plotted frictional coefficients as a function of Reynolds number. They include the following equations given in Table 4.1. Most of these equations are variation of Theodorsen's equation (Equation 2.42a).

Table 4.1. Various equations for determining friction coefficient.

Researcher	Equation
Theodorsen	$\sqrt{\frac{2}{C_f}} = \frac{1}{\kappa}\ln\left(\mathrm{Re}\sqrt{\frac{C_f}{2}}\right) - 1.2$
Nakamura	$\sqrt{\frac{1}{C_f}} = 3.09\log\left(\mathrm{Re}\sqrt{C_f}\right) + 4.79$
Williamson	Figure 4.8 ($k_0 = 0.06$)

Dierich	$\sqrt{\frac{2}{C_f}} = \frac{1}{\kappa}\ln\left(\mathrm{Re}\sqrt{\frac{C_f}{2}}\right) - 0.04$
Modified Nakamura (in Dierich)	$\sqrt{\frac{2}{C_f}} = \frac{1}{\kappa}\ln\left(\mathrm{Re}\sqrt{\frac{C_f}{2}}\right) + 2.2$

The friction coefficients from this work are compared with published results.

4.2.2.3 Shear force moments

The wall shear stress and eddy viscosity profile can also be obtained directly from Fluent output, denoted the Explicit Method in Section 4.3.1. Noting the relationship between wall shear stress and frictional velocity (Equation 2.2), the values were compared between the three methods used.

Since all correlations used by the researchers assume a constant shear stress or shear force moment extending well into the fluid from the wall, an analysis was completed to determine if this was valid. Converting the combined eddy and molecular viscosity data from Fluent using the following equation and Equation 2.3,

$$\tau = (\mu + \varepsilon)\frac{\Delta u}{\Delta z} \tag{4.3}$$

a plot was obtained showing the ratio of $r^2\tau$ to $a^2\tau_w$ for smooth surfaces.

4.3 Experimental method

All work involving rotating rollers was conducted on a test rig built by WRONZ that could support two 940 mm wide rollers (Figures 4.2 and 4.3). The rollers, which could be of variable diameter and carding wire type, were driven off 2.2kW motors controlled by GEC Ranger CCI 340 variable speed drives. All rollers were 940 mm across. Air velocity measurements and data analysis were taken with the same system as used in the flat surface work. The probe could be positioned to an accuracy of 0.1 mm in the radial and axial direction using a computer controlled traverser constructed by the University of Canterbury Mechanical Engineering Department. Some 10 – 12 sets of readings would be taken in a vertical traverse up to a distance of 150 mm from the rotating surface. Side walls were installed to minimise edge effects in the 2D work. This was confirmed with traverses ¼ and

¾ way across the roller producing velocity readings of less than 5% difference to those recorded at the half way mark.

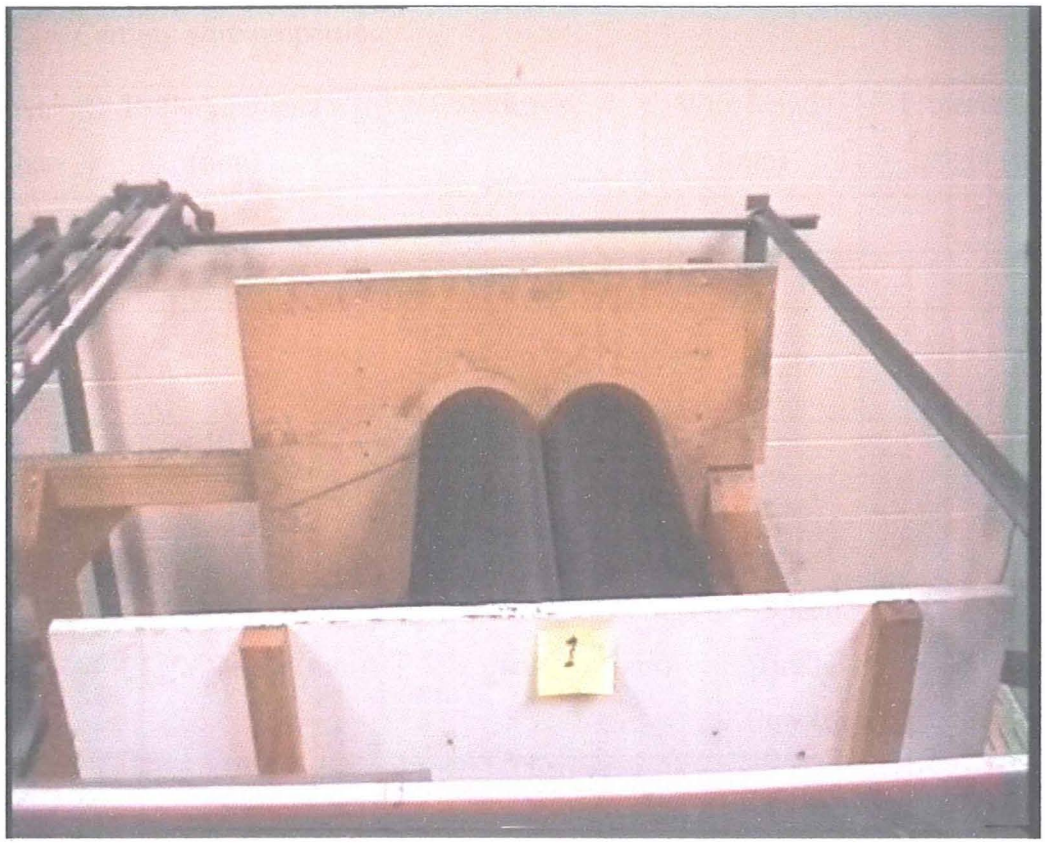

Figure 4.2. Rig showing two rollers and side walls to minimise 3D edge effects.

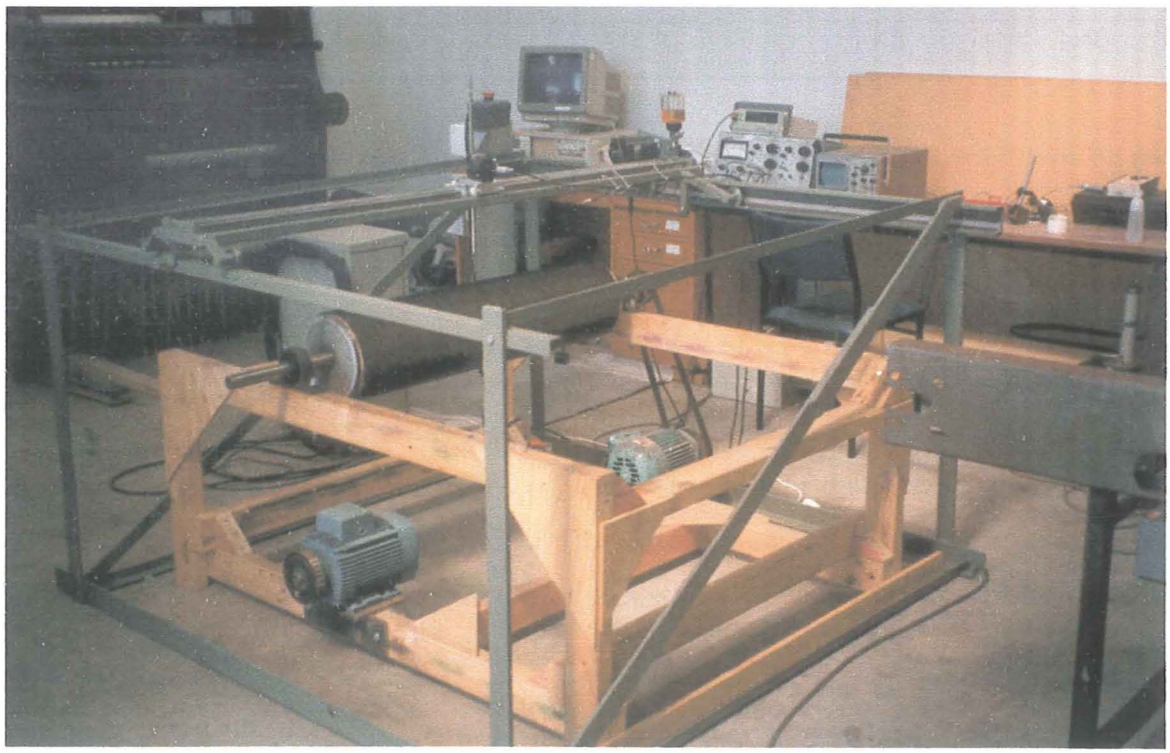

Figure 4.3. Test rig units with side walls removed for 3D work.

Tables 4.2a and 4.2b give the geometries of the roughness elements for the carding wire used in experimental work. The spacing distances were measured at the wire tips.

Table 4.2a. Carding wire properties.

Roller number	Roller diameter (mm)	Comments	Wire length (mm)	Projected wire height (mm)
1	214	Short wires	8.0	7.0
2	214	Long fancy wires	28.5	25
3	214	Short wires, less densely spaced	8.5	7.5
4	107	Short wires	7.5	6.5

Table 4.2b.

Roller number	Thickness parallel to flow (mm)	Thickness normal to flow (mm)	Spacing parallel to flow (mm)	Spacing normal to flow (mm)
1	0.45	0.35	1.30	1.28
2	0.58	0.40	6.40	3.20
3	0.60	0.40	2.60	1.70
4	0.35	0.30	1.45	1.40

Note that due to resource constraints it was not possible to use the same wire used for the flat surface experiments for the rotating roller experiments. The rollers were provided by WRONZ with wire already wound around them, and this existing wire was tested.

From results obtained from flat surface experiments, there was likely to be a displacement depth involved in the equation that would complicate calculations. Knowing this, the raw data was obtained and initially graphed on a semi-log plot of distance versus normalised angular velocity defect, using the distance from the tops of the wires to the probe as the nominal distance. Then various displacement depths were added to the raw data to alter the slope of the trendline. CFD plots of airflow profile were then generated for a variety of inertial resistance factors and porous depths. An example is given in Figure 4.4. The trendlines were then compared to these CFD nomographs to determine a best fit for displacement depth and porosity.

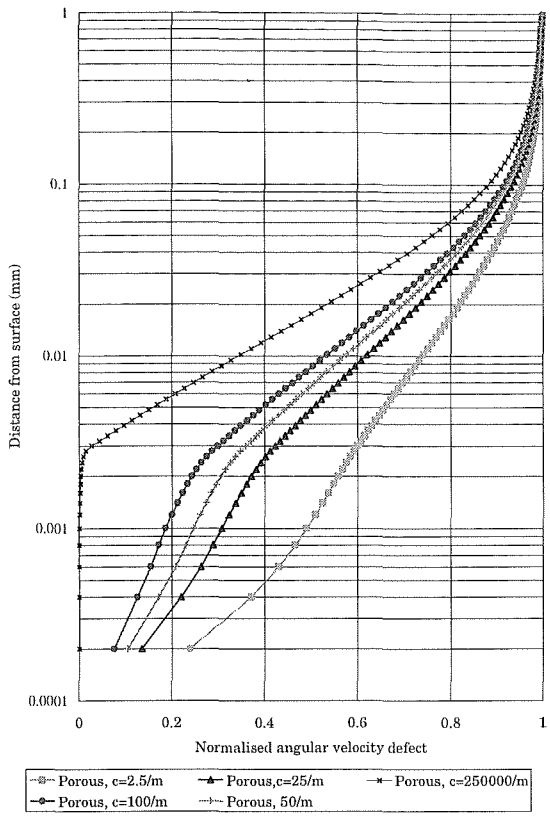

Figure 4.4. CFD nomograph for roller with displacement depth of 3 mm.

Angular velocities have been used to quantify flow profiles rather than linear velocities in this section. Three reasons are given, detailed in the following paragraphs.

1. The literature review showed that researchers typically used angular velocities to describe flow around a rotating cylinder. Thus the formulae and graphs can be better compared to their work. More recent research all used corrections for curvature effects to improve formulae describing this flow. Angular velocity takes curvature effects into account, whereas linear velocity does not.

2. For the same roller surface speed, the boundary layer depth (defined here as the radial distance away from the surface where the velocity is 1% that of the cylinder surface speed) increases as the outer boundary increases. A boundary layer depth concept based on angular velocity stopped increasing as the outer boundary or 'cylinder' was extended to about 50 times the radius of the inner rotating cylinder, and the velocity profile within 10 times the radius of the rotating cylinder became independent of the outer boundary position (this was the basis for choosing the outer boundary in CFD simulations, as detailed in

Section 5.4.2). The boundary layer depth based on a linear velocity was still increasing with the outer boundary 1 000 times the radius of the rotating cylinder. This was an unrealistic CFD simulation considering 99.99% of the domain was of no use to this work.

3. For the case of rough rotating rollers with very high inertial resistance factors (low porosity), the linear velocity of the air entrained with the porous media moved faster than the roller surface speed. When this occurred it was unsure how to obtain parameters such as aerodynamic roughness height, which is based on extrapolating the velocity plot to $u = U_w$.

4.4 Results and discussion

4.4.1 CFD modelled velocity profiles for smooth rollers

Table 4.3 gives values of the friction velocity (in m/s) obtained from various methods of calculation for smooth rollers. Explicit values were obtained directly from Fluent, implicit values were obtained from the slope of the line on a linear plot for laminar flow, and a semi-log plot for turbulent (log-law) flow.

Table 4.3. Friction velocities for smooth rollers.

Roller radius (mm)	Angular velocity (rad/s)	Sublayer depth ($y^+ = 10$) (mm)	Explicit	Implicit (laminar)	Implicit (log-law)
107	5	4.4	0.033	0.032	0.006
107	17.5	1.5	0.095	0.093	0.048
107	50	0.6	0.236	0.226	0.168
107	175	0.2	0.711	0.637	0.738
107	500	0.08	1.84	1.32	1.90
40	175	0.4	0.340	0.340	-
250	175	0.1	1.49	-	1.52
625	175	0.05	3.14	-	3.31

If the benchmark Reynolds shear stress terms are not available, it is clear that determining the velocity gradient in the laminar sublayer is the most accurate method if several measurements can be made within the sublayer. Otherwise obtaining the velocity gradient

within the log-law section of the turbulent boundary layer is the best method, but is less accurate.

Figure 4.4 shows normalised plots of universal velocity distribution for smooth rollers using the standard equations for normalised velocity defect and distance from the roller surface. As expected from the literature review, the laminar sublayer fits the theory but the turbulent region is dependent on the angular velocity of the roller.

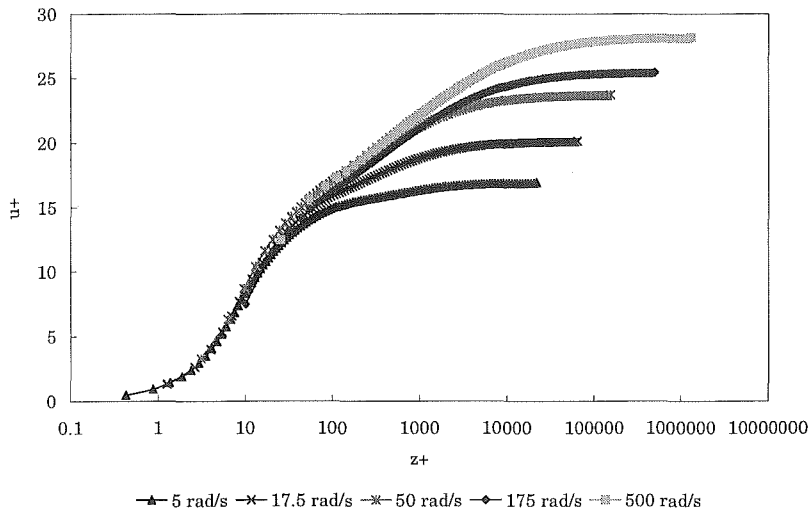

Figure 4.4. Universal velocity profile for rotating cylinders without curvature correction.

Figure 4.5 shows normalised plots of universal velocity distribution for smooth rollers using Furuya's formulae for dimensionless angular velocity defect and distance that take curvature effects into account. The laminar best fit curve fits $u^+ = z^+$, while the best fit line for the turbulent boundary layer reads:

$$u^+ = 2.5 \ln z^+ + 5.0 \qquad (4.4)$$

corresponding to a value for κ of 0.40.

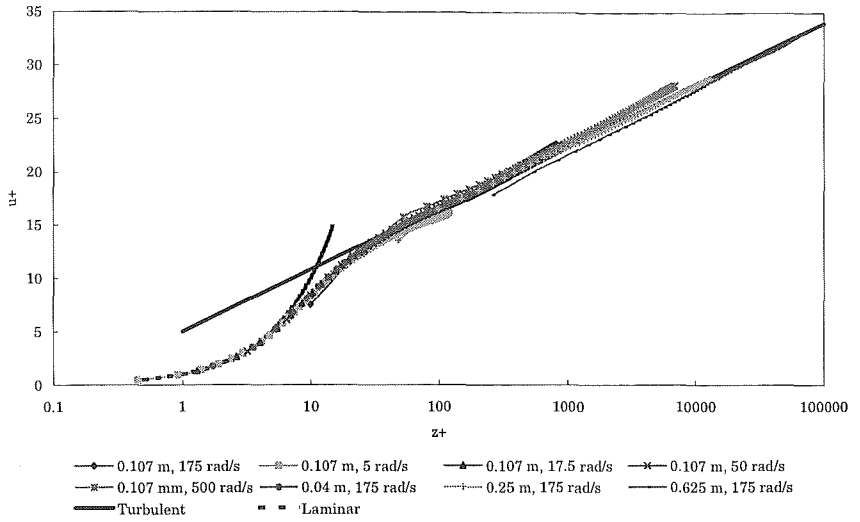

Figure 4.5. Universal velocity profile using Furuya's equations.

4.4.2 CFD modelled shear force moments for smooth rollers

Figure 4.6 shows the relationship between shear force moment and distance away from the roller surface. The normalised moment approaches unity within 1 mm from the roller surface, and drops to about 75% at distance $z = a$ from the surface. It is in reasonable agreement with Nakamura's results. Although the shear force moment continues to fall further away from the surface, it is still about 60% of the wall shear force moment 1 metre away from the surface.

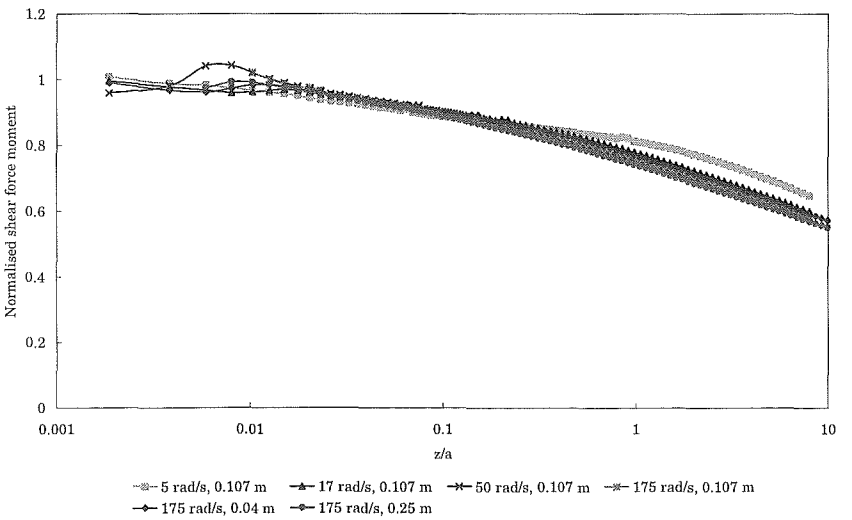

Figure 4.6. Normalised shear force moment for smooth rollers.

4.4.3 CFD modelled friction coefficients for smooth rollers

Figure 4.7 compares the friction coefficients obtained from the smooth roller with the equations given in Table 4.1. The Nakamura and modified Nakamura equations provided the best fit. The other correlations tended to overestimate the friction coefficient compared to those obtained using CFD simulations. As mentioned in the literature review, Nakamura suggested that some discrepancies were attributable to the influence of an outer roller. The physical roughness of the experimental cylinders, however small, could also be having an effect, especially considering the simulated rollers used in this work were 'perfectly smooth' by definition.

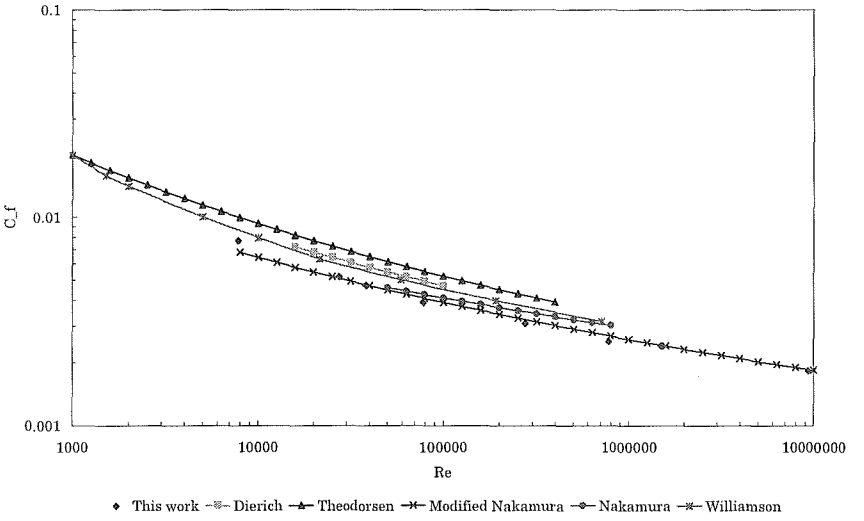

Figure 4.7. Comparisons of friction coefficient correlations for rotating cylinders.

4.4.4 CFD modelled velocity profiles for rough rollers

Table 4.8 gives the friction velocity values for the roughened 107 mm, 175 rad/s rollers; the laminar sublayer is immersed within the carding wire and could not be measured in reality. The wall shear stresses determined by Fluent are also inaccurate due to the influence of the carding wire. Thus the only direct measurement for this CFD simulation is the velocity gradient within the log-law region of the turbulent boundary layer. The specifications are given in porous depth (mm) and inertial resistance factor (1/m).

Table 4.8. Roughness properties for rough rollers.

Specifications	z_0 (mm)	Explicit	Implicit (turbulent)
2 mm, 2.5 /m	0.01	-	0.846
2 mm, 25 /m	0.11	-	1.16
2 mm, 250 000 /m	1.8	-	1.94
7 mm, 2.5 /m	0.1	0.436	1.08
7 mm, 25 /m	1.0	0.225	1.63
7 mm, 250 000 /m	6.4	0.0003	2.70
20 mm, 2.5 /m	0.9	-	1.46
20 mm, 25 /m	5.3	-	2.38
20 mm, 250 000 /m	17.5	-	3.89

The influence of roughened surfaces on the velocity distribution is clearly marked on Figure 4.9 for an arbitrary inertial resistance factor (C_2) of 25/m. Not only does the velocity decrease with respect to smooth surface velocity distribution, the slope of the velocity gradient increases with increasing roughness depth. This initially indicated a decreasing value of κ with increasing roughness depth, but it has been well documented that κ remains constant between smooth and rough surfaces over a flat plate (Schlichting, 1979).

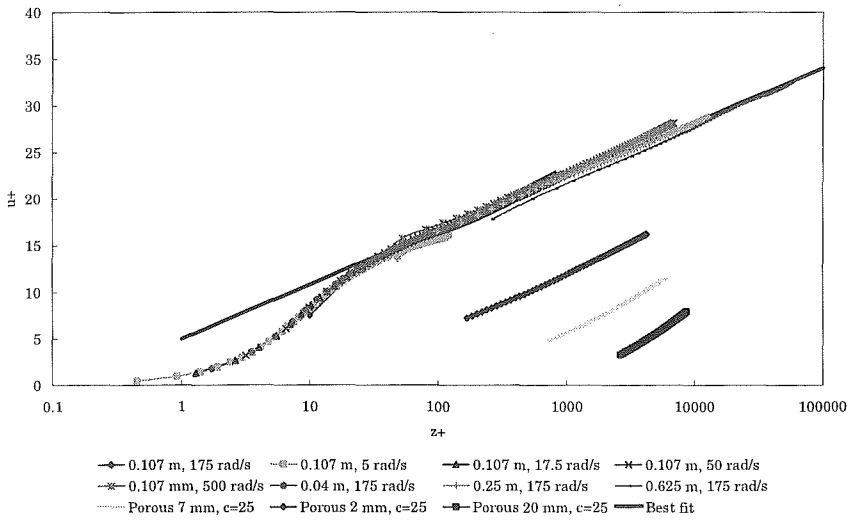

Figure 4.9. Comparison of velocity distribution between smooth and rough roller surfaces.

Instead, the method of finding u_* was put under scrutiny. The only method available using CFD simulations was from the velocity gradient in the log-law region (data on Table 4.3).

However the value for u_* obtained for this method is only valid in the fluid approaching the clothing wire due to the reduction in velocity defect within the wires. Thus the value u_* (and therefore τ) was that at the wire tips, not the roller surface. Adapting Equation 2.43b, we have

$$\tau_w = \frac{r_{wire\ tips}^2}{a^2}\tau_{wire\ tips},\ u_{*w} = \frac{r_{wire\ tips}}{a}u_{*wire\ tips} \qquad (4.5a, b)$$

The porous depth compensation improved the correlation between smooth and rough surfaces. However, the slope (and therefore κ) was still decreasing with increasing roughness depth, even after using Equation 4.5b. It is noted from Figure 4.7 that the shear force moment decreases and therefore Equation 4.5b is not entirely valid away from the roller surface. If Figure 4.7 can be used to provide a shear force moment compensation factor (K) according to the following equation,

$$r^2\tau = K\,a^2\tau_w \qquad (4.6)$$

$$\text{then } u_{*w} = \frac{1}{\sqrt{K}}\frac{r_{wire\ tips}}{a}u_{*wire\ tips} \qquad (4.7)$$

the friction velocity as obtained by velocity gradient has now been corrected for roughness depth effects and the deviation of the normalised shear force moment from unity. The K values as a function of the porous depths used in this work are given in Table 4.5. Adding the factor gives a much better fit on a universal velocity profile plot and κ values are around 0.40, as for the smooth rollers.

Table 4.5. Shear force moment compensation factors.

Porous depth (mm)	K (obtained from Figure 4.7)
2	0.97
7	0.91
20	0.86

With a friction velocity correction calculated, the roughness correction factor using aerodynamic roughness heights:

$$r^+ = \left(\frac{1}{\kappa}\ln\frac{z_0 u_*\rho}{\mu} + 5.0\right) \qquad (4.8)$$

can be added to u^+ obtained from roughened rollers to obtain a universal velocity distribution applicable to both smooth and rough rollers (Figure 4.10).

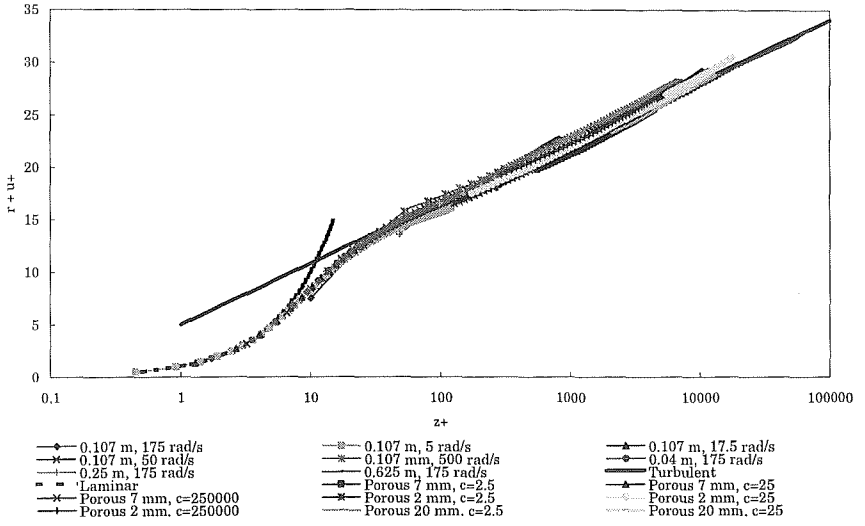

Figure 4.10. Universal velocity distribution using Furuya's correlations for all roller surfaces.

The results from Figure 4.10 suggest an excellent agreement to Furuya's equations, taking both the influence of surface roughness and curvature effects into account to yield the universal velocity distribution that is equivalent to that for a boundary layer over a flat plate.

Although Nakamura obtained a good fit to experimental data, the values of κ and A were different. It is known that κ and A are very sensitive to the friction velocity value and any errors would propagate into the universal velocity function as shown in Figure 4.9, but Nakamura obtained good agreement of u_* from two different sources. Despite the deviation of normalised shear force moment away from unity at long distance from the rotating cylinder, there is still a good fit between the data and Furuya's correlation. Noting Figures 4.9 and 4.10, the correlation tends to slightly underestimate u^+ when z is greater than distance $0.5a$ from the roller surface.

Note that the aerodynamic roughness height, z_0 can also be obtained for smooth surfaces, which can be compensated for using Equation 4.8. Where there existed a significant log-law boundary layer, z_0 was obtained from the $z = 0$ intercept. Table 4.6 gives these values and the roughness correction. By definition, the roughness correction factor should be zero, and the results from Table 4.6 give support to this prediction and confidence in the implicit (log-law) approach to find u_*.

Table 4.6. Aerodynamic roughness heights and roughness correction factors for smooth roller surfaces.

Roller speed (rad/s)	Roller radius (m)	Z_0 (mm)	Roughness correction factor
175	0.107	0.0026	-0.1
500	0.107	0.001	-0.1
175	0.250	0.0013	0.0
175	0.625	0.0007	0.4

At this stage it is prudent to mention some comparisons between the aerodynamic roughness height approach and the sand roughness height approach to compensate for roughness effects. The aerodynamic roughness height has been used in this work since it can be obtained directly from the velocity vs. log-distance plots and does not explicitly depend on u_*, κ, A and B well as roughness parameters such as element density and shape.

An attempt was made to calculate sand roughness height values from the simulations in this work to test the assumption that $k_s \approx 30\ z_0$, or at least k_s = constant $\times\ z_0$. Using Equation 2.10, substituting $A = 5.0$ and $B = -3.5$ (to maintain the constant of 8.5 in Equation 2.12), the roughness correction reads:

$$r^+ = \left(\frac{1}{\kappa} \ln \frac{k_s u_* \rho}{\mu} - 3.5 \right) \tag{4.9}$$

Assuming $\kappa = 0.40$, and using the friction velocities from each run, sand roughness heights could then be calculated. They are presented in Table 4.7 along with a comparison of aerodynamic roughness heights.

Table 4.7. Comparisons between aerodynamic and sand roughness heights.

Porous depth (mm)	c (1/m)	$\frac{k_s u_* \rho}{\mu}$	k_s (mm)	z_0 (mm)	k_s/z_0
2	2.5	24.5	0.41	0.01	41
2	25	299	3.7	0.11	34
2	250 000	1 640	48	1.8	27
7	2.5	299	3.7	0.1	37
7	25	3 640	29	1.0	29

7	250 000	19 700	144	6.4	23
20	2.5	7 330	49	0.9	54
20	25	32 900	133	5.3	25
20	250 000	111 000	533	17.5	31

Although the average ratio of k_s to z_0 from these runs is 33, the individual ratios vary considerably, generally decreasing as the inertial resistance factor increases. It can also be argued that the aerodynamic roughness height is a more meaningful value, approaching the porous height as the inertial resistance factor becomes very large. The sand roughness height has far less meaning at this point as its value becomes many times the height of the actual roughness elements.

4.4.5 Experimental results

Figure 4.11 gives the experimental data on a semi-log plot of normalised angular velocity defect as a function of distance from the wire tips, with no displacement depth used. Plots were then generated of each set of data, with various displacement depths added. Figure 4.12 shows an example for Roller 1 with the wires facing upwind. These were visually compared to the CFD airflow profile plots generated in Section 4.2. Table 4.8 details the effective porous depths and porosities that gave the best fit to the experimental data for the four wire types. This best fit data was graphed in Figure 4.13. The roller descriptions are given in Section 4.3.

Table 4.8. Best fit porous depths and inertial resistance factors.

Roller number	Direction	*k-d* (mm)	C_2 (1/m)
1	Upwind	2.5	95
1	Downwind	2.5	45
2	Downwind	25	15
3	Upwind	4	40
3	Downwind	4	25
4	Upwind	4	75
4	Downwind	4	40

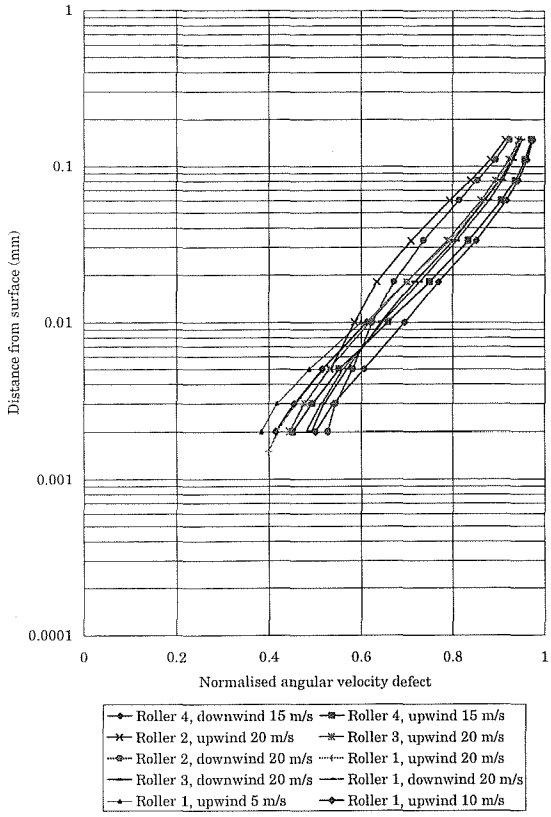

Figure 4.11. Raw airflow profile data.

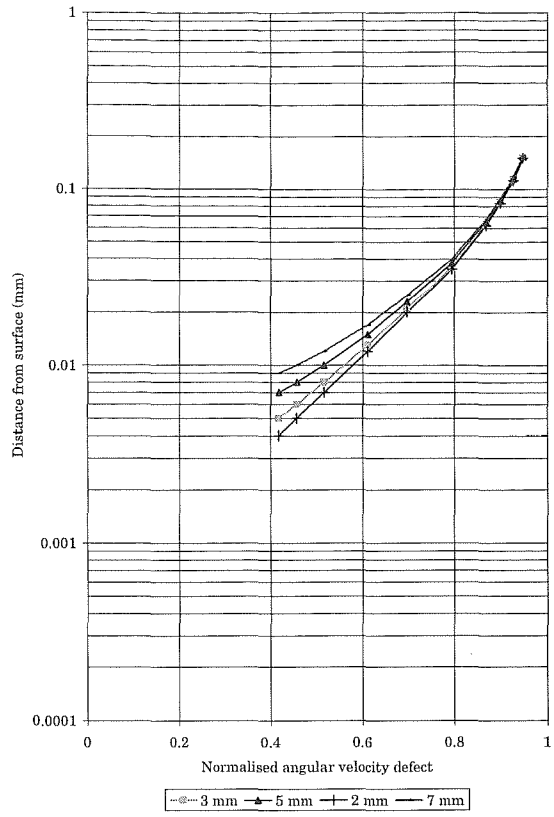

Figure 4.12. Roller 1 airflow data with added displacement depths.

With displacement depth and porosity now predicted, z_0 and u_* can then be determined from Figure 4.13 by extrapolating the experimental data to a zero velocity defect, then using Equations 4.2 with a displacement depth. Table 4.9 details these values.

Table 4.9. Rough surface properties.

Roller number	Direction	z_0 (experimental) (mm)	u_* (experimental) (mm)
1	Upwind	0.45	1.66
1	Downwind	0.22	1.47
2	Downwind	2.3	2.51
3	Upwind	0.55	1.71
3	Downwind	0.29	1.47
4	Upwind	0.60	1.55
4	Downwind	0.38	1.44

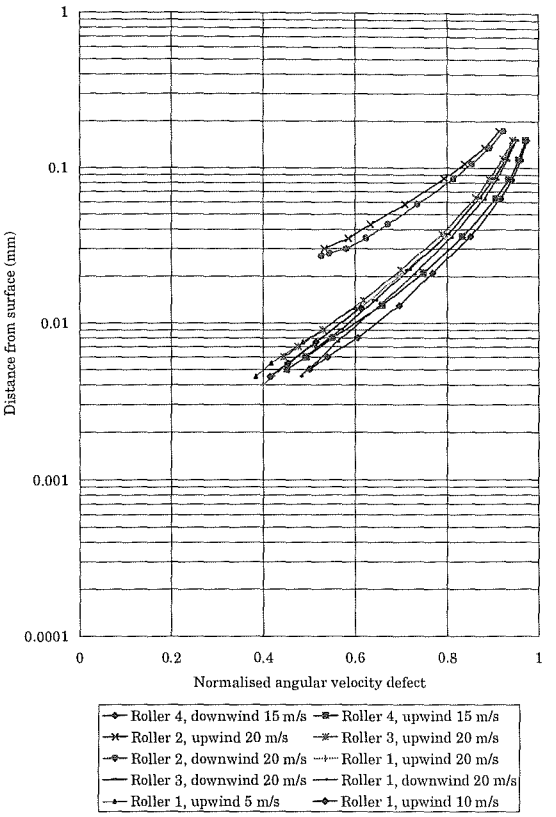

Figure 4.13. Airflow profiles corrected for displacement depths.

The data could then be plotted on a $r^+ + u^+$ vs z^+ plot using Furuya's equation adapted for rough surfaces (Equation 4.4 and adding Equation 4.8). Figure 4.14 shows the airflow data from all the rollers and the universal velocity profile approximation for rotating cylinders (Equations 2.4b and 4.4).

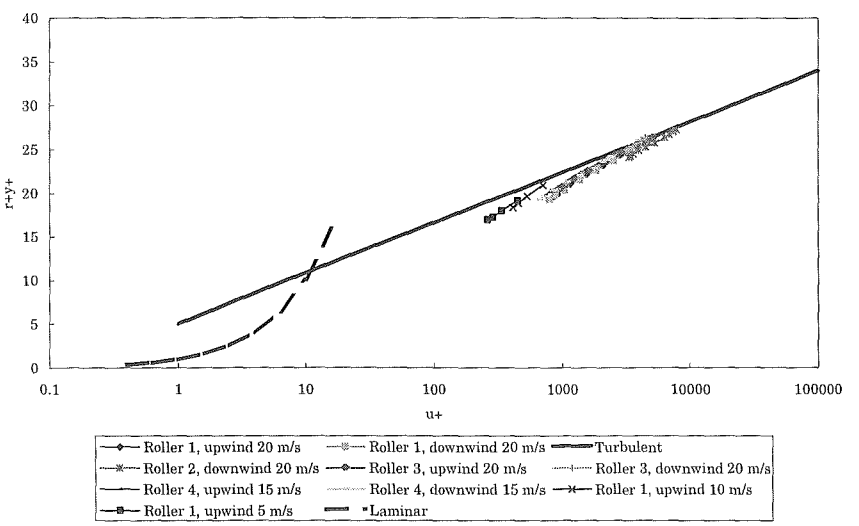

Figure 4.14. Universal velocity profiles for experimental rollers.

The slopes of all the data are higher than predicted, even after adding shear stress and displacement corrections. Reynolds Stress measurements were not made in these experiments, and it is possible that the CFD output may have overestimated Reynolds Stresses for rough surfaces. However the data as a whole lies very close to the universal velocity profile.

4.4.6 Predicting displacement depth and porosity using correlations

Table 4.10 gives a comparison of aerodynamic roughness height between the experimental values and those predicted by Waigh and Dvorak (detailed in Section 2.3.3.2). These two equations gave the most accurate roughness height values for the flat surface work. However only Waigh's equation gave reasonable estimates, accurate to about 30% error. The equations generated by other researchers and used for the flat surface work also gave widely inaccurate values.

Table 4.10. Aerodynamic roughness height comparisons.

Roller number	Direction	z_0 (experimental) (mm)	z_0 (Waigh) (mm)	z_0 (Dvorak) (mm)
1	Upwind	0.45	0.48	0.045
1	Downwind	0.22		
2	Downwind	2.3	1.5	11.5
3	Upwind	0.55	0.48	0.071
3	Downwind	0.29		
4	Upwind	0.60	0.66	0.38
4	Downwind	0.38		

As for the fancy wire in the flat surface work, the CFD data could not be fitted to the experimental data for the shorter wires without the use of a displacement depth. The use of a displacement depth implied that only a fraction of the wire height was being used to actively move air around the roller. Table 4.11 details displacement depths, corresponding effective wire height (= porous height used in CFD model) and inertial resistance factors.

Table 4.11. Best fit data for CFD porous model.

Roller number	Direction	d (mm)	k-d (mm)	C_2 (1/m)
1	Upwind	4.5	2.5	95
1	Downwind	4.5	2.5	45
2	Downwind	0	25	15
3	Upwind	3.5	4	45
3	Downwind	3.5	4	25
4	Upwind	2.5	4	75
4	Downwind	2.5	4	40

The trends in values for roughness parameters differed significantly between the flat and rotating surfaces. Whereas the short wires had no displacement depth when laid flat and air blown across them, in all cases the best fit was achieved when a displacement depth was used. The converse was true for the fancy wires; the best CFD fit for a rotating surface was when there was no displacement depth. As such, the equation used to predict displacement depth and porosity for roughness elements over flat surfaces did not hold for the rotating surfaces. A better set of correlations needed to be found.

A correlation between displacement depth and element density could be plausible since the displacement depth tended to increase for more densely spaced wires. A plot was generated of displacement as a function of element density ($1/\Lambda_w$) to ascertain if there was a definite trend (Figure 4.15). With the fancy wires being spaced the most sparse, there was no displacement depth. However for the short, densely spaced wires the displacement depth fraction increased as a function of element density. Drawing a best-fit line through the three points and extrapolating to $d = 0$ yielded a critical element density of approximately 0.035, below which no displacement depth was required. At element density values above 0.035 there possibly exists an air pocket near the roller surface that rotates at the same speed as the roller, reducing the effective height of the wires that can drag air, causing the displacement depth effect and reducing the amount of air pumped around the roller.

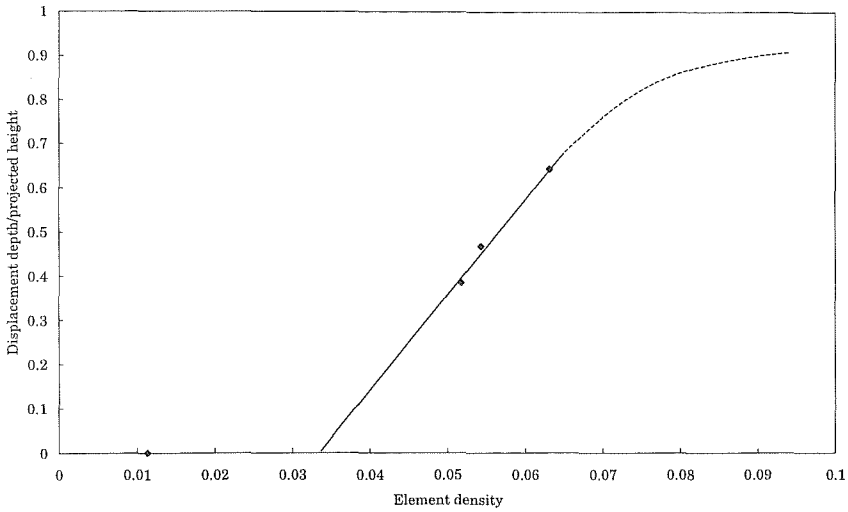

Figure 4.15. Displacement depth as a function of element density.

The following equations were used to graph the best-fit line for displacement depth:

$$d' = 22/\Lambda_w - 0.743, \qquad 0.035 < 1/\Lambda_w < 0.07 \qquad (4.10)$$

$$d' = 0, \qquad 0 < 1/\Lambda_w < 0.035 \qquad (4.11)$$

where $d' = d/k$

The phenomenon of a critical element density is not confined to rotating rough surfaces. The findings by the researchers mentioned in Section 2.3.3 all found there exists a certain 'element density parameter' (such as Λ_d or Λ_s), below which a skimming effect started to occur.

The reason why no displacement depth is occurring for the long fancy wires on rotating surfaces compared to stationary surfaces could be due to the helical pattern it is wound around the roller. Since the tangential airflow around the roller does not quite match the wire pattern, there is a diminished chance for the air to streamline past the wires. Thus the individual elements are all exposed to the airflow, and since the wires are more widely spaced, they are exposed right down to the surface of the roller.

The relationship between porosity and roughness geometries was more difficult to pinpoint. Wires pointing upwind had a higher porosity than those pointing downwind. With the wires pointing upwind, porosities varied between 65% and 110% over the same rollers pointing downwind, averaging 85%. A plot was generated of porosity as a function of element density for wires pointing downwind to find any trends (Figure 4.16). A best-fit line was

drawn through the points and extrapolated to the origin (since a smooth surface has no porosity). There was a trend of increasing porosity as a function of element density but there was a lot of scatter in the data. The following equations were used to the best-fit lines for porosity:

Wires facing upwind: $C_2 = 662/\Lambda_w$, $0 < 1/\Lambda_w < 0.07$ (4.12)

Wires facing downwind: $C_2 = 1225/\Lambda_w$, $0 < 1/\Lambda_w < 0.07$ (4.13)

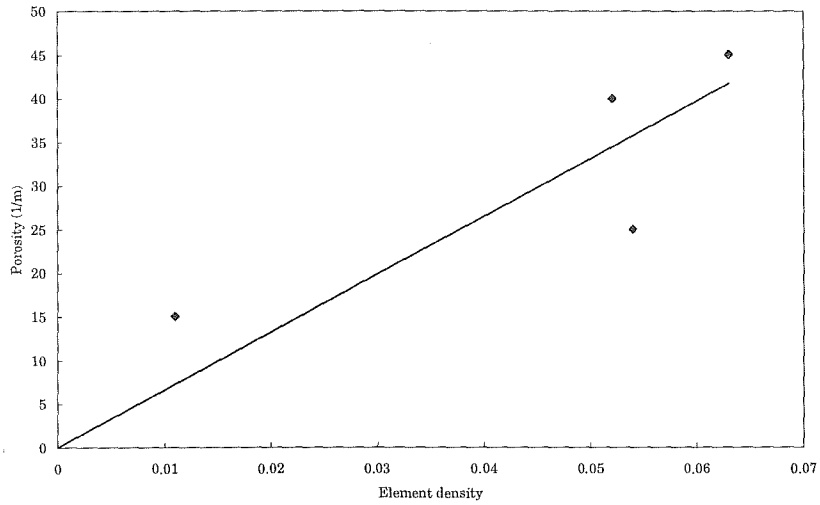

Figure 4.16. Inertial resistance factor (inverse porosity) as a function of element density.

It has been assumed all along that the porous media used in to model the wires in Fluent has a constant porosity from the surface to the wire tips. However the porosity values used are only an average value from the surface to the tips. In reality the porosity will change as a function of wire height since the spacing between the wires (and hence the element sparseness) is greater at the wire tips than at the roller surface. However it is impossible using the hotwire anemometry techniques used here to measure the air velocity within the wires and gauge the changing porosity, and it would complicate the porous media conditions used in Fluent.

4.4.7 Boundary layer development

The boundary layer depth and air pumping capability of the rollers was also determined from the time-independent CFD output. The boundary layer was defined as the point where the angular velocity was 1% of the angular velocity of the roller. Since the boundary layer depths vary between the rollers, the volumetric airflow generated by a 940 mm wide roller

was calculated out to a distance of 600 mm from the roller surface. This allowed for a more accurate comparison between the rollers of their ability to pump air.

The area-averaged air velocity from the roller surface to a depth of 600 mm was calculated using the following equation:

$$v_A = \frac{1}{A}\sum_{i=1}^{n} v_i A_i \qquad (4.14)$$

where A = area of each section i, m^2

The area-averaged air velocity was then multiplied by the chosen boundary layer depth and the roller width to obtain the volumetric flowrate across the roller, i.e.

$$Q = v_A \, \delta w \qquad (4.15)$$

where δ = boundary layer depth, m

w = width of roller, m

Tables 4.12 and 4.13 detail the volumetric flowrate of air generated by the rollers and shows that the roller with the fancy wire pumped some 2.5 times more air than the same sized roller rotating at the same speed with ordinary fillet wire. This was more than the 73% increase of air drag by stationary fancy wires on a flat surface.

Table 4.12. Boundary layer data from rollers with wires facing upwind.

Roller number	δ^* (mm)	U_w (m/s)	v_A (m/s)	Q (m^3/s)
1	470	20	1.50	0.85
3	480	20	1.60	0.90
4	280	15	0.95	0.54

Table 4.13. Boundary layer data from rollers with wires facing downwind.

Roller number	δ^* (mm)	U_w (m/s)	v_A (m/s)	Q (m^3/s)
1	430	20	1.30	0.73
2	730	20	3.20	1.80
3	440	20	1.40	0.79
4	260	15	0.85	0.48

4.5 Conclusions

The universal velocity profiles obtained from CFD simulations were found to closely match experimental data found in the literature, in that flow in the laminar region all fell on the one curve while flow in the turbulent region was Reynolds number dependent. If the curvature effects as suggested by Furuya et al (1978) were taken into account, all the data in the turbulent regime collapsed onto the one line and made the profile identical to that for flow over a flat plate. Nakamura's equations predicting friction coefficients were also the most accurate, and shear force moment profile obtained from this work also mirrored Nakamura's experimental results. With some compensation to the friction velocity obtained directly from velocity versus distance plots, the universal velocity profile for roughened rollers also fitted onto the same line by using a roughness correction, similar to that used for flat surfaces.

The experimental data could also be fitted to a universal velocity profile, although the slope of the line was higher than predicted. The shear stress estimates used could have been overestimated. The air pumping capabilities of the rough rotating rollers were also quantified, and showed that rollers clad with the fancy wire generated a larger boundary layer and pumped the most air of the wires evaluated.

The flat surface work described in Section 3 was useful to determine how different roughness geometries affect boundary layer flow and there was plenty of literature to compare it against. However it was of little use in predicting how rotating rough surfaces would behave.

5 THREE-DIMENSIONAL AIRFLOW BEHAVIOUR AROUND A SINGLE ROTATING CYLINDER

5.1 Introduction

A brief study was conducted into the 3D airflow patterns generated by rotating cylinders in a quiescent zone. It was proposed from the literature review that the 3D rotating roller, if narrow enough, would have flow patterns similar to a rotating disc, where the flow would move towards the roller axes and be flung out towards the disc edges. The literature review also showed the presence of Taylor vortices on concentric rollers that may also exist on single isolated rollers.

5.2 Experimental method

The same test rig was used as for the 2D single rotating roller. Roller 1 was used for all experiments in this section. The side walls were removed to introduce the edge effects. However only flow visualisation tests using smoke generation were used to ascertain semi-quantitative airflow profiles. The smoke was introduced via a long pipe underneath the roller, and the pipe was moved back and forth. The smoke profiles were video taped, converted to mpeg format and saved onto a compact disc. The disc is included in a pocket at the back of this thesis. The 3D roller flow visualisation experiments were labelled thus:

6. Roller rotating at a tip speed of 8 m/s
7. Roller rotating at a tip speed of 20 m/s
8. As for (7), but continuing to record after the smoke was turned off

Still frames were captured from the experiments.

5.3 Setting up the CFD model for the 3D rotating roller

There were five CFD examples of 3D rollers processed. The control case was based on Roller 1 type geometries, namely 214 mm diameter and 940 mm width. A surface speed of 18.6 m/s was chosen in each case. The five cases used the following conditions:

- 214 mm diameter, 940 mm width (aspect ratio 4.4), unbounded
- 1 372 mm diameter, 940 mm width (aspect ratio 0.7), unbounded
- 1 372 mm diameter, 2 744 mm width (aspect ratio 2.0), unbounded

- 214 mm diameter, 940 mm width, wall at distance 214 mm from roller surface
- 214 mm diameter, 940 mm width, wall at distance 107 mm from roller surface

A coarse grid was set to minimise iterating times, with the closest grid point to the surface being typically 2 mm away. The two-layer zonal wall treatment model was still used although it was recognised it could introduce some errors. However, as mentioned in Section 5.1, this project was not meant to include a fully quantitative analysis into 3D flows, but to find semi-quantitative trends and compare them with the open literature. The surface was made smooth by not using a porous media model and disabling the explicit roughness model, to reduce computational expense. For all cases, the outer boundary was cylindrical. For unbounded flow, the boundary was set one metre away from the roller surface and the 'pressure-inlet' wall condition used to minimise boundary effects. Other underlying conditions were as used in the 2D single roller set-up.

These simplifications still resulted in a grid with typically 200 000 faces that took at least 24 hours for 10 000 iterations. Two-dimensional CFD output was obtained from 'slicing' a plane along the $y-z$ axis through the axis of rotation of the cylinder.

5.4 Results and discussion

5.4.1 Unbounded rollers

Figures 5.1 and 5.2 show the flow patterns for CFD and experimental results respectively. The profiles are very similar despite the coarse grid used in Fluent. Although the primary flow patterns are tangential to the roller, the secondary flow patterns are dominated by the 'spinning disc' effect, the movement of air towards the centre of the roller along the axes and then flung out radially. The CFD output also predicted the flow or air moving radially towards the centre of the roller before being flung out (Figure 5.3). This was picked up by flow visualisation when the smoke, which was being introduced below the roller, was turned off and allowed to circulate around the room (Figure 5.4). The 'spinning disc' secondary flows were also evident in the smaller aspect ratio rollers (Figures 5.5 and 5.6). The formation of vortices along the cylinder may explain the occurrence on carding machines of an uneven web due to fibre migration across the card (WIRA, 1948).

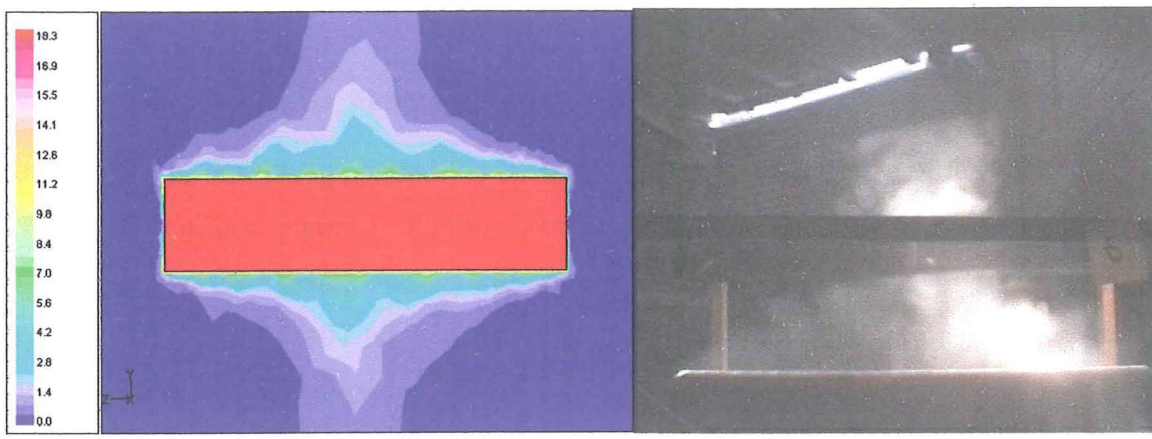

Figures 5.1 and 5.2. CFD output for velocity magnitude (m/s) and experimental flow visualisation results for 3D rotating cylinder.

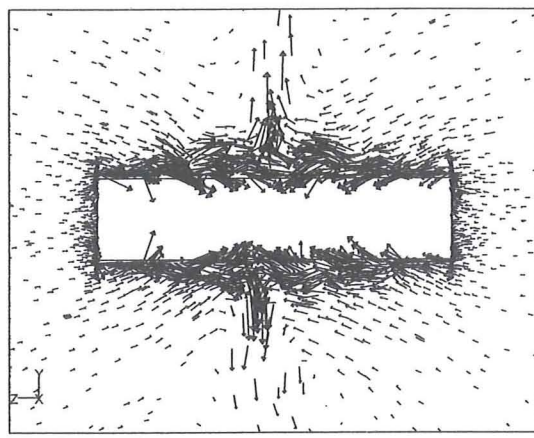

Figure 5.3. CFD output for velocity vectors.

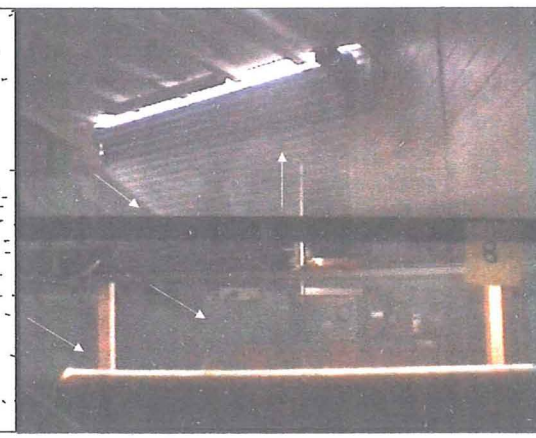

Figure 5.4. Flow visualisation results showing secondary flow patterns.

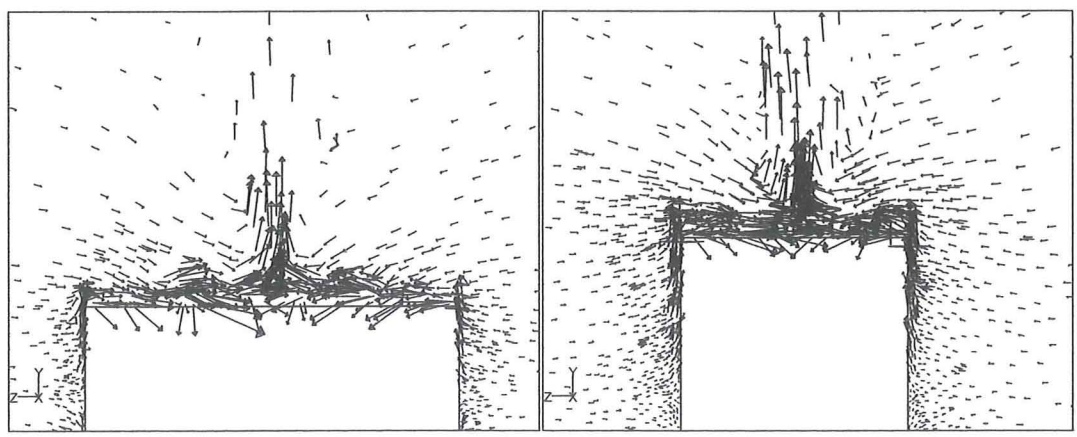

Figures 5.5 and 5.6. CFD output for velocity vectors on rotating rollers with aspect ratios of 2.0 and 0.7 respectively.

5.4.2 CFD predictions for bounded rollers

The addition of covers suppressed the radial flow out from the centre of the rollers (Figure 5.7). At a gap of one diameter, the flow becomes less streamlined, but there is still evidence of a toroidal vortex (Taylor vortex) forming at either side of the roller (Figure 5.8). If the gap is reduced to half (107 mm), the position of the major vortices move out towards the edges of the roller, while the flow looks more random near the centre of the roller (Figures 5.9, 5.10).

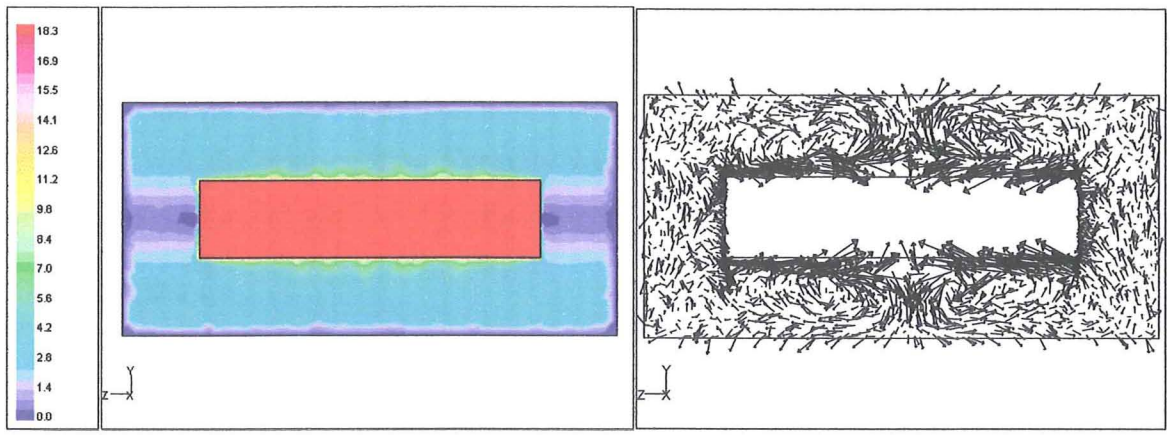

Figures 5.7 and 5.8. CFD output of velocity magnitude (m/s) and velocity vectors for rotating 3D roller in cylindrical cover at distance 214 mm from roller surface.

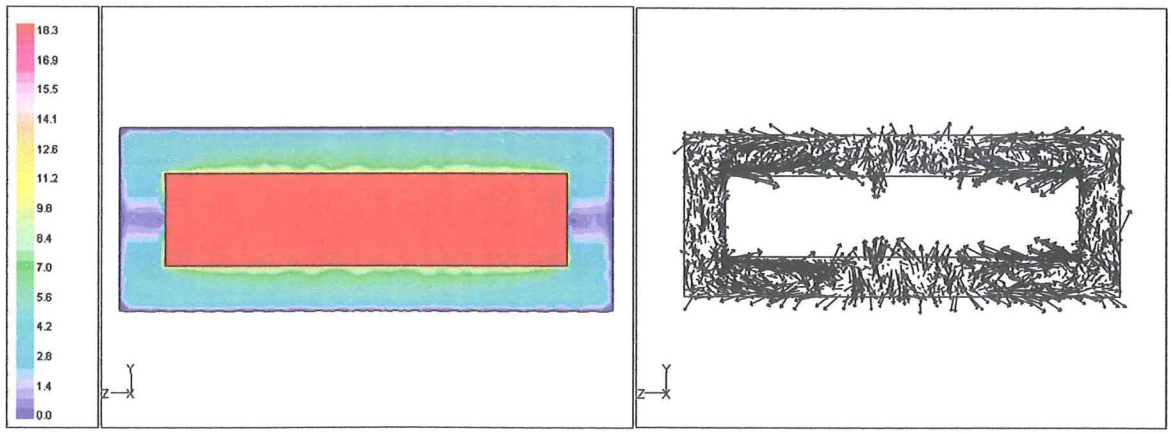

Figures 5.9 and 5.10. CFD output of velocity magnitude (m/s) and velocity vectors for rotating 3D roller in cylindrical cover at distance 107 mm from roller surface.

Carding machines do not usually operate with covers less than 100 mm away from the rotating surface, thus closer gaps were not investigated here. However as the gap reduces, it

is predicted that more toroidal vortices would appear along the roller (Wild, 1996), and the problem becomes similar to windage issues associated with rotor-stator interactions in motors and turbines that cause power losses. The use of a more refined grid may have improved the definition of the flow nears the centre of the roller in the 107 mm gap case and shown the formation of more vortices.

An interesting phenomenon to arise from the CFD output was the presence of wavy flows snaking along the rollers towards the centre (Figure 5.11). This was not immediately evident from the flow visualisation experiments, although the high rotational speeds would prevent a good view of any such flow. The grid resolution was not high enough to determine whether they were genuine Taylor vortices or an aberration associated with the coarse grid. However a graph of vorticity magnitude (Figure 5.12) shows some varying rotational component with the primary flow. Vorticity magnitude (ξ) is a measure of rotation of a fluid element, and is defined as the curl of the velocity vector,

$$\xi = \nabla \times \vec{v} \qquad (5.1)$$

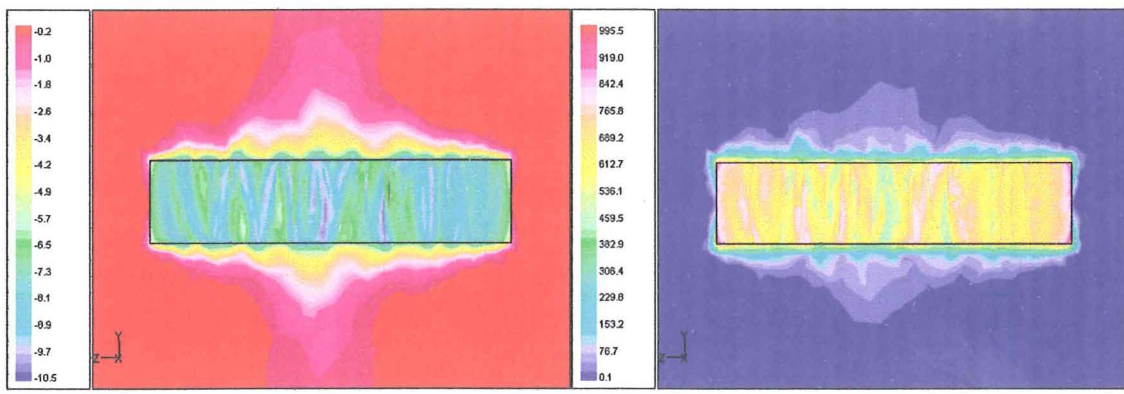

Figures 5.11 and 5.12. Evidence of toroidal vortices on 3D rotating cylinder in terms of tangential velocity (m/s) and vorticity magnitude (m/s).

5.5 Conclusions

The general flow patterns predicted on a 3D rotating cylinder by CFD were the following:

- a primary tangential flow, and the secondary effects of an axial flow to the centre of the roller
- a secondary axial flow towards the centre of the roller, converting to a radial flow away from the roller, as induced by a spinning disc.

The influence of covers was to suppress the radial flow outwards from the roller and induce vortex flow in the shape of elliptical toroids. There were additional smaller scale vortices snaking along the roller surface but it was unsure whether they were due to a genuine physical effect (Taylor vortices) or due to an inaccurate grid.

6 AIRFLOW BEHAVIOUR AROUND A PAIR OF ROTATING CYLINDERS

6.1 Introduction

The single roller airflow profile could be compared to results in the open literature. However there was no open literature describing airflow profiles around a pair of rotating rollers, with the closest approximation available to two rotating cylinders in 2D was that of a rotating vortex pair in potential flow (Kirchoff, 1985). However ascertaining the flow around two rollers was deemed very important in the understanding of airflows generated by carding machines and the general flow patterns and some air velocity measurements could be easily found by experiment using the test rig.

6.2 Setting up the CFD model

6.2.1 Grid generation and input conditions

The same underlying conditions used in the single rotating roller were also used for the roller pair. Exceptions included the change to the simpler k-ε model (the reasons being outlined in Section 6.4.2), and the SIMPLE algorithm replacing the PISO algorithm. Since the Type 1 roller was being used in experimental work, the porous depth was set at 2.5 mm and the porosity at c = 95/m. The basic grid for the roller set-up consisted of the following:

- An outer boundary at least one metre away from the rollers. This is much closer than the 10 metres used in the single roller. However it was necessary to reduce the number of nodes generated. The 'pressure-inlet' wall condition was used in Fluent to minimise boundary effects (Figure 6.1).
- A quad grid within the porous section, a tri grid elsewhere.
- Setting the closest interior grid point at around 0.3 mm away from the roller surface. This was achievable without an excessively fine grid away from the rotating surfaces by using the grid adaption facility in Fluent. The closest 4-8 layers of cells closest to the rotating surfaces were refined at least fourfold (see Figures 6.2 and 6.3).

There were typically 20 000 – 30 000 node points on a grid, depending on whether the rollers were smooth or rough, and on the gap between the rollers. The solutions were left for

10 000 iterations, with normalised pressure residuals of between 10^{-2} and 10^{-3}, and normalised velocity residuals between 10^{-4} and 10^{-5}. The iterations lasted typically 3-4 hours on a Pentium III 700 MHz computer.

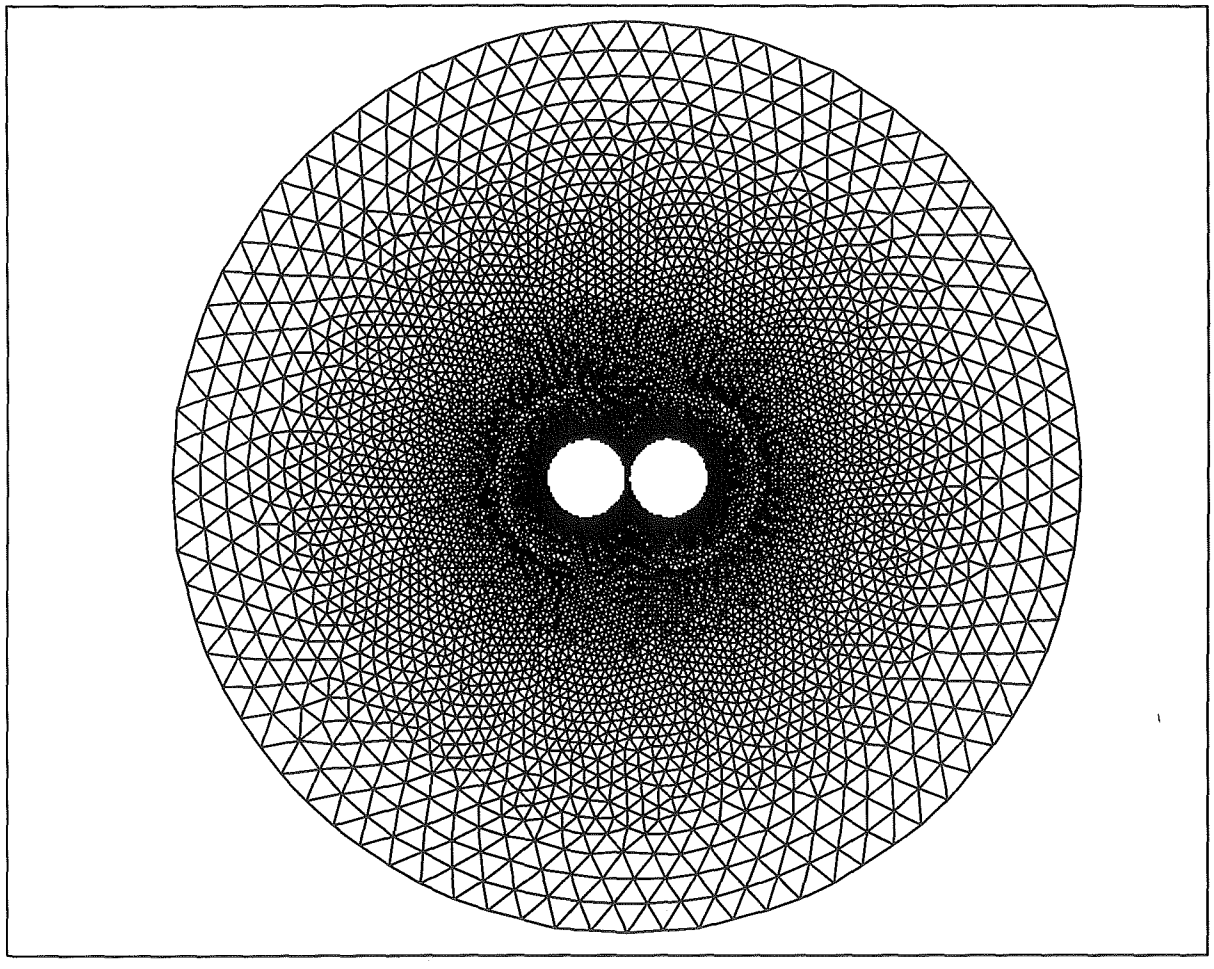

Figure 6.1 Typical CFD global grid for 2D roller pair.

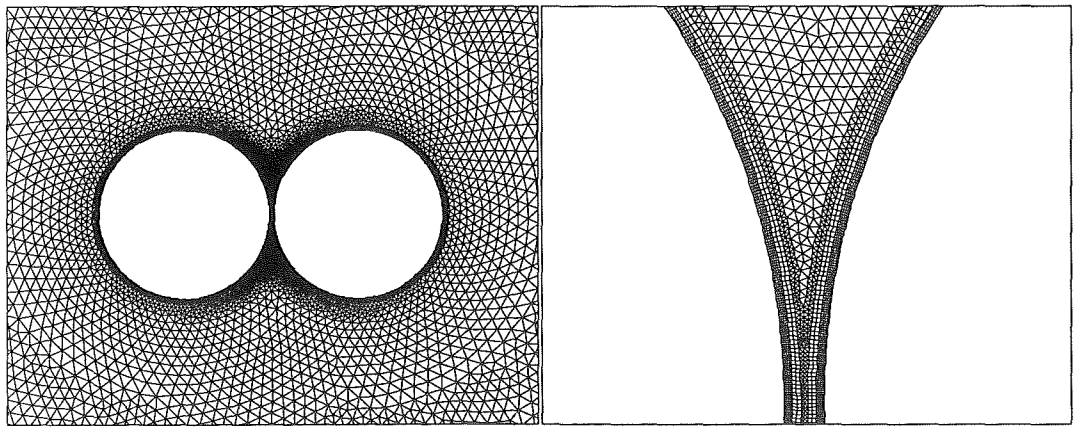

Figures 6.2 and 6.3. Magnifications of the CFD grid for the 2D roller pair.

6.2.2 Data input and analysis

The control used the 107 mm rollers and a 5 mm gap. The effects of the following variables were tested:

- Gap between rollers (smooth rollers only: 5, 50 mm). An example of small changes in gap not affecting the flow patterns is given in the co-rotating case, when a 1 mm and 5 mm gap between 'roughened' rollers are compared)
- Angular velocity of both rollers, ω (77, 175 rad/s)
- Comparison between rough and smooth rollers (porous media inertial resistance, c = 95/m)
- The effects of a small gap change between rough rotating rollers (from 0.5 mm to 1 mm)
- Angular velocity difference between rollers (ratios of 2:1, 4:1, 8:1 and one roller stationary for both co- and counter-rotating cases)

The small gap change work simulation was conducted because it was hoped that a 1 mm gap could be tolerated for the subsequent 2D carding machine component work in CFD. If smaller tolerances commonly used for real carding machines (often down to 0.2 mm and actually touching in the case of the swift and fancy rollers) were used, it would cause serious grid density problems and necessitate the creation of massively dense grids to avoid excessive aspect ratios for grid faces.

6.3 Experimental method

6.3.1 Flow visualisation

Flow visualisation work using smoke generation was conducted on a pair of Type 1 rollers, using a maximum speed of 175 rad/s (18 m/s surface speed). The method for collecting information was the same as for the 3D single roller, and detailed in Section 5.2. The smoke was introduced underneath the gap between the rollers.

The following set of experiments were conducted and labelled accordingly on the mpeg file. Velocities, where indicated, are at the roller surface.

1. Counter-rotating rollers, left hand side (LHS) 18 m/s = right hand side (RHS)
2. Counter-rotating rollers, LHS 8 m/s = RHS

3. Counter-rotating rollers, LHS 8 m/s, RHS 4 m/s
4. Counter-rotating rollers, LHS 8 m/s, RHS stationary
9. Co-rotating rollers, LHS 18 m/s = RHS
10. Co-rotating rollers, LHS 8 m/s = RHS
11. Co-rotating rollers, LHS 8 m/s, RHS 4 m/s

Frames were captured from the 8 m/s surface speed experiments and analysed in this work since the airflow trends were much easier to visualise than with surface speeds at 18 m/s.

6.3.2 Hot wire anemometry

A method to determine whether the CFD output for a pair of rotating rollers was accurate was to graph the air velocity as a function of radial distance from the roller surface. So long as the initial starting point was away from the closest gap between the rollers, the profile should approximate that of a single roller close to the surface. This is particularly true of when there was a considerable gap between the rollers, since the rollers could be considered as single rollers in isolation. With this in mind, a set of hot wire anemometry experiments were conducted on the roller pair.

The same hot wire anemometry set-up was used as for the single rotating roller experiments (Section 4.2). The pair were both Type 1 rollers. Readings were taken for both co-rotating and counter-rotating rollers, each rotating at 8 m/s. The probe was positioned directly above the centre of one of the rollers, and above its axis of rotation. Readings were taken of air velocity as a function of radial distance away from the roller surface.

6.4 Results and discussion

6.4.1 CFD predictions for smooth rotating rollers

Figures 6.4 to 6.9 show the comparisons between co- and counter-rotating rollers for the base case (107 mm diameter smooth rollers, 5 mm gap, 175 rad/s) in terms of velocity contours, velocity vectors and stream functions respectively.

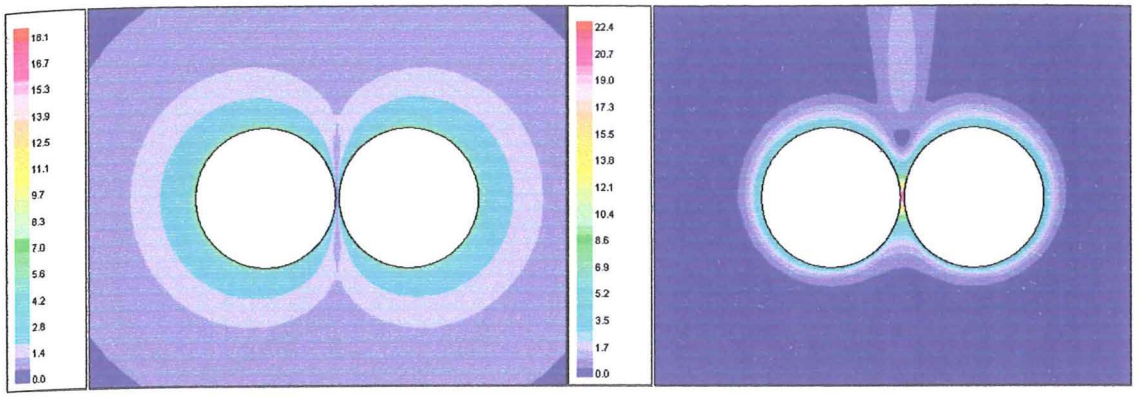

Figures 6.4 and 6.5. CFD output of velocity magnitude (in m/s) for smooth co-rotating and counter-rotating rollers respectively with a 5 mm gap.

The boundary layer is considerably deeper in the case of co-rotating rollers compared to counter-rotating rollers. The co-rotating rollers' boundary layers complement each other, and combine to create a single boundary layer similar in magnitude to a single rotating roller. Like the single rotating roller, the co-rotating rollers have had no restrictions in generating a fully developed boundary layer. The converse is true for the counter-rotating rollers; the boundary layers they generate tend to cancel each other out after each revolution of the rollers.

The CFD output predicted the mean air velocity at the roller gap to approach zero for co-rotating rollers. This was also predicted in potential flow theory, but Fluent predicted the turbulent kinetic energy to be very high at this point. Although the counter-rotating rollers produced a smaller boundary layer, the synergistic effects of the rollers rotating in the same direction past the gap produced an air velocity greater than that of each roller's tip speed.

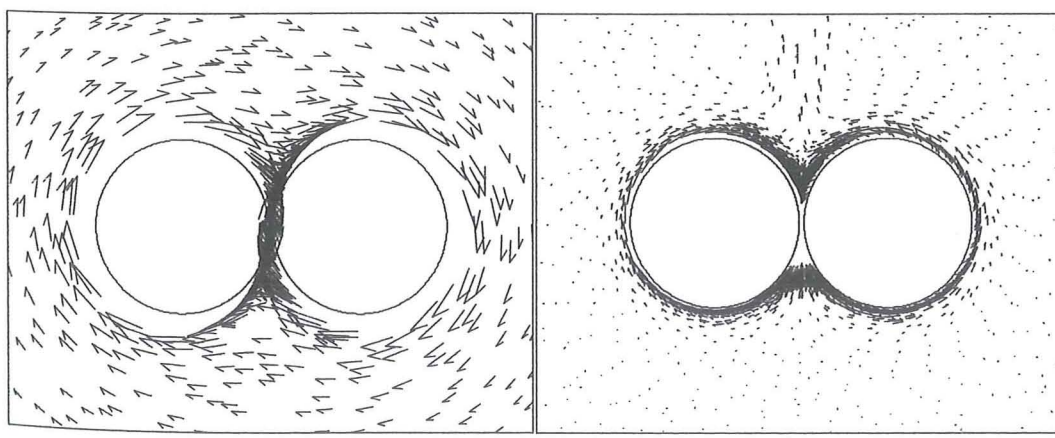

Figures 6.6 and 6.7. CFD output of velocity vectors for smooth co-rotating and counter-rotating rollers respectively with a 5 mm gap.

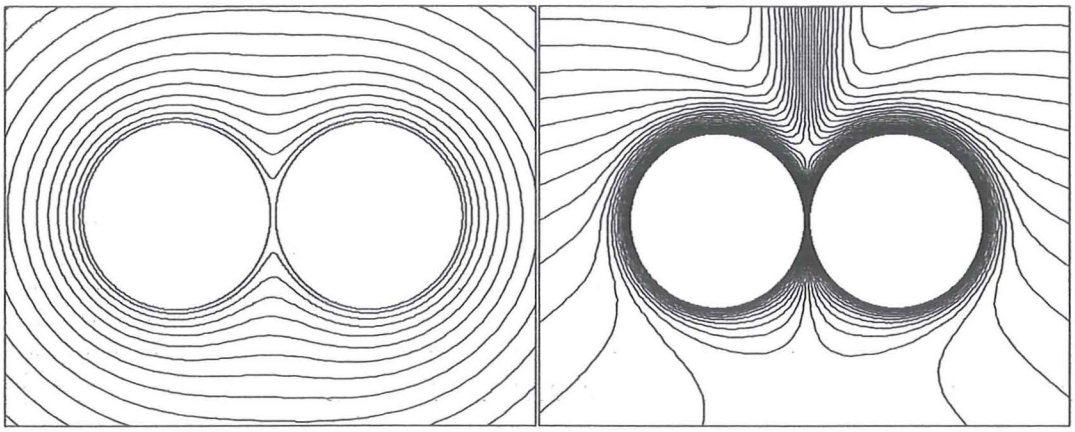

Figures 6.8 and 6.9. CFD output of stream functions for smooth co-rotating and counter-rotating rollers respectively with a 5 mm gap.

Figures 6.10 to 6.13 show the comparisons between co-rotating and counter-rotating rollers for the case of a 50 mm gap.

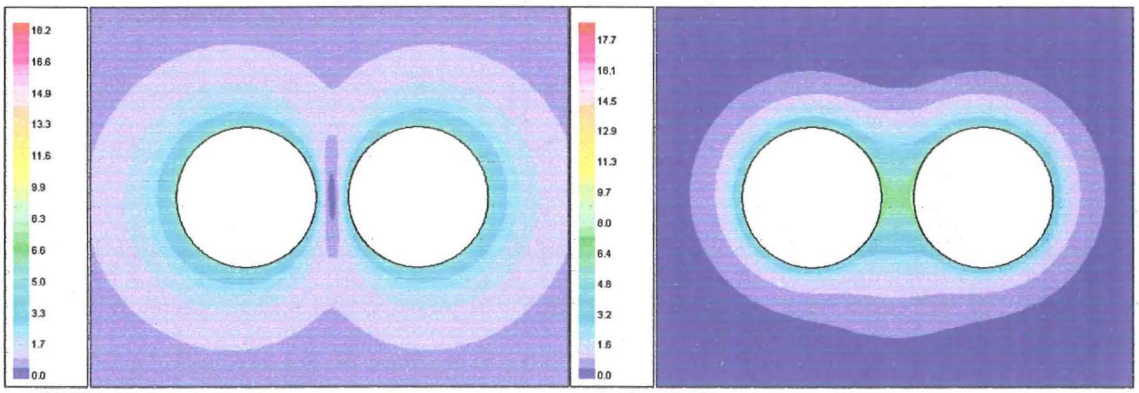

Figures 6.10 and 6.11. CFD output of velocity magnitude (in m/s) for smooth co-rotating and counter-rotating rollers respectively with a 50 mm gap.

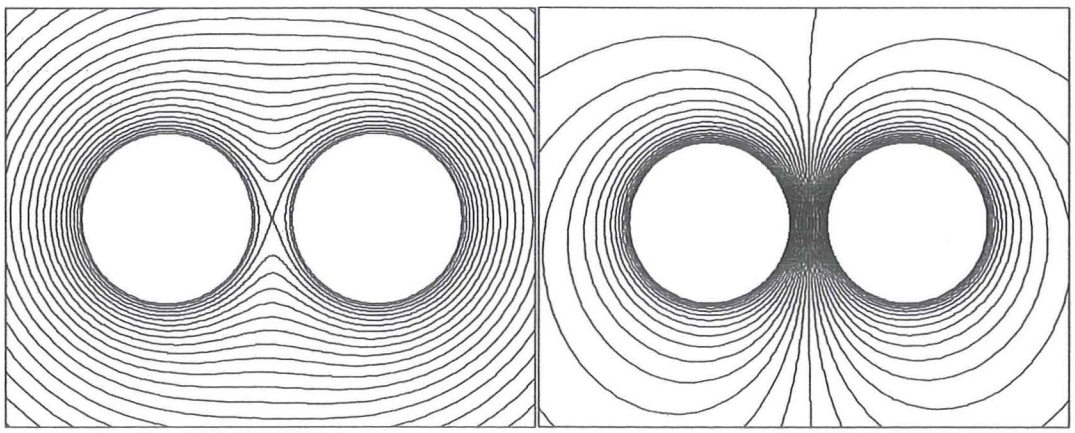

Figures 6.12 and 6.13. CFD output of stream functions for smooth co-rotating and counter-rotating rollers respectively with a 50 mm gap.

While the airflow profile of the co-rotating rollers looks very similar to the potential vortex flow patterns, the same cannot be said for counter-rotating rollers. As the rollers are moved closer together (compare Figures 6.5 and 6.11), less air can be pushed through the gap and the pressure upstream of the gap increases. This leads to the formation of a plume of air heading away from the roller, which can be noticed a considerable distance away (Figure 6.14). There is also a flow separation point above the rollers (the saddle point in Figure 6.6).

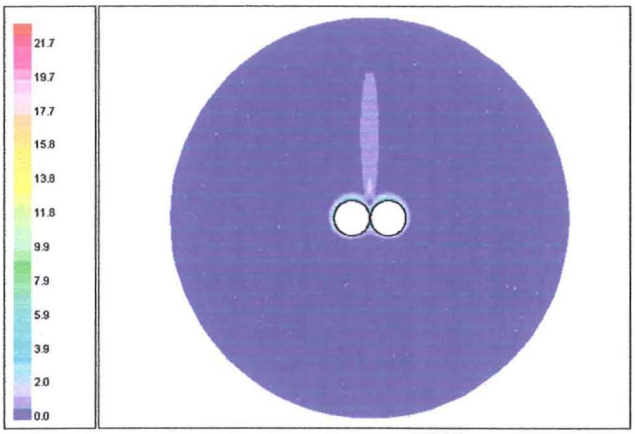

Figure 6.14. CFD output of velocity magnitude (in m/s) for smooth counter-rotating roller with a 5 mm gap zooming out from the rollers and showing the plume.

A plot of angular velocity defect as a function of distance from the rollers is shown in Figure 6.16, along with a smooth single rotating roller as a comparison. For the roller pairs, the airflow profile was taken along a line above the RHS roller (refer to Figure 6.15). The data from the RHS was nearly identical with that above the LHS roller. The profiles were also very similar within 1 mm of the surface below the rollers and to the side of both rollers.

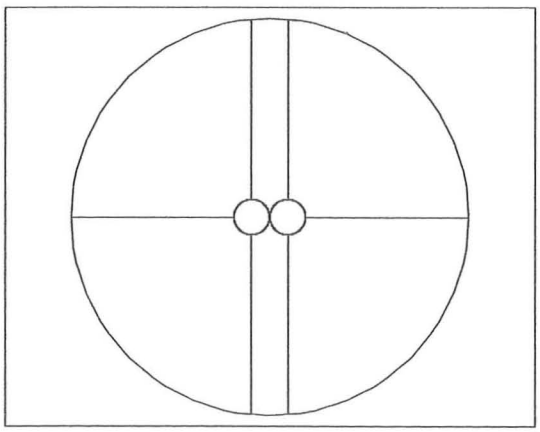

Figure 6.15. The CFD domain of the rotating roller pair, with lines showing where velocity profiles were taken.

The CFD simulations also predict close comparisons of airflow profiles between a single rotating roller and rotating roller pair, particularly for the pair of rollers with the 50 mm gap since there are fewer interaction effects (Figure 6.16). However the counter-rotating rollers air velocity diminishes rapidly as a function of distance from the rollers, explained by the boundary layers counteracting each outer.

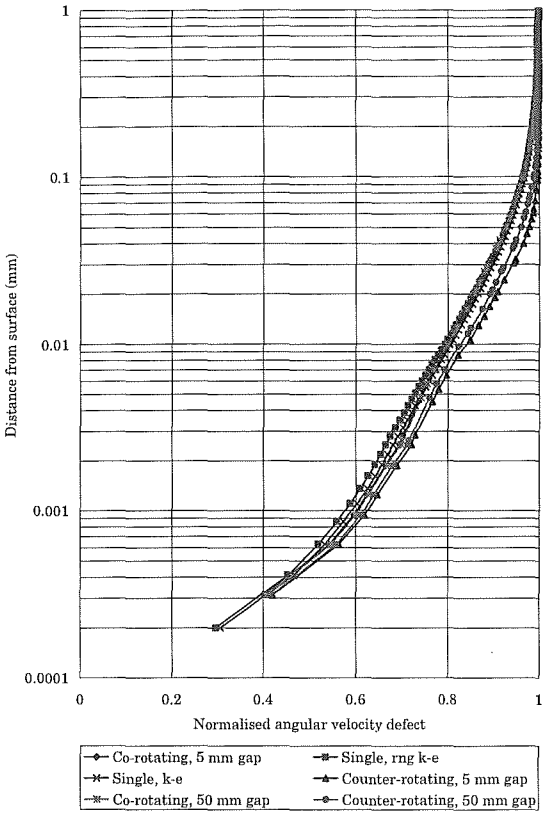

Figure 6.16. Airflow profile comparison between single rollers and roller pairs.

6.4.2 CFD predictions for rough rotating rollers

Figures 6.17 to 6.20 show the comparison between co-rotating and counter-rotating rollers with a small gap (0.5 and 1 mm respectively). Note that the grid for the 0.5 mm gap contained about 40 000 nodes, more than twice that for the 1 mm gap.

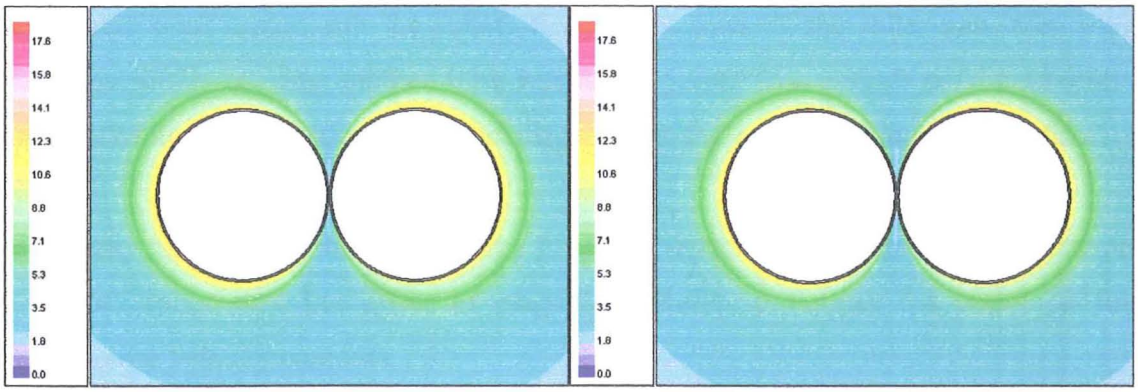

Figures 6.17 and 6.18. CFD output of velocity magnitude (in m/s) for smooth co-rotating rollers with a 0.5 mm and 1 mm gap respectively.

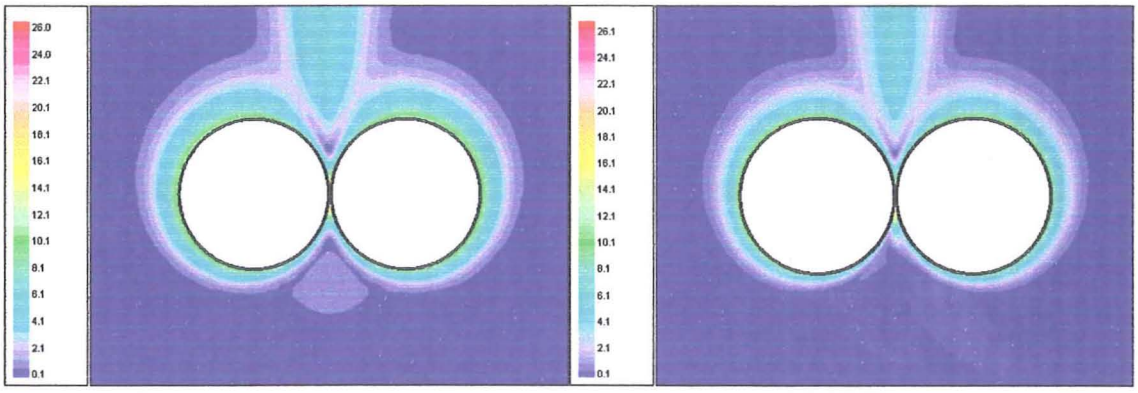

Figures 6.19 and 6.20. CFD output of velocity magnitude (in m/s) for smooth counter-rotating rollers with a 0.5 mm and 1 mm gap respectively.

The comparison is good for the co-rotating rollers. However in the case of the counter-rotating flow, the unstable jet attaches to one of the rollers and moves the plume very slightly off-centre. The streamlines may slightly alter, but the velocity magnitudes are very similar in each case. Thus a 1 mm gap is considered a satisfactory simplification to make, and makes for much less computational expense.

It was discovered at this point that the k-ε model was better suited to the unstable flow generated by the counter-rotating rollers (see Section 6.4.3) and was used in all subsequent CFD work. It gave similar answers to the RNG k-ε model for the case of the smooth rollers (refer to Figure 6.16), so its use would introduce few significant errors.

Figures 6.21 and 6.22 show the velocity vectors and stream functions respectively for a pair of rough counter-rotating rollers. The magnitude of the plume increases and there exists a

considerable draft underneath the rollers that moves towards the roller gap, then moves around the rollers causing another flow separation point. This updraft combined with an intense jet of downward moving air squeezing through the gap causes the unstable flow.

The velocity and stream function patterns for the co-rotating pair were almost identical to the smooth roller case but differ in magnitude. Refer to Figures 6.4 and 6.18 for a comparison of velocity contours.

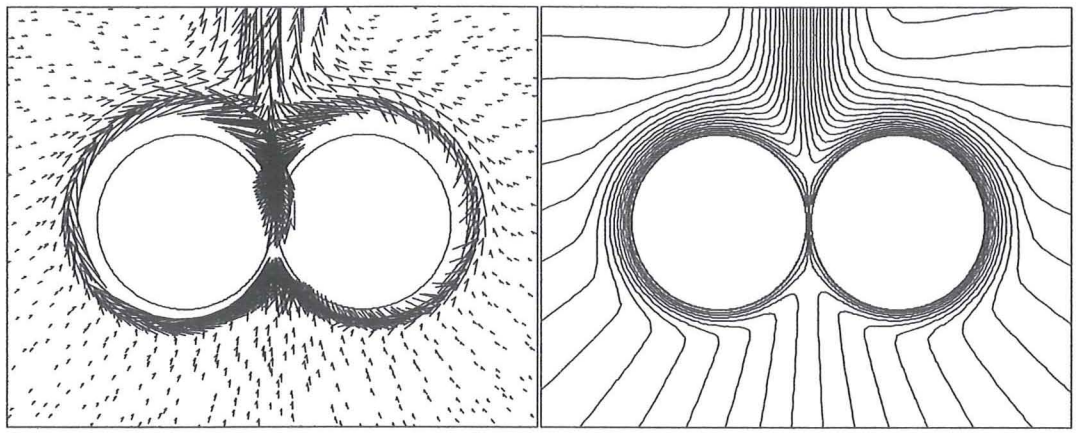

Figures 6.21 and 6.22. CFD output of velocity vectors and stream functions for a rough counter-rotating roller pair with a 1 mm gap.

6.4.3 Experimental results and comparison with CFD predictions

Figures 6.23 to 6.33 illustrate the comparison between the flow visualisation results for Type 1 rollers and accompanying CFD simulations. In the photos, the rollers are partly obscured by the side walls.

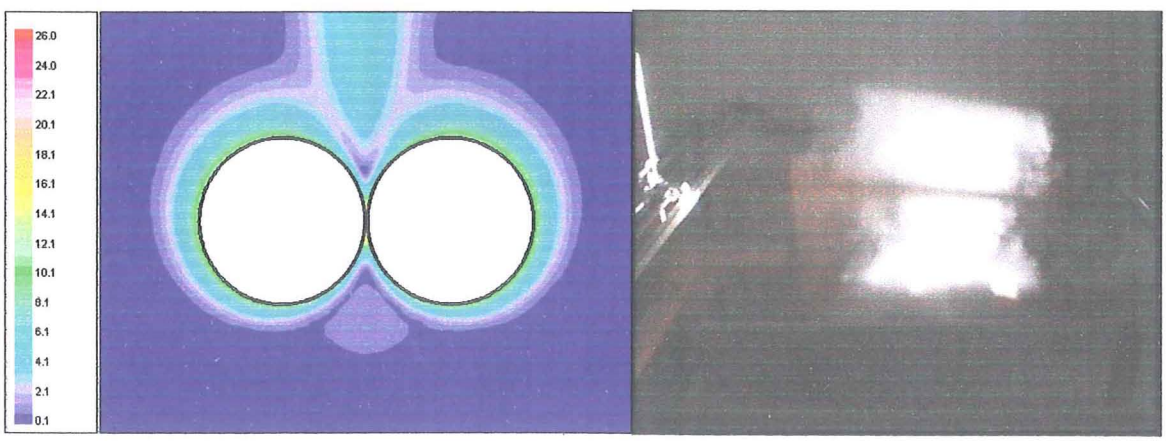

Figures 6.23 and 6.24. Counter-rotating, tip speeds of both rollers 8 m/s, LHS clockwise, RHS anticlockwise.

Note here that the CFD output is for a pair of rollers with a 1 mm gap, with the prediction that the plume will move directly away from the rollers.

Figure 6.25 gives the CFD output for a pair of 'roughened' counter-rotating rollers with a 5 mm gap. The plume is off centre because the high velocity air ejecting below the rollers has re-attached to one of the rollers rather than moving directly downwards. The high volume, high velocity jet creates an area of low pressure and becomes unstable as it rapidly expands downstream of what can be best termed a throttle. The low pressure (and the high speed plume upstream) causes a suction effect of air below the rollers to move upwards towards the rollers. This opposing effect and the availability of a high speed, low pressure stream, namely the developing boundary layer on either roller causes the jet to attach to either roller. It is suspected that the jet may rapidly alternate attaching between each roller, causing the plume upstream to be highly turbulent and of greater width than predicted by Fluent. This certainly seemed to be the case in the experimental work, where although the plume went in the right direction, it was highly turbulent and was much broader than the CFD prediction.

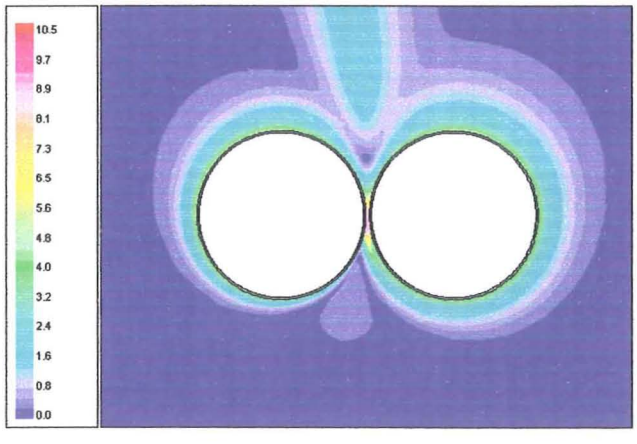

Figure 6.25. CFD output of velocity magnitude (m/s) for a rough counter-rotating roller pair with a 5 mm gap.

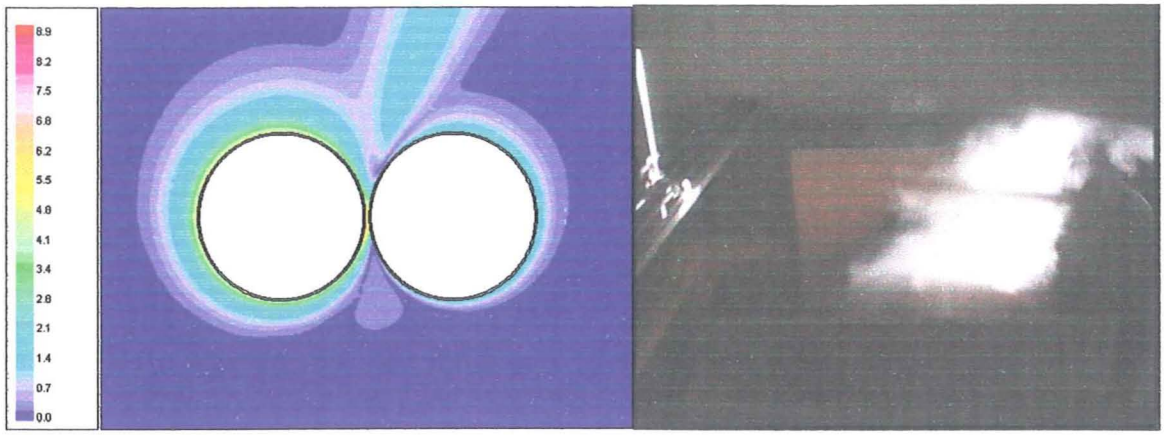

Figures 6.26 and 6.27. Counter-rotating, tip speeds LHS 8 m/s clockwise, RHS 4 m/s anticlockwise.

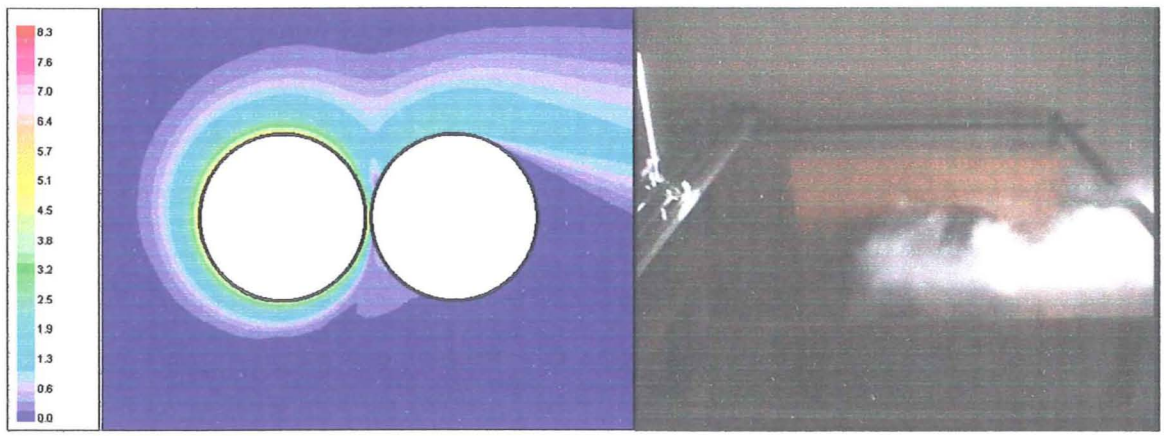

Figures 6.28 and 6.29. Tip speeds LHS 8 m/s clockwise, RHS stationary.

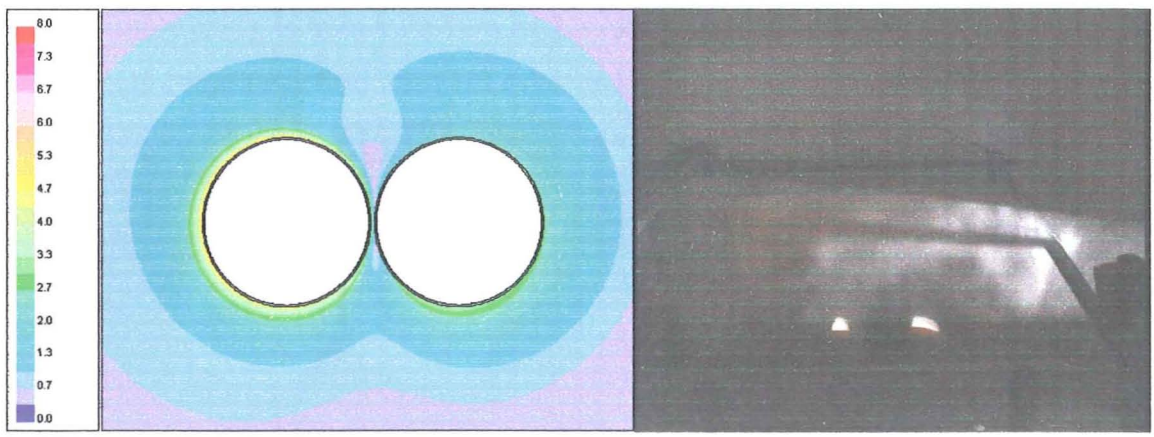

Figures 6.30 and 6.31. Co-rotating, tip speeds LHS 8 m/s anticlockwise, RHS 4 m/s anticlockwise.

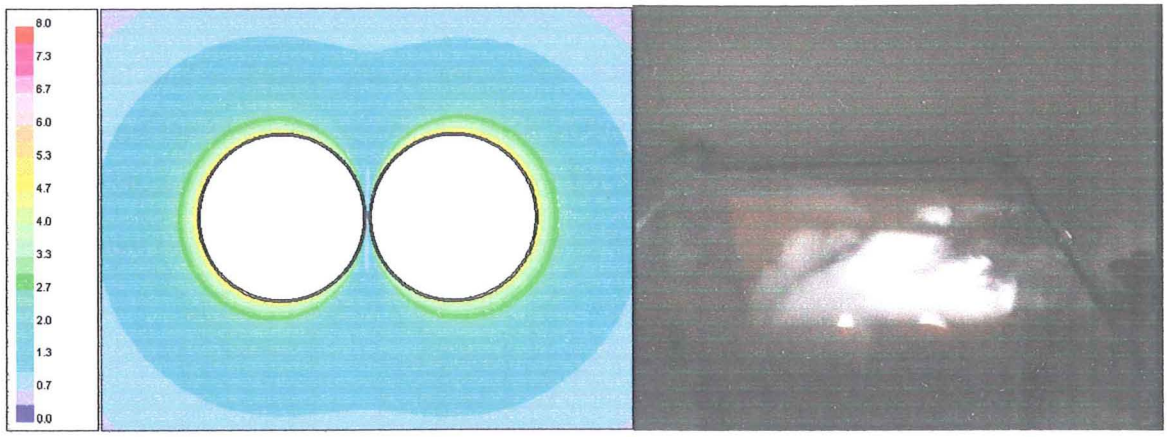

Figures 6.32 and 6.33. Co-rotating, tip speeds of both rollers 8 m/s, anticlockwise.

The CFD predictions of plume direction were close to those achieved from the experiments, except they were wider and more turbulent than predicted. In counter-rotating flow, as the RHS roller becomes progressively slower, the plume moves towards the RHS. When the RHS roller is stationary, the developed boundary layer of moving air hits the roller, bounces off and then creeps along the roller. This creeping effect increases if the RHS roller rotates in the same direction as the LHS roller (Figures 6.34 and 6.35). The effect is more pronounced if the roller has rougher surfaces. If the slower roller on the RHS is co-rotating at a critical speed, the plume re-attaches to the LHS roller. For the case of the experimental rollers, the critical speed of the RHS roller was predicted to be between 1/8 and 1/4 that of the LHS roller and rotating in the same direction. The flow visualisation results with the RHS roller co-rotating at half the speed of the LHS roller generally backed this result up (refer to Figure 6.31). However the flow in this experiment was quite unstable, and often the plume would come away from the LHS roller and move upwards (refer to the disc).

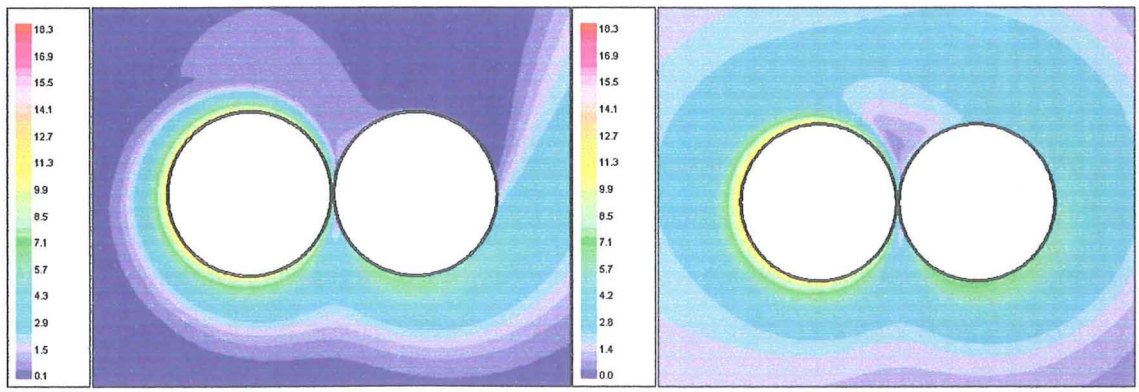

Figures 6.34 and 6.35. CFD output of velocity magnitude (m/s) for rough counter-rotating rollers with a 5 mm gap, the RHS roller rotating at 1/8 and 1/4 speed respectively of the LHS roller.

As previously mentioned, the unstable flow underneath the rollers contributes towards a more broad and turbulent plume above the rollers. This was also borne out in the air velocity profiles obtained above the RHS roller. The experimentally obtained velocities were well above predictions more than about 33mm away from the wire tips. In contrast, the experimental velocity data for the co-rotating roller closely matched the CFD output (Figure 6.36).

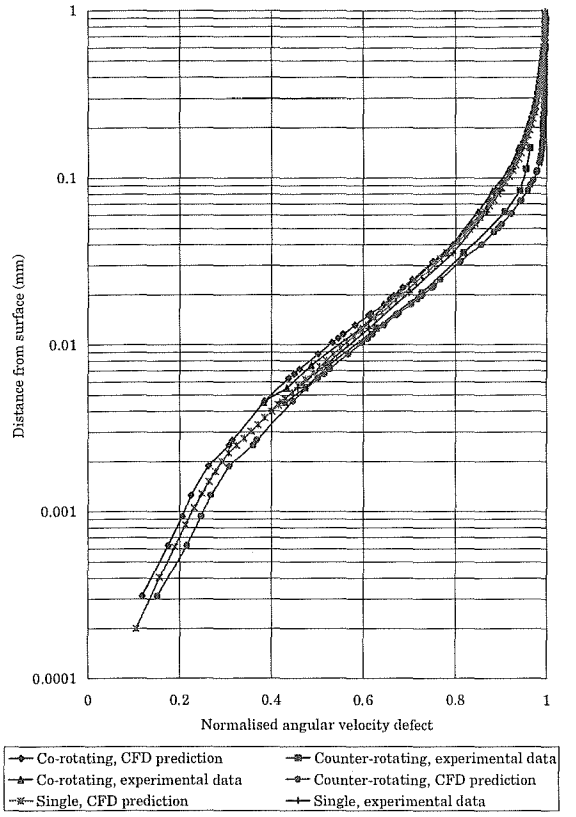

Figure 6.36. Comparisons between experimental and CFD predicted airflow profiles for co-rotating and counter-rotating roller pairs.

6.5 Conclusions

Co-rotating and counter-rotating rollers have considerably different flow patterns to each other and to a single rotating roller. The co-rotating roller pair generates a boundary layer similar in magnitude to a single rotating roller. The flow pattern of the co-rotating roller pair also closely matched that predicted by co-rotating vortices from potential flow theory.

The counter-rotating rollers produce a smaller boundary layer, and if the gap is close enough, a plume of air is produced extending in the opposite direction of the rollers

approaching the gap. This behaviour is different to counter-rotating vortices where a plume of air is not produced.

The introduction of rough surfaces to a counter-rotating roller pair introduces instabilities downwind of the gap that CFD could not accurately predict. These instabilities may lead to increasing air turbulence around the rotating roller pair. This was noticed in the flow visualisation work where although the plume position was predicted accurately by CFD, its width and magnitude were underestimated.

7 AIRFLOW BEHAVIOUR AROUND TWO DIMENSIONAL CARDING MACHINE COMPONENTS

7.1 Introduction

With CFD predictions matching experimental output and literature in Sections 3 to 6, we can proceed with some confidence in using CFD to predict airflow generated by more complex geometries. The airflow trends from the CFD modelling will be compared to the open literature and to flow visualisation experiments conducted on a small scale simplified carding machine. The experimental results are presented first, in Section 7.4. The results from CFD simulations of various 2D carding machine components based on a Chadwick carding machine (Figure 7.1) follow in Section 7.5. Discussion, including comparisons with experimental observations and the literature, are also included in Section 7.5.

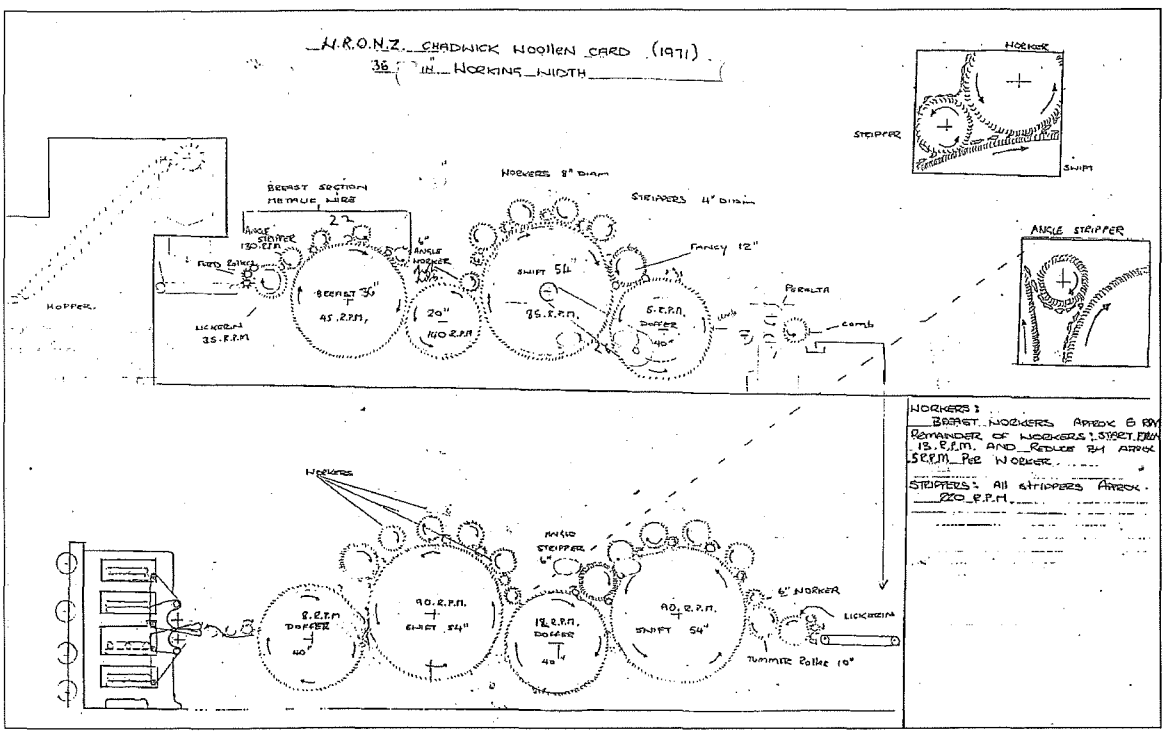

Figure 7.1. Chadwick wool carding machine at WRONZ (WRONZ, 1997).

7.2 Experimental method

This carding machine had the basic lickerin/swift rollers as shown in Figure 1.1 and had two pairs of workers and strippers. It did not have the more complicated breast section used in full scale carding machines. The simplified machine had a removable cover over the

worker/stripper roller section of the swift roller. A flow visualisation experiment was conducted using smoke, with all sections uncovered. A 'dry' run was conducted, i.e. the airflows were not affected by the presence of fibres. It was difficult to accurately show airflow trends with photographs due to the high levels of turbulence, especially with the cover down. As such, the general trends were hand sketched.

7.3 Setting up the CFD model

Various components of the carding machine were chosen to be modelled based on the literature review and discussion with WRONZ scientists. The following components were modelled:

- Swift/worker/stripper roller
- Swift/fancy/doffer roller
- Breast/transfer/swift/worker roller
- Swift/doffer/angle stripper
- Mote knife/swift roller

Roller sizes, positions, speeds, and direction of rotation were all based on the Chadwick wool carding machine located at WRONZ. These details are given for each component in Sections 7.3.1 to 7.3.5. Although this machine had a pilot plant production rate (about 25 kg wool/hour) it has all the components of an industrial sized machine. A 1 mm gap and 2.5 mm been chosen as standard between all rollers. Although the actual gaps are usually less than this, using smaller gaps in CFD would cause serious grid density issues, especially for predictions involving the large swift roller in its entirety. Introduction of slightly larger gaps should cause few errors, as detailed in Section 6.4.2. Roller 1 type carding wire has been assumed to be standard except for the fancy wire. In reality, some rollers are clothed with wires of slightly differing depths and different types, but the general direction of airflow pattern should still hold. The other input conditions such as near-wall models, turbulence models and underrelaxation factors were the same as for the roller pair simulations. The grids generated in Gambit were refined in Fluent to plant node points within the laminar sublayer, similar to the grid refinement process for the CFD simulations of the rotating roller pair. Some close-up details of each grid are included in the Appendix.

7.3.1 Swift/worker/stripper roller interactions

7.3.1.1 Worker/stripper rollers in isolation

Only one set of worker/stripper rollers on the swift is included in this simulation. An example of a swift/stripper/worker in isolation is the first worker/stripper pair after the lickerin roller (or tummer roller for the Chadwick card). Roller specifics are detailed in Table 7.1 and illustrated in Figure 7.2.

Table 7.1. Roller information used in Fluent.

Roller type	Swift	Worker	Stripper
Effective wire depth (mm)	2.5	2.5	2.5
Diameter (mm)	1 372	214	107
Direction of rotation	clockwise	anticlockwise	anticlockwise
Wire orientation	upwind	downwind	upwind
Inverse porosity (1/m)	95	45	95
Angular velocity (rad/s)	-8.90	1.36	23.04
Tip speed (m/s)	6.11	0.11	1.23

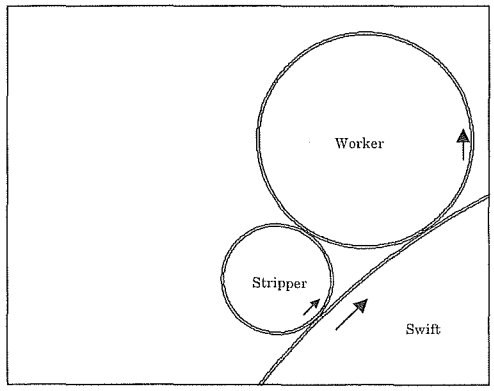

Figure 7.2. Positions of swift/worker/stripper rollers relative to each other.

7.3.1.2 Worker/stripper rollers in series

In this model, rotational effects have been assumed negligible, and the spacing between each worker/stripper set at 325 mm, approximately the same as for the Chadwick carding machine. A grid for one worker/stripper was constructed in Gambit, then the translational periodic function used in Fluent to simulate an infinite number of worker/stripper pairs in series. The roller specifics are detailed in Table 7.2 and illustrated in Figure 7.3.

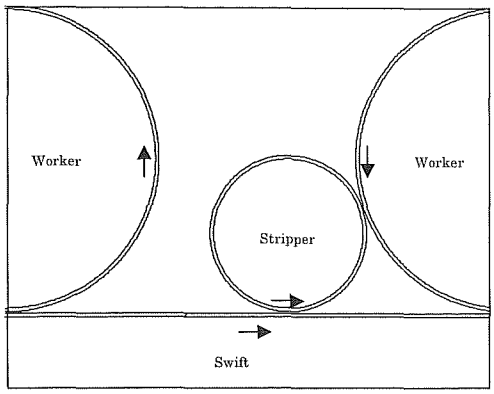

Figure 7.3. Position of swift/worker/stripper rollers relative to each other in series.

7.3.2 Swift/fancy/doffer roller interactions

In this model, there are no worker/stripper rollers affecting the airflow, nor any 'fly' strippers often used adjacent to fancy rollers. Roller specifics are detailed in Table 7.3 and illustrated in Figure 7.4.

Table 7.3. Roller information used in Fluent.

Roller type	Fancy	Swift	Doffer
Effective wire depth (mm)	25	2.5	2.5
Diameter (mm)	321	1 372	508
Direction of rotation	Anticlockwise	clockwise	Anticlockwise
Wire orientation	Upwind	upwind	Downwind
Inverse porosity (1/m)	15	95	45
Angular velocity (rad/s)	46.73	-8.90	0.52
Tip speed (m/s)	7.50	6.11	0.27

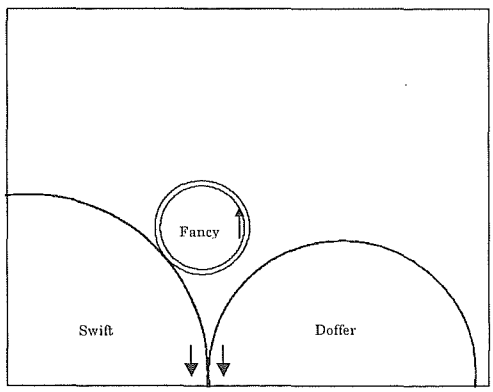

Figure 7.4. Positions of swift/fancy/doffer rollers relative to each other.

7.3.3 Breast/transfer/swift/worker roller interactions

It is assumed there is no influence of a floor in this model, and that the breast and swift rollers are rotating in isolation and have no other rollers attached to them. Roller specifics are detailed in Table 7.4 and illustrated in Figure 7.5.

Table 7.4. Roller information used in Fluent.

Roller type	Breast	Transfer	Swift	Worker
Effective wire depth (mm)	2.5	2.5	2.5	2.5
Diameter (mm)	914	508	1 372	160.5
Direction of rotation	clockwise	Anticlockwise	clockwise	anticlockwise
Wire orientation	upwind	upwind	upwind	downwind
Inverse porosity (1/m)	95	95	95	45
Angular velocity (rad/s)	-4.71	14.66	-8.90	0.63
Tip speed (m/s)	2.16	3.72	6.11	0.05

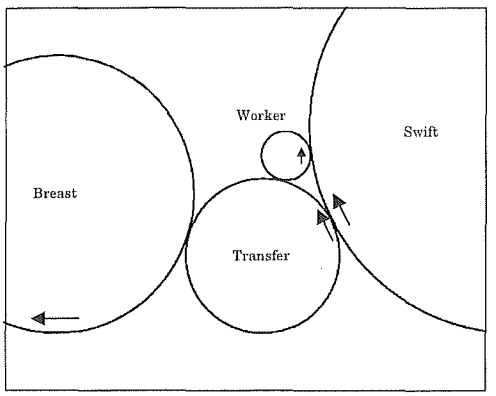

Figure 7.5. Positions of breast/transfer/swift/worker rollers relative to each other.

7.3.4 Swift/doffer/angle stripper interactions

As for the CFD model in Section 7.3.3, there was no floor influencing the airflow and the swift and doffer rollers have no other rollers attached to them. Roller specifics are detailed in Table 7.5 and illustrated in Figure 7.6.

Table 7.5. Roller information used in Fluent.

Roller type	Swift	Doffer	Stripper
Effective wire depth (mm)	2.5	2.5	2.5
Diameter (mm)	1 372	1 016	160.5
Direction of rotation	Anticlockwise	clockwise	clockwise
Wire orientation	Upwind	downwind	downwind
Inverse porosity (1/m)	95	45	95
Angular velocity (rad/s)	8.90	-1.26	-13.61
Tip speed (m/s)	6.11	0.64	1.09

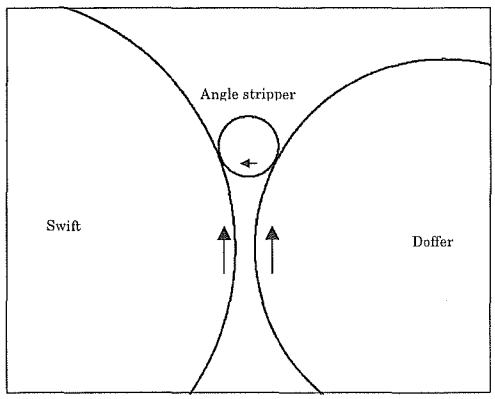

Figure 7.6. Positions of swift/doffer/angle stripper rollers relative to each other.

7.3.5 Mote knife/swift roller interactions

The swift roller conditions are as for all preceding cases. The mote knife was 300 mm long, 20 mm wide, possessed a blade at 45° to normal, and angled flat against the swift roller. There was a 1 mm gap between the mote knife and the outer porous surface of the roller. Figure 7.7 illustrates the example.

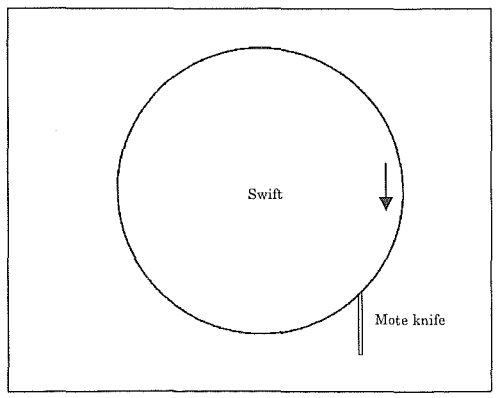

Figure 7.7. Position of swift roller and mote knife relative to each other.

7.4 Experimental results

Figures 7.8 shows the general 2D airflow trends over the simplified card with no breast section. The most noticeable primary airflows were tangential and associated with the swift and fancy rollers. There was only a very thin boundary layer associated with airflow over the swift roller, particularly near the worker/stripper pairs. The fancy roller that generated an air current stretching back over the worker/stripper roller sets caused the dominant secondary airflow. A secondary 2D airflow was noticed by the first worker/stripper pair, with air moving away from the rollers towards the feed section of the carding machine.

It was difficult to pick up the 3D edge effects due to the turbulence and the presence of a wall and floor close by. Any 3D effects were not as strong as for the isolated 3D roller, in particular the absence of a strong radial flow outwards from the centre of the rollers. The floor may be acting as a pseudo bottom cover to suppress the spinning disc effect. The presence of the other rollers around the swift roller could also be reducing the radial outflow.

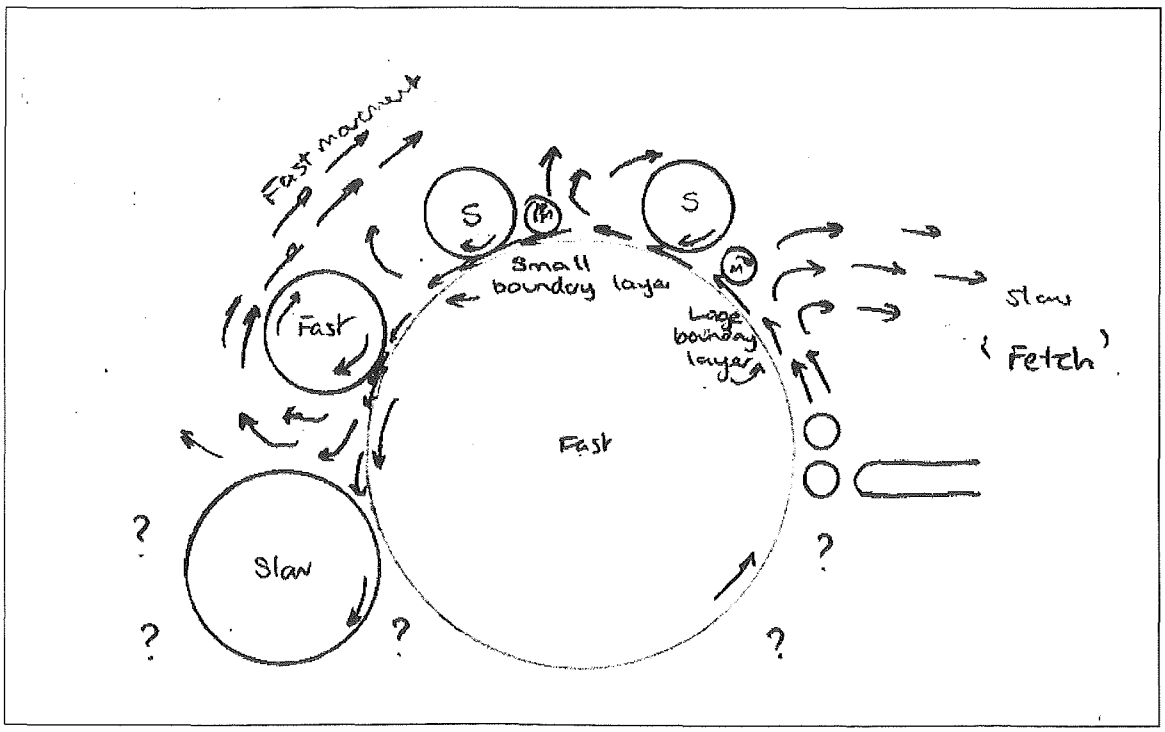

Figures 7.8. Primary and secondary airflow profiles observed over simplified carding machine.

7.5 CFD simulation results

7.5.1 Swift/worker/stripper roller interactions

7.5.1.1 Worker/stripper rollers in isolation

Figures 7.9 to 7.11 illustrate the velocity vectors, velocity magnitude and stream functions respectively for this CFD example. The bouncing of the airflow off the stripper and away from the card is a known airflow issue in carding, and is often called the 'fetch'. This area is commonly unguarded in carding machines.

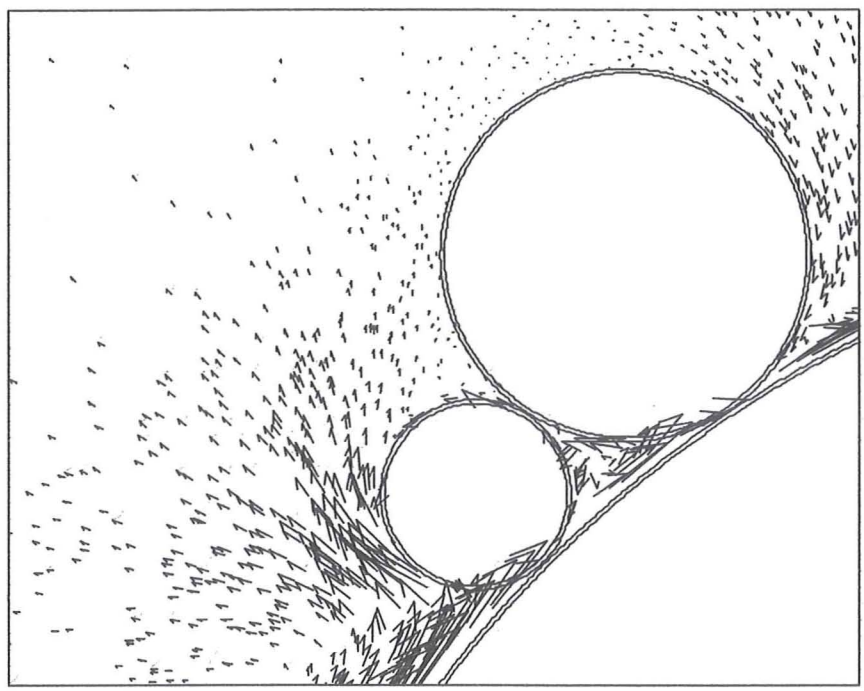

Figure 7.9. CFD output of velocity vectors for the worker/stripper pair in isolation.

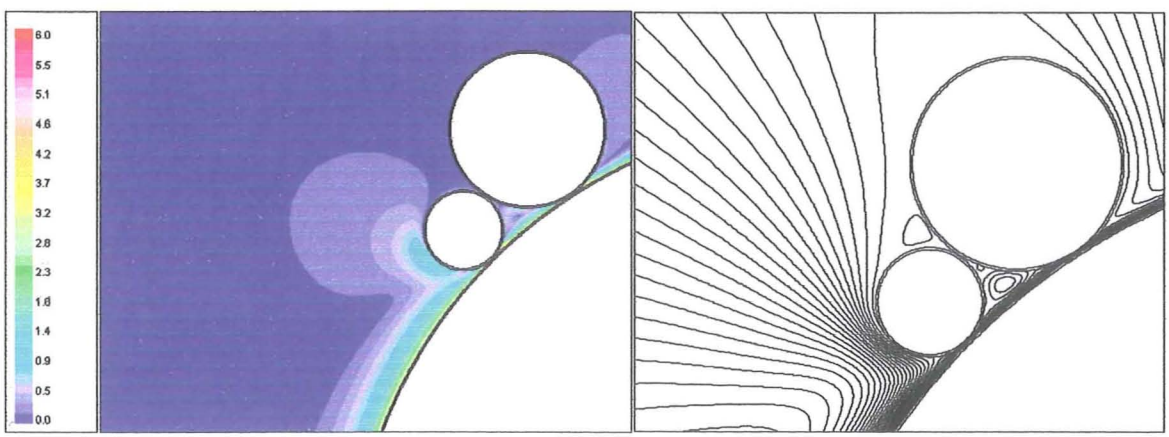

Figures 7.10 and 7.11. CFD output of velocity magnitude (m/s) and stream functions for the worker/stripper pair in isolation.

7.5.1.2 Worker/stripper rollers in series

Figures 7.12 to 7.14 illustrate the velocity vectors, velocity magnitude and stream functions respectively for this CFD example. It was important to know about this section of the swift since it is where most of the primary functions of the carding machine are occurring. The other sections only aid this section by properly feeding the wool to this section or transporting wool off this section.

The roller pairs suppress the boundary layer development over the swift, with negligible airflow over the worker rollers. This is consistent with the comment in WIRA (1969) that airflows generated by the swift roller are only important to less than 1 mm from the swift wire tips. However it is only applicable to the top of the swift. The stream functions show primary and secondary vortices occurring between the worker/stripper pairs. The influence of covering the worker/swift section of the swift roller was considered to be useful work but the evidence from this section is that a cover would have virtually no impact on airflows. The only benefit (apart from a safety point of view) would be to minimise the impact of other airflow impinging on this area of the swift roller.

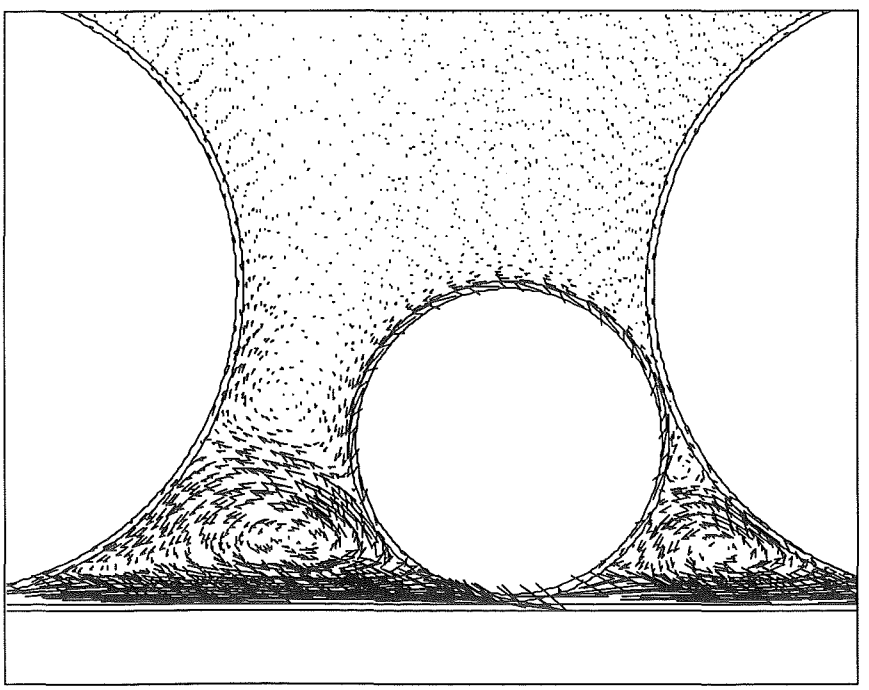

Figure 7.12. CFD output of velocity vectors for worker/stripper pairs in series.

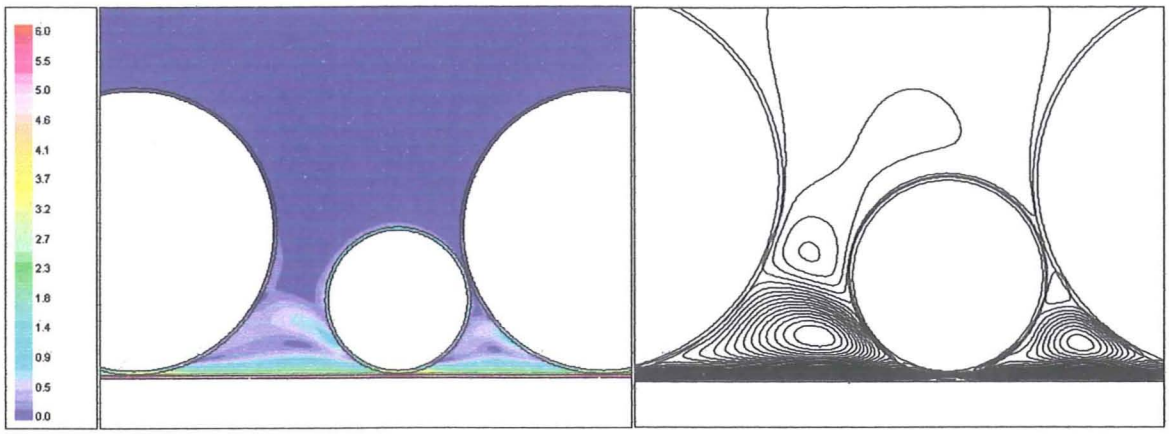

Figures 7.13 and 7.14. CFD output of velocity magnitude (m/s) and stream functions for worker/stripper pairs in series.

7.5.2 Fancy/swift/doffer roller interactions

Figures 7.15 to 7.17 illustrate the velocity vectors, velocity magnitude and stream functions respectively, showing the effect of the rotating fancy roller. The fancy roller is the fastest moving roller in the carding machine set-up. With its long wires, it is also the biggest air pump in the carding machine as well. Using the typical differential speeds of about 20% higher than the swift roller, the results from Section 4.3.7 show the fancy roller can move some 3 times more air than the swift roller can. Small wonder it historically has caused the most aerodynamic problems in the carding machine. The fancy roller is normally covered but if fly strippers are not placed on either side of the fancy, or between the fancy and the doffer (as done on the Chadwick card – refer to Figure 7.1), there occurs a 'blowout' of air through the cover entrance over the swift, in the opposite direction of air and fibre flow, and causes high turbulence and fibre 'fly'. There is also the phenomenon of the air travelling through the fancy wires faster than the surface speed of either the swift or fancy roller causing a 'draft', the same as through a pair of counter-rotating rollers (Section 6.4.1). The maximum air velocity reached was 8.7 m/s, some 16% higher than the fancy roller surface speed and 43% higher than the swift roller surface speed.

Note that in reality, the fancy roller teeth are actually set below the level of the swift wire tips. Achieving this in CFD code would have required some sort of complex 'deforming mesh' system that would have been more trouble than it was worth, especially considering the reasonable accuracy with a 1 mm gap (Section 6.4.2).

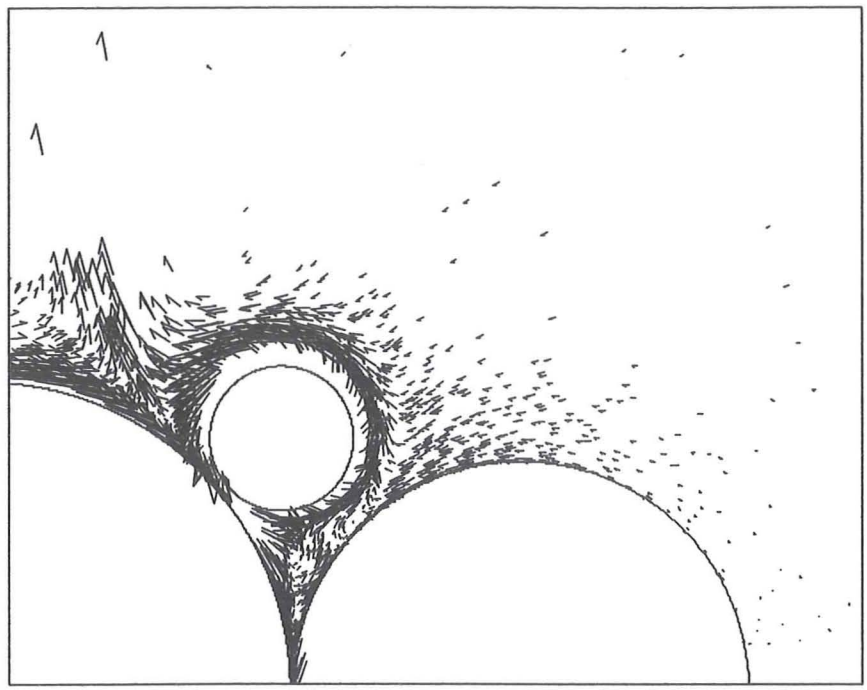

Figure 7.15. CFD output of velocity vectors for the swift/fancy/doffer roller combination.

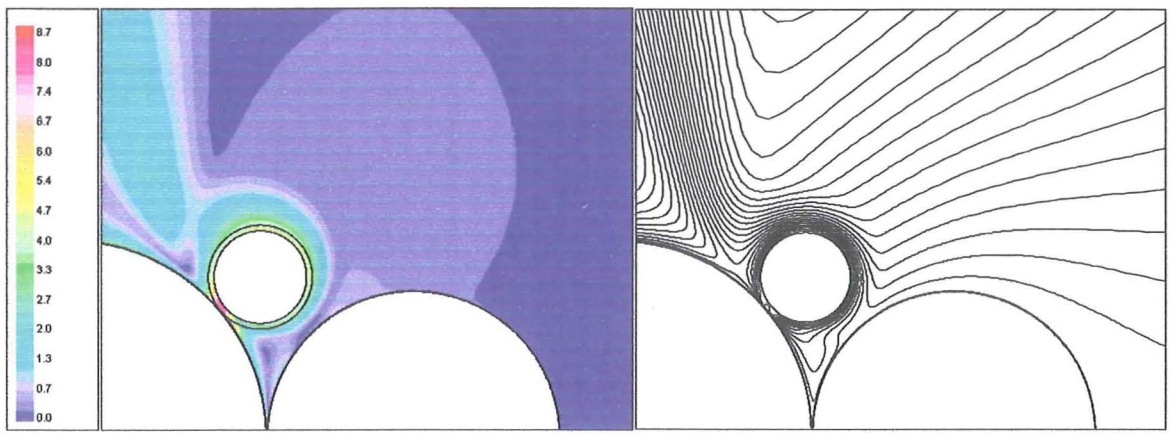

Figures 7.16 and 7.17. CFD output of velocity magnitude (m/s) and stream functions for the swift/fancy/doffer rollers in combination.

7.5.3 Breast/transfer (or lickerin)/swift/worker roller interactions

An area known to be highly turbulent is the area between the breast and transfer rollers. It is a direct application of two relatively fast counter-rotating rollers producing a plume moving away from the two rollers. Figures 7.18 to 7.20 illustrate the plumes generated by the rollers. What may not be so obvious is the larger plume generated under the swift as it bounces off the transfer roller. Unless the swift is positioned very close to the ground the swift, or covers used underneath the swift roller, it would have generated a reasonably sized boundary layer underneath the roller.

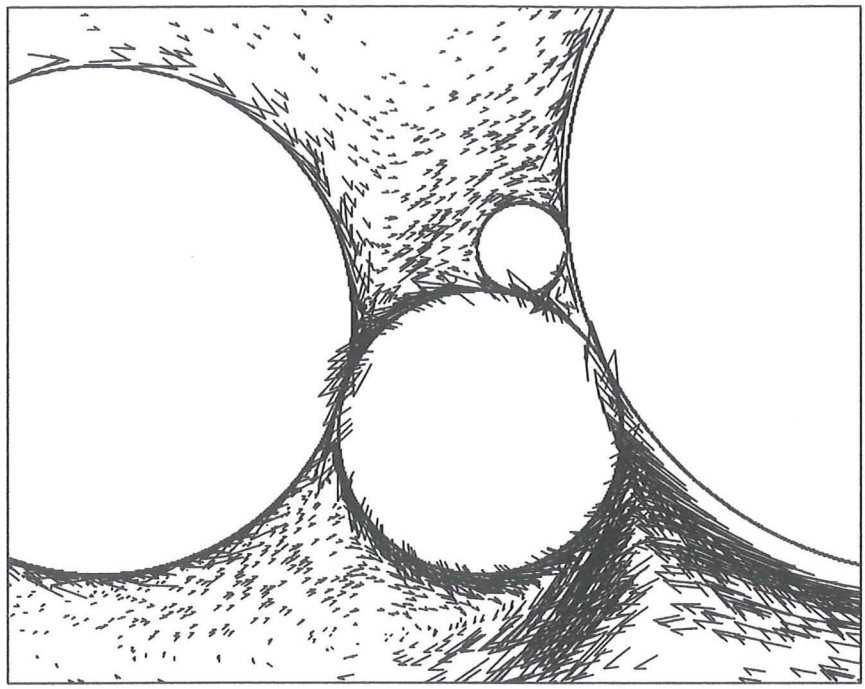

Figure 7.18. CFD output of velocity vectors for the breast/transfer/swift/worker roller combination.

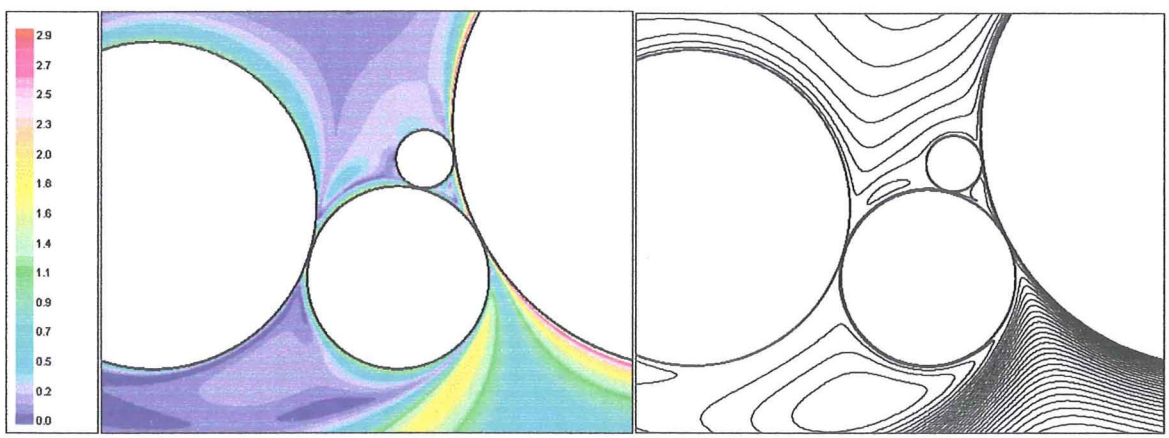

Figures 7.19 and 7.20. CFD output of velocity magnitude (m/s) and stream functions for the breast/transfer/swift/worker rollers in combination.

7.5.4 Swift/doffer/angle stripper roller interactions

Figures 7.21 to 7.23 illustrate the velocity vectors, velocity magnitude and stream functions respectively for this CFD example.. The angle stripper acts as an air dam and a boundary layer suppressor. A vortex is formed directly underneath the angle stripper. However the real action is again occurring underneath the rollers as the plume bounces off the near-stationary doffer roller.

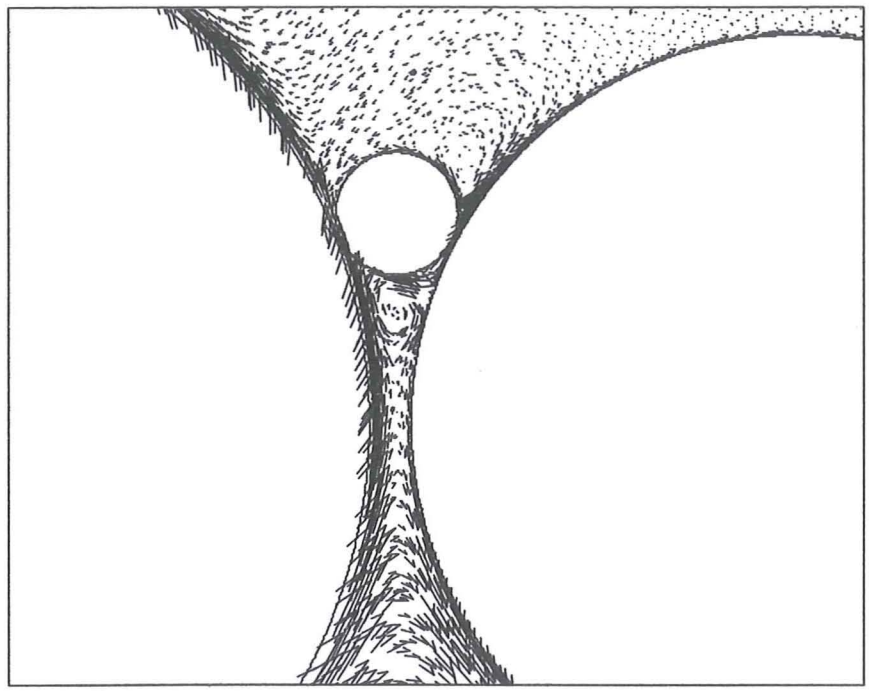

Figure 7.21. CFD output of velocity vectors for the swift/doffer/angle stripper roller combination.

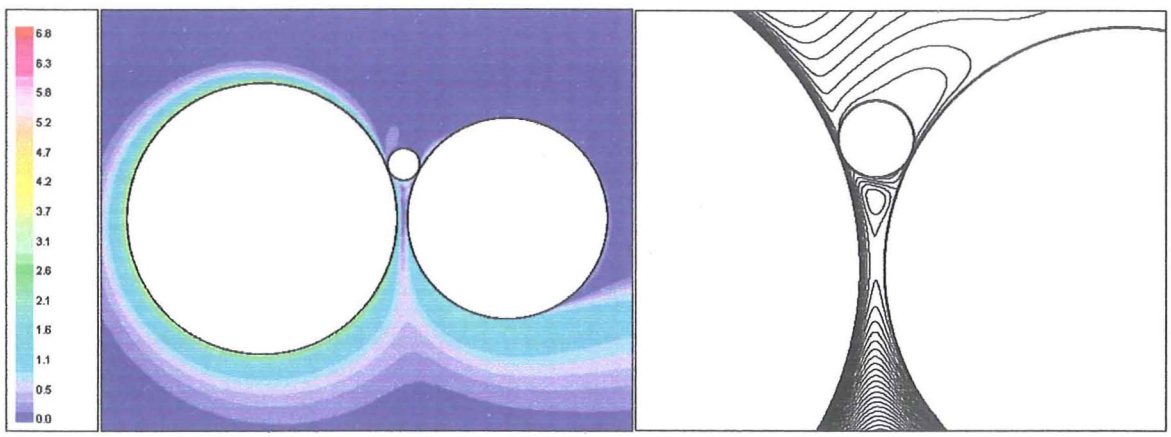

Figures 7.22 and 7.23. CFD output of velocity magnitude (m/s) and stream functions for the swift/doffer/angle stripper rollers in combination.

7.5.5 Swift/mote knife interactions

This example shows how much air can move past a mote knife if a sufficient boundary layer has developed around the swift roller. Mote knives have been used on cotton carding machines to facilitate the removal of heavier contaminants such as dirt or seeds that would tend to move with the airflow rather than be attached to the fibre. There is clear evidence in the previous examples that the swift roller is restricted in generating its own airflow that could be of use in aerodynamic separators such as mote knives. However if there is an

unobstructed section of the swift such as underneath the swift or between the lickerin and the first worker/stripper pair, any mote knife should be situated immediately prior to the obstruction. If gravity cannot assist in the removal of contaminants after it has left the fibrous web, then vacuum slots immediately downstream of the mote knife would be an advantage.

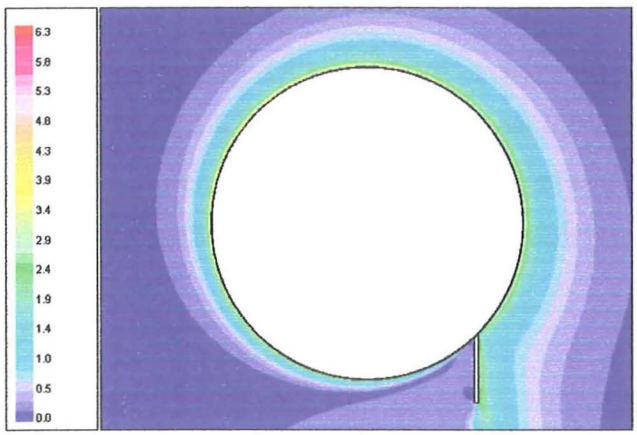

Figure 7.24. CFD output of velocity magnitude (m/s) for a swift roller/mote knife interaction.

7.6 Conclusions

Various rotating roller combinations found in carding machines were modelled using CFD to determine the direction and magnitude of generated air currents. In some cases the CFD output could be compared to experimental flow visualisation data that was recorded above and to the side of the large swift roller. In these cases, the CFD output was similar in velocity magnitude and flow direction. Thus the approach to model certain combinations of rollers rather than the whole machine did not introduce appreciable errors. It also saved a lot of computational expense since the available computers would struggle with the grid size of a full scale machine.

The dominant airflow moving away from the carding machine (secondary flows) was generated by the fancy roller. This was predicted from results in Sections 3.4.2.3 and 4.3.7.

What the 2D models revealed was that there was a lot happening underneath the rollers. The worker/stripper pairs above the swift roller suppressed its boundary layer generation. However if there are gaps between a roller and the floor and/or covers, fast moving rollers such as the breast or swift rollers have the chance to generate a considerable boundary layer

with a lot of air movement. The air slams into the next obstruction such as a roller or cover and bounces off its surface. The flow pattern is similar to that of a fast moving roller situated next to a slow moving or stationary roller (Figures 6.29, 6.35).

There were few readily observable 3D effects occurring on the simplified card. There was a trend for some air to move axially from the edges towards the centre, but it was not as strong as predicted on an isolated 3D cylinder. Little evidence existed of radial flow outwards from the centre of the rollers. Secondary 3D effects including the wall, floor or moving belts could in turn influence the primary 3D effects. Despite the CFD overestimation of 3D effects, the observations from this work were similar to those found in the open literature.

8 CONCLUSIONS

8.1 Original contributions towards this field of study

This work has been the first comprehensive effort to gain a full understanding into how air currents originate and behave on carding machines. Excessive air currents have been the bane of carding machines since the introduction of the fancy roller, if not earlier. The suppression of aerodynamic forces on carding machines has to date been based on art rather than science. The results from this work are also applicable to more general windage studies.

The author could not find anywhere in the open literature where CFD had been used to model any isolated rotating single cylinders in a quiescent zone, let alone a rough cylinder or cylinder pairs. This may be the first publishable work in this area.

The offshoot of this work has been the surprising accuracy of how the velocity profile generated by a smooth rotating cylinder, if corrected for curvature effects, could fit the universal velocity profile for a smooth flat surface. By adding a roughness correction factor, even roughened surfaces could be made to fit the universal velocity profile. This work is the first known effort to determine by experiment the velocity profiles from roughened rotating cylinders.

8.2 Summary of section conclusions

The ongoing literature review showed there has been virtually no work done previously on quantifying aerodynamic forces on carding machines, either from experiment or computer modelling. This was a little surprising given that carding is a processing step for all cotton and wool grown around the world. More literature was available that showed how these aerodynamic forces affected fibre processing. The majority of the review investigated how boundary layers were generated by flat and rotating surfaces. Since no substantive research was available on roughened rotating surfaces, the review concentrated on flat surfaces (smooth and rough) and smooth rotating surfaces.

The experimental and CFD modelling work started on simple flat surfaces roughened by carding wires. Only the formulae used by Waigh (1998) could provide a reasonable estimate of the roughness properties of the wires. Using the porous media model and an optimal porous height (= actual height of roughness elements – displacement depth), Fluent could accurately predict the airflow over flat carding wire surfaces.

Fluent could also accurately simulate flow profiles generated by smooth rotating cylinders. Using corrections for curvature used by Furuya (1978), the CFD output could be fitted onto the same universal velocity profile used for flat plates. Again, using the porous media model with a displacement depth correction (implying in certain cases that only a fraction of the wire surface was being used to actively pump air), the CFD output matched the experimental velocity profile. By adding a roughness correction factor to the curvature-corrected formulae used by Furuya, CFD and experimental data for roughened rotating cylinders could also be fitted to the universal velocity profile. There were some slight discrepancies due to a possible overestimation of shear stresses. When the work was extended to investigate 3D airflow generated by a rotating cylinder, the primary flow (tangential) and secondary flow ('spinning disc') effects predicted from literature were confirmed by CFD and experimental results.

The 2D rotating roller pairs generated air currents that behaved in similar fashion to the single cylinder very close to the surface (<1 mm) but differed elsewhere. The co-rotating rollers generated more intense air currents than counter-rotating rollers, which produced plumes and flow separation points. The flow separation caused instabilities in the flow that CFD could not accurately predict. However CFD could still predict the general flow patterns observed in the experimental work.

The hard and time-consuming work required to determine properly working models in CFD and fine-tuning experimental techniques paid off when modelling carding machine components. The prediction of plume formation from several roller pairs, the fancy roller dominating secondary flow, suppression of air currents above the swift roller and axial flow across the rollers were all predicted from the results in previous sections. The CFD output overestimated 3D effects, but this was in part due to inadequately modelling the complex secondary 3D influences such as the proximity of the carding machine to the floor and roller-roller interactions.

8.3 Summary of CFD capabilities for this application

The general impression is that CFD is a powerful tool in modelling airflow currents around carding machines. It accurately predicted air velocity magnitudes and directions over and around simple geometries such as flat surfaces and single rotating cylinders. It could also predict the general profile of air currents generated by rotating roller combinations found on a carding machine. These results were in turn combined to model flow patterns around a full-scale carding machine in 2D.

Given the correct grid and input conditions, CFD could also successfully model 3D airflow effects around a carding machine.

The drawbacks of CFD were the following:

- The porous media model used in Fluent required two input values, the porous height and inertial resistance factor (inverse porosity) values. Experiments needed to be conducted on a rotating cylinder for every different wire type to obtain these values. Only a small database was obtained in this work. Equations were created to predict porous height and inertial resistance factor from carding wire geometries but had large errors.
- It is well documented that CFD can have problems resolving flow around a separation point. This work proved no exception.
- Modelling 3D effects around an isolated rotating cylinder revealed the general flow patterns expected on a carding machine but not at the correct magnitude.
- The most modern computers in the Department could handle roller combination within the 2D carding machine, but would struggle with a complete full-scale 2D carding machine and well refined 3D grid required for a comprehensive 3D analysis of rotating cylinders.

8.4 Future work

This work has shown that CFD can accurately model airflow movements in carding machines in the absence of fibres. The general airflow profiles found in this work were also consistent with those on fibre-laden carding machines investigated by previous researchers (WIRA, 1948). However air-fibre interactions were not studied in this work. Although it is

known that air currents can have an effect on fibre migration, its extent is still unknown and so is the effect of the fibrous web on altering the airflow profile.

The 3D airflow currents were only briefly investigated in this work. They could not be accurately modelled due to secondary 3D effects and limitations in computational power.

Since one of the longer-term aims is to improve the evenness of the web generated by the carding machine by minimising 3D airflow variations, they need to be modelled accurately. Unfortunately this would require much more computational power than currently available, but could be realistic research within five years.

A more comprehensive database of carding wire properties is required, including porous height and inertial resistance factor values required for CFD input. Adding to this database would allow better prediction of porous height and inertial resistance factor, based on accurate formulae rather than relying on experimental testing for each carding wire. It would also enhance current knowledge on rough surfaces in general, and rotating surfaces in particular.

The 2D CFD modelling in this work used the same roller speeds, diameters, positions and surface roughness as used on the Chadwick card, without the effect of covers. Changing these parameters would be useful work to pursue, particularly the effect of cover position. The other parameters cannot be changed without some significant change to the carding efficiency and would need to be accompanied by pilot plant wool processing trials.

Cotton carding machines use mote knives to remove contaminants from the fibre. One example of a mote knife was modelled in this work, and recommendations were given on where a mote knife would be most appropriate. Future work in this area could fine-tune the optimum dimensions of a mote knife, whilst modelling on CFD software the trajectory of various size particulates as it approaches a mote knife.

Associated with this work (and any work involving determining the influence of fibres on airflows) would be the modelling in CFD software of a fibrous web on a carding machine using a porous media model. The rollers would in effect have two porous layers; the wires and the fibrous web.

9 REFERENCES

Andersson, H. I., Johansson, B., Lofdahl, L., Nilsen, P. J. (1991), Turbulence in the vicinity of a rotating cylinder in a quiescent fluid, 8th Symp. on Turbulent Shear Flows, 30-1-1 – 30-1-6.

Bradshaw, P. (1969), The analogy between streamline curvature and buoyancy in turbulent shear flow, J. Fluid Mech., **36** (1), 177 - 191.

Bramwell, W. C. (1881), The wool carders' Vade Mecum, Boston, Thayer & Wadham, 250.

Dierich, M., Gersten, K., Schlottman, F. (1998), Turbulent flow around a rotating cylinder in a quiescent fluid, Experiments in Fluids **25**, 455 – 460.

Dorfmann, L. A. (1963), Hydrodynamic resistance and the heat loss of rotating solids, Oliver and Boyd.

Dvorak, F. A. (1969), Calculation of turbulent boundary layers on rough surfaces in pressure gradient, AIAA Journal **7** (9), 1752-1759.

Dyrbye, C., Hanson, S. O. (1997), Wind Loads on Structures, Chicester, J. Wiley and Sons Ltd, 19-31.

Elliott, K. H., Carnaby, G. A., Dent, J. B. (1986), A computer simulation model of semi worsted yarn manufacture, II. Modelling the consequences of carding, WRONZ Communication C103, Christchurch, WRONZ, 31p.

Ergun, S. (1952), Chem. Eng. Prog. **48**, 89-94.

Farber, J. F., Dahmen, N. (1996), Trends in textile finishing machinery construction, Melliand International **3**, 151-154.

Fluent User's Guide (1996) Lebanon, NH, Fluent Inc.

Furuya, Y., Nakamura, I., Yamashita, S. (1978), The laminar and turbulent boundary layers on some rotating bodies in axial flows, Mem. Fac. Eng, Nagoya Univ. **30** (1), 1-58.

Ghosh, G. C., Bhaduri, S. N. (1968), Studies on hook formation and cylinder loading on the cotton card, Textile Res. J. 38, 535-543.

Grabow, R. M., White, C. O. (1975), Surface roughness effects on nosetip ablation characteristics, AIAA Journal **13** (5), 605-609.

Hewitt, A., Townend, P. P. (1971), The effect of fibre length, linear density, production rate and swift tooth angle on droppings during carding, J. Text. Inst. 62, 648-653.

Jackson, P. S. (1977), Aspects of wind behaviour, Wind Engineering 1 (1), 1-14.

Kasagi, N., Hirata, M. (1975), Transport phenomena in near-wall region of turbulent boundary layer around a rotating cylinder, ASME Paper No. 75-WA/HT-58.

Kirchoff, R. H.(1985), Potential flows: computer graphic solutions, New York, M. Dekker.

Klein, W. (1986), A practical guide to opening and carding, Plymouth, Latimer Trend & Co Ltd, 4-23.

Klein, W. (1985), The technology of short-staple spinning, Plymouth, Latimer Trend & Co Ltd, 18-20.

Kong, L. X., Platfoot, R. A. (1996), Two-dimensional simulation of air flow in the transfer duct of open-end rotor spinning machines, Textile Res. J. 66 (10), 641-650.

Lauber, M., Wulfhorst, B. (1995), Non-contact gauging of the fiber flow during carding and drafting of cotton, Melliand Textilberichte. 76 (5), E77-78.

Lettau, H. (1969), Note on aerodynamic roughness-parameter on the basis of roughness element description, J. Applied Meteorology 8, 828-832.

Marshall, J. K. (1971), Drag measurements in roughness arrays of varying density and distribution, Agr. Meteorol. 8, 269-292.

Martindale, J. G. (1945), The distribution and movement of wool on woollen cards, Trans. J. Text. Inst, T213-228.

Massey, B. S. (1989), Mechanics of Fluids, 6th ed., Chapman and Hill, London, 205.

Millikan, C. B. (1939), Proc. 5th Int. Congr. Appl. Mech., Cambridge, USA, p 25.

Milne-Thomson, L. M. (1968), Theoretical Hydrodynamics, 5th ed., London, MacMillan.

Mulhearn, P. J. (1977), Turbulent flow over a very rough surface, 6th Australian Hydraulics and Fluid Mechanics Conference, Adelaide, Australia, 269-272.

Nakamura, I., Ueki, Y., Yamashita, S. (1983), A universal velocity distribution and turbulence properties in the shear flow on a rotating cylinder in a quiescent fluid, 4th Symp. on Turbulent Shear Flows, Karlsruhe, 2-21 – 2-26.

O'Laughlin, E. M. (1969), Flow Phenomena Near Rough Boundaries, J. Hydraulic Research 7, 231-250.

Schlichting, H. (1979), Boundary Layer Theory, 7th ed., New York, McGraw Hill.

Sigal, A., Danberg, J. E. (1990), New correlation of roughness density effect on the turbulent boundary layer, AIAA Journal **28** (3), 354-356.

Simpson, R. L. (1973), A generalised correlation of roughness density effects on the turbulent boundary layer, AIAA Journal **11** (2), 242-244.

Smith, G. P., Townsend, A. A. (1982), Turbulent Couette flow between concentric cylinders, J. Fluid Mech. **123**, 187 – 217.

Taylor, G. I. (1923), Fluid friction between rotating cylinders, Phil. Trans. Roy. Soc. London **223**, 289-343.

Theodorsen, T., Regier, A. (1944), Experiments on drag of rotating discs, cylinders an streamline rods at high speeds, NACA Report No. 793.

Waigh, D. R., Kind, R. J. (1998), Improved aerodynamic characterisation of regular three dimensional roughness, AIAA Journal **36** (6), 1177-1178.

Wild, P. M., Djilali, N., Vickers, G. W. (1996), Experimental and computational assessment of windage losses in rotating machinery, Trans. ASME J. Fluids Engineering 118, 116-122.

Williamson, J. W., Koukousakis, C. (1987), Turbulent flow around a rotating cylinder, ASME Applied Mechanics, Bioengineering and Fluids Engineering Conference, FED-Vol. 51, 79 – 83.

WIRA (1948), Wool Research, Vol. 4: Carding, Leeds, WIRA.

WIRA (1969), Woollen Carding, Leeds, WIRA.

Wooding, R. A., Bradley, E. F., Marshall, J. K. (1973), Drag due to regular arrays of roughness elements of varying geometry, Boundary-layer Meteorology **5**, 285-308.

WRONZ (1994), The Technology of Woollen Carding, An Intensive Short Course, Christchurch, WRONZ.

WRONZ (1997), unpublished information.

10 NOMENCLATURE

$A \approx 5.5$ for hydraulically smooth surfaces

A_f = specific area of flat surface per roughness element, m^2

A_p = projected area of roughness in flow direction, m^2

A_s = windward surface area of roughness, m^2

a = radius of cylinder, m

B = constant

C_2 = inertial resistance factor (inverse porosity), 1/m

C_f = friction coefficient, dimensionless

C_{Re} = roughness constant, dimensionless

d = displacement depth, m

H = pressure drop, mm H_2O

k = actual height of roughness element, m

K = shear force moment correction factor, dimensionless

k_s = equivalent sand roughness height, m

L = porous depth, m

l = turbulent mixing length, m

n = spacing between elements normal to flow, m

P = air pressure, mbar

ΔP = pressure drop, N/m^2

$\Delta P/L$ = pressure gradient, N/m^3

p = horizontal length of roughness element normal to flow, m

q = velocity magnitude, m/s (Section 2.4.1)

Q = volumetric flowrate, m^3/s

r = distance from centre of origin, m

r^+ = roughness correction, dimensionless

Re = Reynolds number, dimensionless

s = spacing between elements parallel to flow, m

T = air temperature, °C

t = horizontal length of roughness element parallel to flow, m

U = average velocity, average tangential velocity, m/s

u = localised tangential velocity, m/s

u_* = friction velocity, m/s

u_* = friction velocity, m/s

u' = $U - u$, m/s

u^+ = dimensionless velocity (Equations 4a, b), dimensionless

$u^+ = U/u_*$

v = generic term for velocity, m/s

$v(t)$ = instantaneous velocity, m/s

v' = localised radial velocity, m/s

$\overline{v}$ = average velocity, m/s

z = distance from surface, m

z^+ = dimensionless length

z_0 = aerodynamic roughness height, m

α = permeability, m^2

β = bluntness parameter (= A_s/A_p)

δ = boundary layer thickness, m

ε = eddy viscosity, Ns/m^2

θ = momentum thickness, m

κ = Von Karman's constant

$\lambda = A_f/A_p$

$\lambda_d = s/t$

μ = dynamic viscosity, Ns/m^2

ν = kinematic viscosity, m^2/s

ξ = vorticity magnitude, m/s

τ = shear stress, N/m^2

ψ = stream function, m^2/s

ψ_1 = streamwise aspect ratio = (k/t)

ψ_2 = spanwise aspect ratio (= k/p)

ω = angular velocity, rad/s

ω_* = friction angular velocity, rad/s

ω^+ = dimensionless angular velocity

Subscripts

i	inner
o	outer
t	turbulent
w	wall

APPENDIX

Fluent 5.0 report summary for base case of smooth roller (107 mm radius) with no porosity.

Models

Model	Settings
Space	2D
Time	Steady
Viscous	RNG k-epsilon turbulence model
Wall Treatment	Two-Layer Zonal Model

Boundary Conditions

Zones

name	id	type	physical description
air	1	fluid	air surrounding roller
porous	2	fluid	air within carding wire
porous-boundary	5	interior	wire tips
inlet:008	8	periodic	
inlet	6	periodic	
boundary	3	wall	imaginary outer boundary
roller	4	wall	rotating cylinder
default-interior	9	interior	
default-interior:011	11	interior	

Boundary Conditions

air

Condition	Value
Material Name	air
Specify source terms?	no
Source Terms	()
Motion Type	0
X-Velocity Of Zone	0
Y-Velocity Of Zone	0
Rotation speed	0
X-Origin of Rotation-Axis	0
Y-Origin of Rotation-Axis	0
Laminar zone?	no
Porous zone?	no

X-Component of Direction-1 Vector	1
Y-Component of Direction-1 Vector	0
Direction-1 Viscous Resistance	0
Direction-2 Viscous Resistance	0
Direction-3 Viscous Resistance	0
Direction-1 Inertial Resistance	0
Direction-2 Inertial Resistance	0
Direction-3 Inertial Resistance	0
C0 Coefficient for Power-Law	0
C1 Coefficient for Power-Law	0

porous

Condition	Value	
Material Name	air	
Specify source terms?	no	
Source Terms	()	
Motion Type	0	
X-Velocity Of Zone	0	
Y-Velocity Of Zone	0	
Rotation speed	0	
X-Origin of Rotation-Axis		0
Y-Origin of Rotation-Axis		0
Laminar zone?	no	
Porous zone?	no	
X-Component of Direction-1 Vector	1	
Y-Component of Direction-1 Vector	0	
Direction-1 Viscous Resistance	0	
Direction-2 Viscous Resistance	0	
Direction-3 Viscous Resistance	0	
Direction-1 Inertial Resistance	0	
Direction-2 Inertial Resistance	0	
Direction-3 Inertial Resistance	0	
C0 Coefficient for Power-Law	0	
C1 Coefficient for Power-Law	0	

porous-boundary

Condition	Value

inlet:008

Condition	Value
Rotationally Periodic?	yes

inlet

Condition	Value
Rotationally Periodic?	yes

boundary

Condition	Value
Free Stream Temperature	300
Apply a velocity to this wall?	no
Define wall motion relative to adjacent cell zone?	yes
Apply a rotational velocity to this wall?	no
Velocity Magnitude	0
X-Component of Wall Translation	1
Y-Component of Wall Translation	0
Rotation Speed	0
X-Position of Rotation-Axis Origin	0
Y-Position of Rotation-Axis Origin	0
Specify shear stress?	no
X-component of shear stress	0
Y-component of shear stress	0
Swirl component of shear stress	0

roller

Condition	Value
Free Stream Temperature	300
Apply a velocity to this wall?	yes
Define wall motion relative to adjacent cell zone?	yes
Apply a rotational velocity to this wall?	yes
Velocity Magnitude	0
X-Component of Wall Translation	1
Y-Component of Wall Translation	0
Rotation Speed	-175.436
X-Position of Rotation-Axis Origin	0
Y-Position of Rotation-Axis Origin	0
Specify shear stress?	no
X-component of shear stress	0
Y-component of shear stress	0
Swirl component of shear stress	0

Solver Controls

Equations

Equation	Solved

Flow	yes
Turbulence	yes

Numerics

Numeric	Enabled
Absolute Velocity Formulation	no

Relaxation

Variable	Relaxation Factor
Pressure	0.5
Momentum	0.5
Turbulence Kinetic Energy	0.5
Turbulence Dissipation Rate	0.5
Viscosity	0.5
Density	1
Body Forces	1

Linear Solver

Variable	Solver Type	Termination Criterion	Residual Reduction Tolerance
Pressure	V-Cycle	0.1	
X-Momentum	Flexible	0.1	0.69999999
Y-Momentum	Flexible	0.1	0.69999999
Turbulence Kinetic Energy	Flexible	0.1	0.69999999
Turbulence Dissipation Rate	Flexible	0.1	0.69999999

Discretization Scheme

Variable	Scheme
Pressure	Second Order Upwind
Momentum	Second Order Upwind
Pressure-Velocity Coupling	PISO
Turbulence Kinetic Energy	Second Order Upwind
Turbulence Dissipation Rate	Second Order Upwind

Solution Limits

Quantity	Limit
Minimum Absolute Pressure	1
Maximum Absolute Pressure	5000000
Minimum Temperature	1
Maximum Temperature	5000

Minimum Turb. Kinetic Energy	1e-10
Maximum Turb. Viscosity Ratio	100000

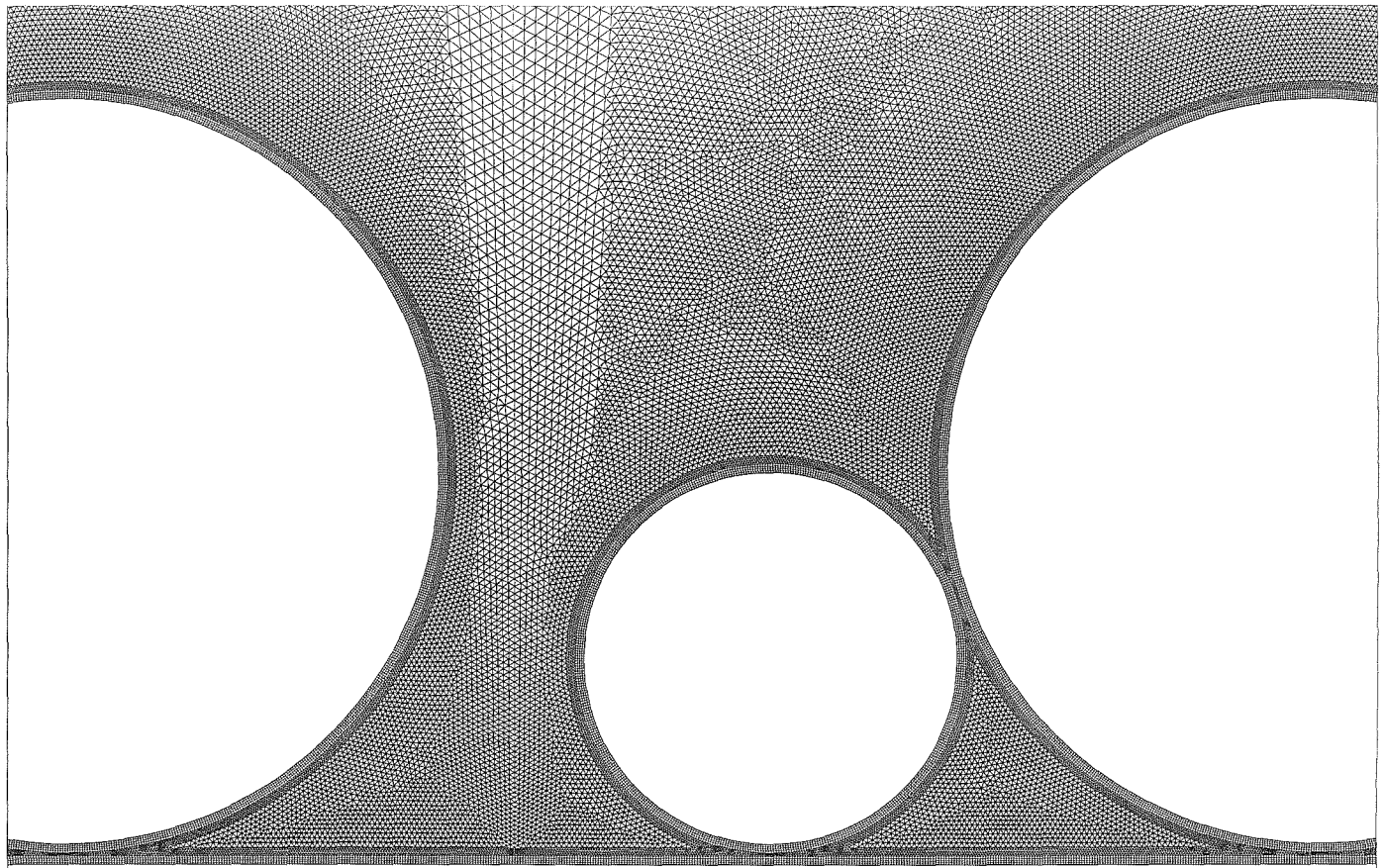

Close-up grid of swift/worker/stripper in series
Grid

Jul 20, 2001
FLUENT 5.4 (2d, dp, segregated, ke)

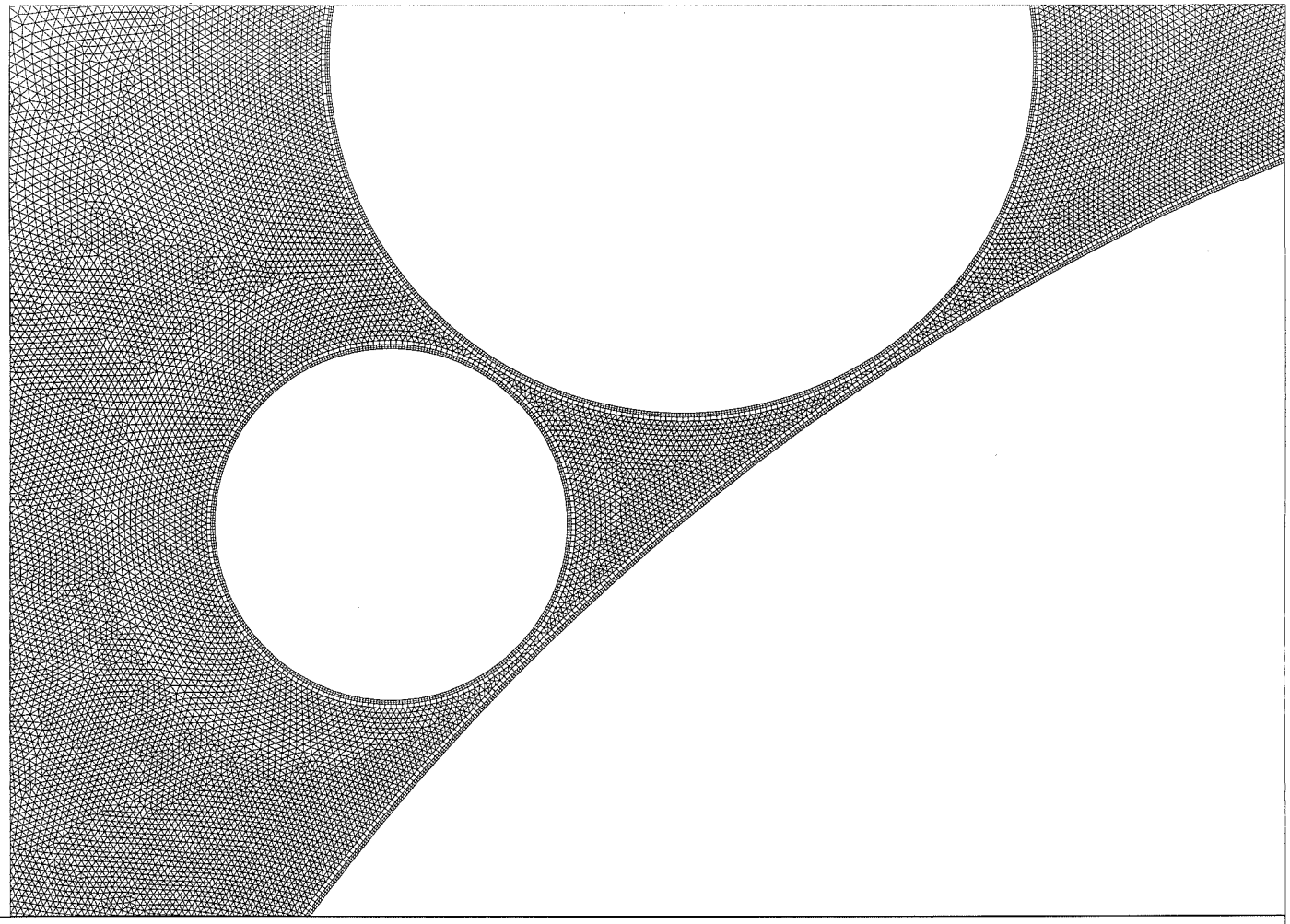

Close-up of swift/worker/stripper
Grid

Jul 20, 2001
FLUENT 5.4 (2d, dp, segregated, ke)

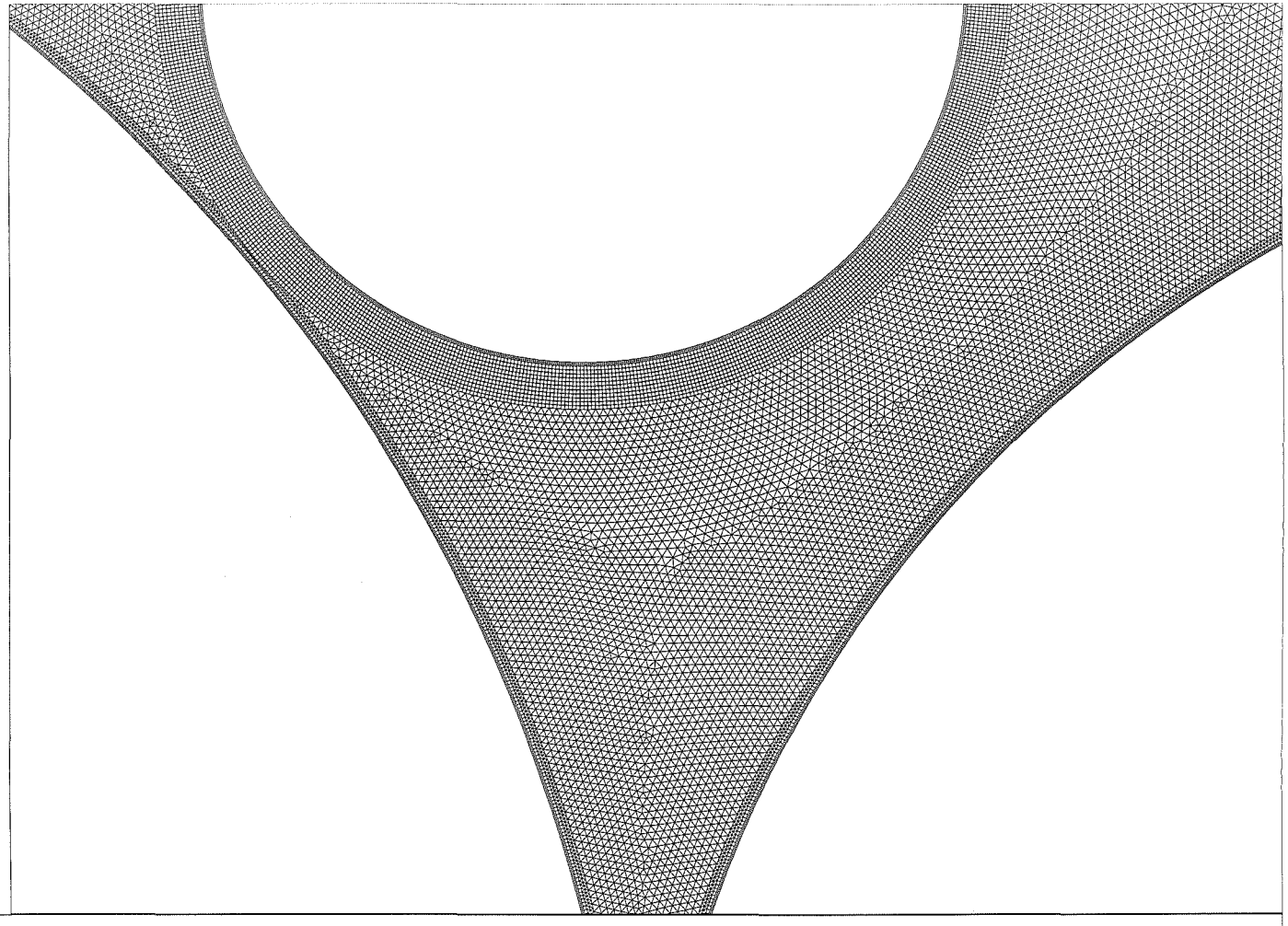

Close-up grid of fancy/swift/doffer
Grid

Jul 20, 2001
FLUENT 5.4 (2d, dp, segregated, ke)

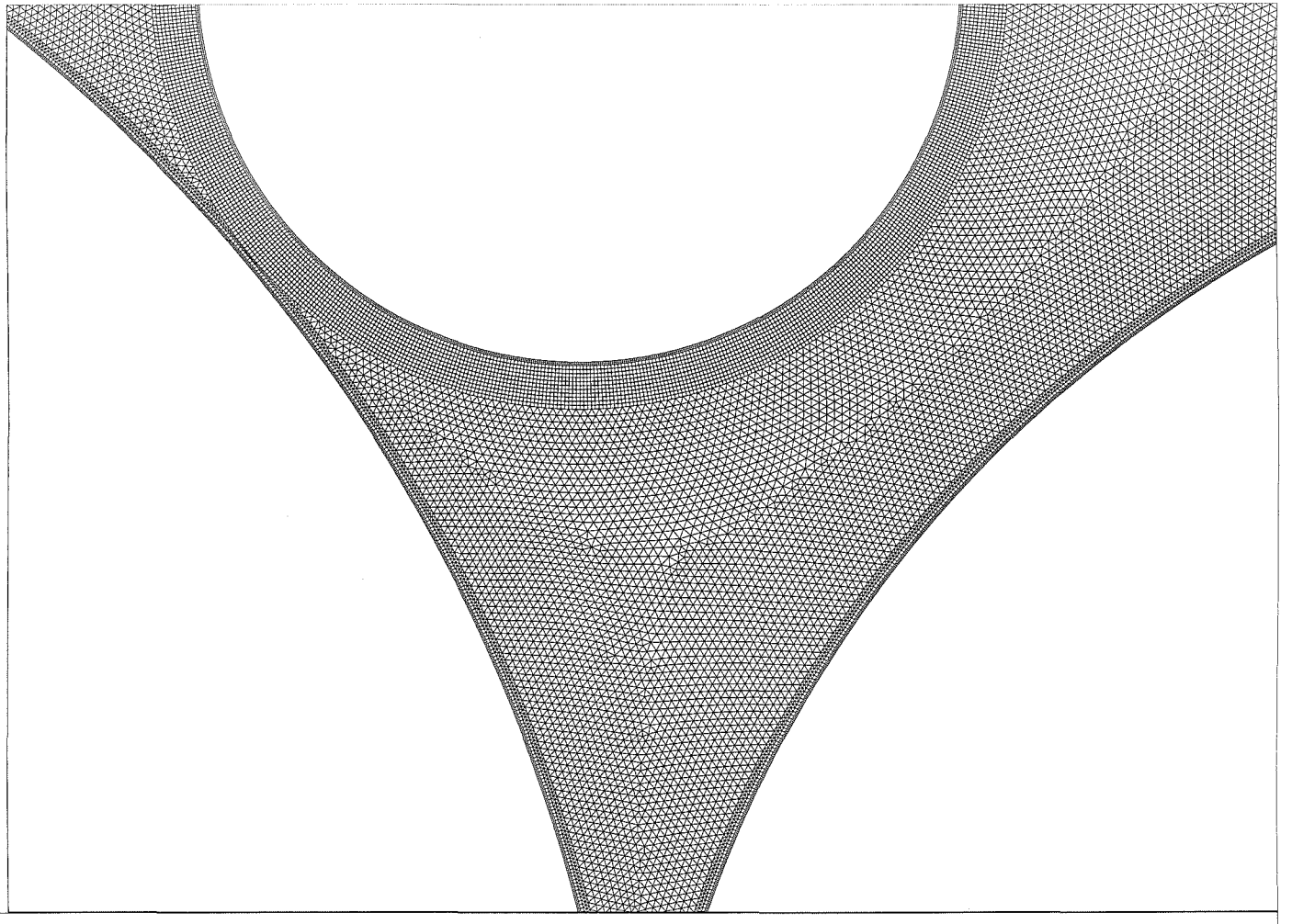

Close-up grid of fancy/swift/doffer
Grid

Jul 20, 2001
FLUENT 5.4 (2d, dp, segregated, ke)

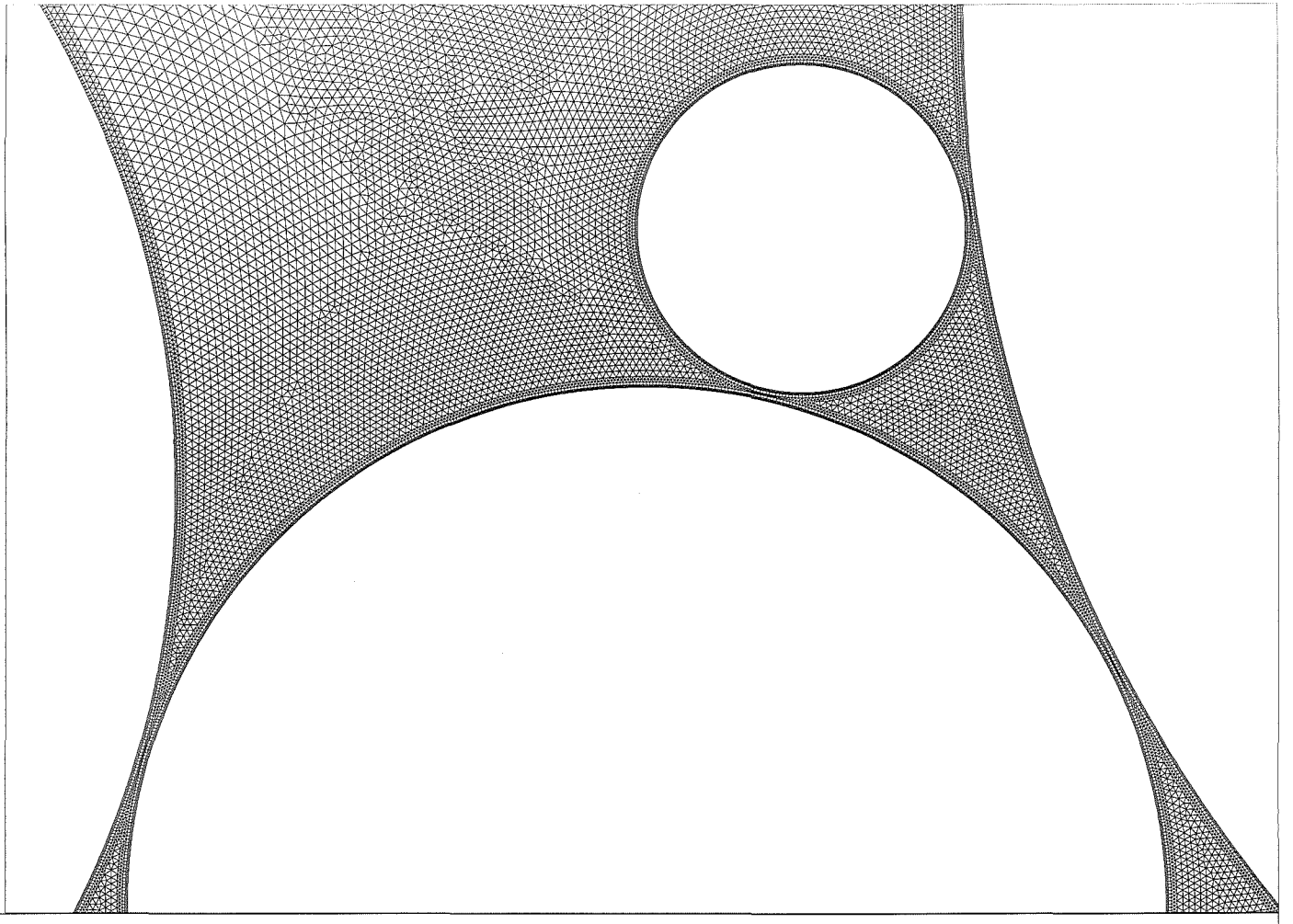

Close-up grid of breast/transfer/swift/worker
Grid

Jul 20, 2001
FLUENT 5.4 (2d, dp, segregated, ke)

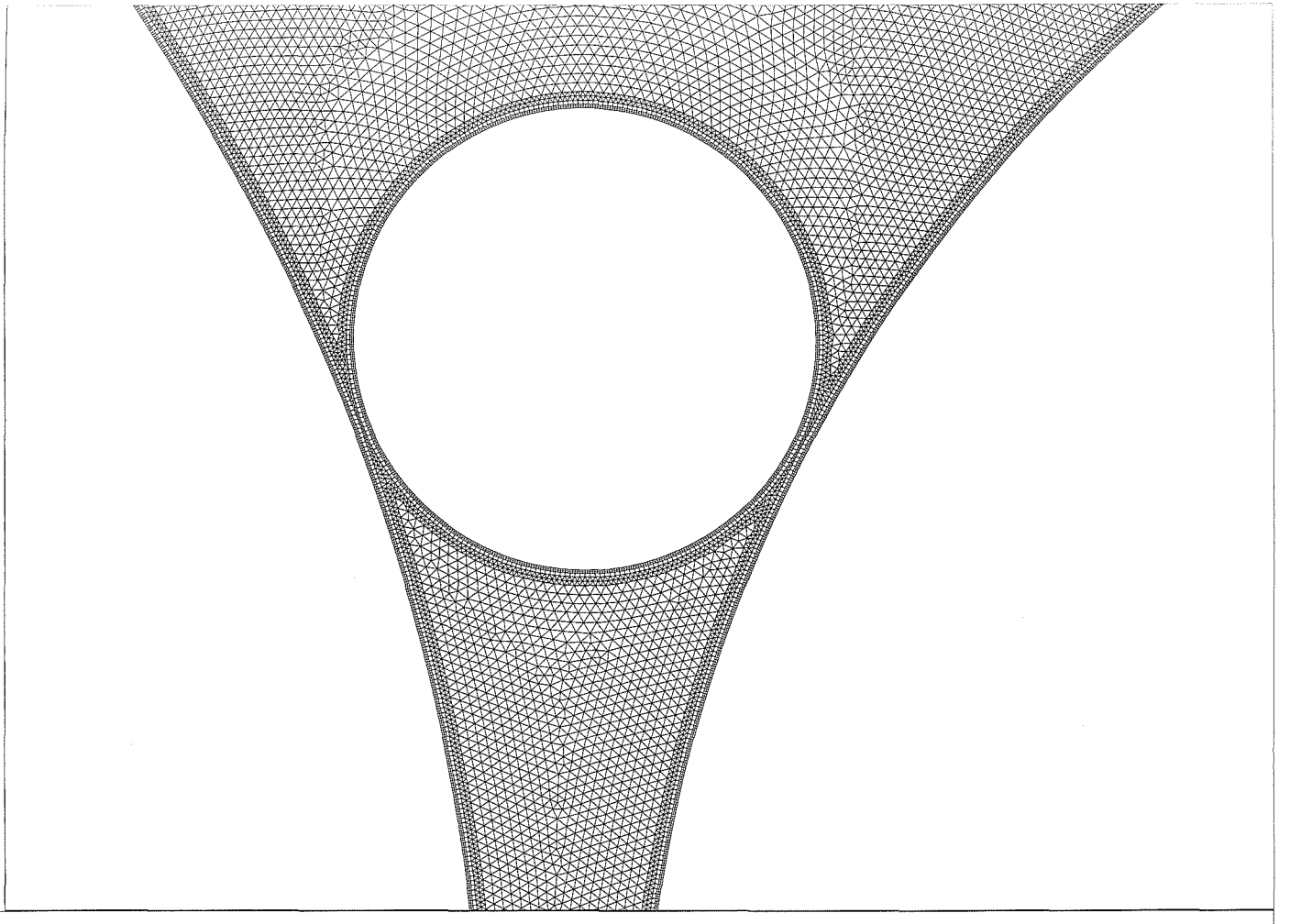

Close-up grid of swift/doffer/angle stripper
Grid

Jul 20, 2001
FLUENT 5.4 (2d, dp, segregated, ke)

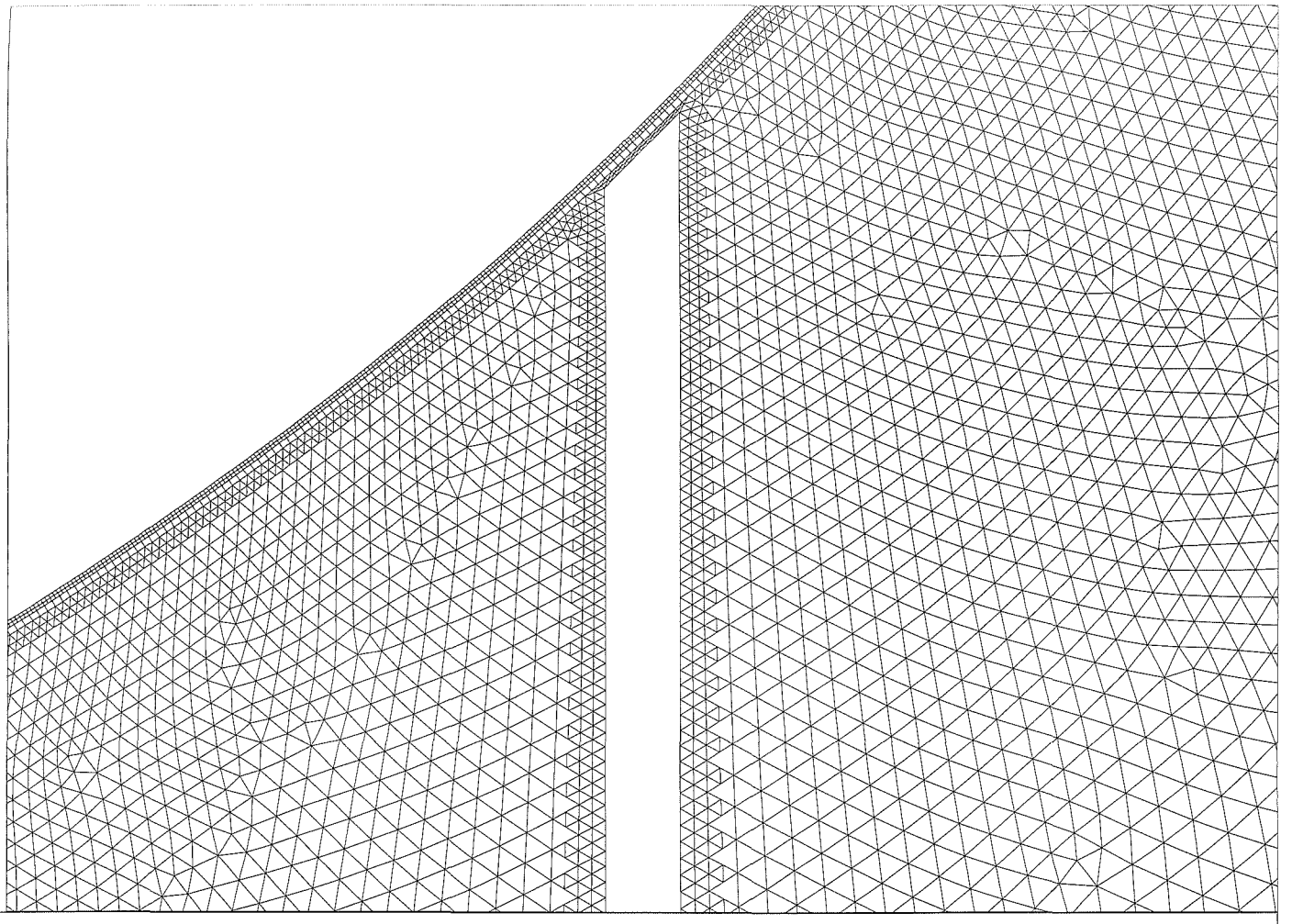

Close-up grid of swift/mote knife
Grid

Jul 20, 2001
FLUENT 5.4 (2d, dp, segregated, ke)